Dual-load Hybrid Detection of Water Content Using Electromagnetic and Surface Acoustic Wave Sensors

Dem Fachbereich Elektrotechnik und Informationstechnik
der Technischen Universität Darmstadt
zur Erlangung des akademischen Grades eines
Doktor-Ingenieurs (Dr.-Ing.)
genehmigte Dissertation

Dissertation

von

M. Sc.
Donghang Lu
geboren am 19. November 1985
in Jilin, China

Referent	:	Prof. Dr.-Ing. Rolf Jakoby
Korreferent	:	Prof. Dr. mont. Mario Kupnik
Tag der Einreichung	:	12.07.2016
Tag der mündlichen Prfüng	:	27.10.2016

D17
Darmstadt 2016

Preface

This dissertation is a summary and precious reflection of my work as a research assistant at the Institute for Microwave Engineering and Photonics at Technische Universität Darmstadt. In the past four and half years, I have received a lot of help and support and therefore would like to extend my deepest gratitudes to the following important people in my life.

First of all I would like to express my gratitude to Prof. Dr.-Ing. Rolf Jakoby, who allowed me the opportunity to conduct research at his institute as my supervisor. Without his profound advice, warm encouragement and helpful guidance, this dissertation would never have come to fruition.

Secondly, I would like to deeply thank Prof. Dr.-Ing. Andreas Penirschke, who was my group leader. His tireless patience and thorough instruction were pivotal in my understanding of sensor design principles.

Moreover, I would like to give many thanks to Dr. Yuliang Zheng, who provided the path for me to continue my research while showing me a solution when I was deeply confused.

I would also like to thank Dr. Mattias Maasch. With his wisdom, I have gained a lot more than I could ever imagine.

For the inspiring discussions and constructive cooperation, the support of my fellow colleagues in the Institute for Microwave Engineering and Photonics are warmly appreciated. In particular, I'm deeply grateful for the help of Dr. Martin Schüler, Dr. Aleksandar Angelovski, Mr. Alex Wiens, Mr. Christian Weickmann and Dr. Holger Maune for the limitless support and cordial friendship over the last several years.

Lastly, I would like to thank my parents, Mr. Qingyi Lu and Ms. Lina Fu, for all their years of selfless support and understanding, and my friend Feng Gu whose friendship I really appreciate.

Abstract

This work focuses on water content detection both in materials and in gases, i.e., measurements of moisture and humidity. To detect the moisture, a cavity perturbation method (CPM) is introduced to extract the relationship between permittivity and water content in material under test (MUT), which, in this application is tobacco at a single frequency. The obtained information is used as pre-knowledge for a mass flow sensor design in tobacco production. The mass flow sensor is an open cylindrical resonator that consists of two circular waveguides with different diameters. An on-sight test of the mass flow sensor is performed, and the measured weights are within a 10 % discrepancy compared to the supplied weights. For the humidity measurement, a material named polyvinyl alcohol (PVA) is employed as a sensitive layer. The PVA film involves two mechanisms for humidity sensing, which are variations of electrical loading and mechanical loading with relative humidity (RH). To apply the electrical loading property, the PVA film is characterized by an interdigital capacitor (IDC) in a wide frequency range at different RHs, and the results are used to create a comprehensive model of the PVA film for computer simulation tools to predict the performance of the sensor. A wireless humidity sensor is designed to verify the PVA film model, and a good agreement between the simulation and measurement results proves the accuracy of the model. To utilize the mechanical loading property, the PVA film is loaded on surface acoustic wave (SAW) resonators. A wet chemical method of patterning the PVA film is found, and the influence of the PVA film thickness is investigated. With different patterns and thicknesses of the PVA film, humidity sensors can achieve various performances in terms of operation range, sensitivity, and quality factor. To apply both, electrical and mechanical loading properties of the PVA film for humidity sensing at the same time, a novel dual-load SAW resonator is introduced by using additional IDCs as reflectors with the PVA film loaded on top. The humidity sensor based on this novel hybrid structure extends its operating range, and shows better sensitivity and quality factor with different sensing mechanisms within certain RH ranges. A figure of merit (FoM) is defined to evaluate the sensitivity and quality factor of the sensor at the same time, and the sensing mechanism

with better FoM can be selected for humidity sensing in a defined RH range.

Kurzfassung

Die Bestimmung des Wassergehaltes in einem flüssigen oder festen Medium sowie des Feuchtigkeitsgehaltes in einem gasförmigen Medium ist eine zentrale Aufgabe in vielen industriellen Prozessen. Die Verarbeitung von Materialien erfolgt häufig bei einer fest vorgeschriebenen Prozessfeuchte um die Qualität des Materials nicht zu beeinflussen oder aber eine bestimmte Reaktion kann nur unter einem fest vorgegebenen Feuchtigkeitsgehalt der Umgebungsluft ablaufen In dieser Arbeit werden Methoden zur Erkennung des Wasser- bzw. Feuchtegehaltes in festen sowie gasförmigen Medien untersucht und darauf basierend Sensoren zur Messung dieser entwickelt. Der erste Teil der Arbeit beschäftigt sich mit der Eignung, sowie der Dimensionierung eines mikrowellenbasierten Sensors für die Tabakindustrie. Für einen Nachweis der Feuchtigkeit im Rohtabak wurde das Störkörper- Messverfahren angewendet, um die Beziehung zwischen der Permittivität und dem Wassergehalt des Messgutes bei der Arbeitsfrequenz zu extrahieren. Basierend auf der erhaltenen Information wurde ein Sensor zur Bestimmung des Massenstromes in der Tabakproduktion entwickelt. Der Massenstromsensor besteht aus einem offenen zylindrischen Resonator, der aus zwei kreisförmigen Hohlleitern mit unterschiedlichen Durchmessern besteht. Im Versuchsstand der Riedel Filtertechnik GmbH konnte anhand realitätsnaher Tests des Massenstromsensors Abweichungen von weniger als 10 % im Vergleich zum Istwert erreicht werden. Der zweite Teil der Arbeit untersucht die Messung der Luftfeuchtigkeit. Als sensitives Material wurde Polyvinylalkohol (PVA) ausgewählt, da PVA zwei Mechanismen für die Messung der Feuchtigkeit, die Änderung der elektrischen Beladung und der mechanischen Beladung eines SAW Resonators in Abhängigkeit der Feuchtigkeit besitzt. Die Änderung der dielektrischen Eigenschaften als Funktion der Luftfeuchtigkeit des PVA-Films wird mit einem Interdigitalkondensator (IDC) in einem breiten Frequenzband bei verschiedenen relativen Luftfeuchtigkeiten (RHs) gemessen. Mit Hilfe der Ergebnisse konnte ein umfassendes Modell des PVA-Films für die Computersimulation zur Vorhersage der Eigenschaften von Sensoren erstellt werden. Ein drahtloser Feuchtigkeitsensor wurde entworfen, um das Modell für den PVA-Film zu verifizieren. Die Genauigkeit des Modells wird durch eine

gute Übereinstimmung zwischen der Simulation und den Messergebnissen bestätigt. Um die Änderung der mechanischen Beladung zu nutzen, wurde der PVA-Film auf Resonatoren der akustischen Oberflächenwellen (SAW) geladen. Ein nass-chemisches Verfahren für die Strukturierung des PVA-Films wurde entwickelt und der Einfluss der Lagendicke des PVA-Films untersucht. Mit verschiedenen Strukturen und Lagendicken des PVA-Films ist es möglich, Feuchtigkeitssensoren für verschiedene Betriebsbereiche, Empfindlichkeiten und Qualitätsfaktoren zu erzielen. Um beide Eigenschaften von PVA, die elektrischen Beladung und mechanicshen Beladung gleichzeitig anwenden zu können, wurde ein neuer SAW-Resonator entwickelt, der IDCs als Kapazitäten und gleichzeitig als Reflektoren besitzt. Der Feuchtigkeitssensor erweitert damit seinen Betriebsbereich und zeigt eine bessere Empfindlichkeit und Qualitätsfaktor in einen bestimmten RH-Bereich. Es wurde ein Qualitätsfaktor (FoM) definiert, der gleichzeitig die Empfindlichkeiten und die Gütefaktoren des Sensors auswertet. Die Messungsmechanismen mit besseren FoM können dann für die RH-Messung in einem definierten RH-Bereich ausgewählt werden.

Acronyms

COM coupling of modes

CPM cavity perturbation method

CPW coplanar waveguide

EMW electromagnetic wave

FEM finite element method

FoM figure of merit

GUI graphical user interface

IDC interdigital capacitor

IDT interdigital transducer

ISM industrial scientific and medical

$LiNbO_3$ Lithium Niobate

$LiTaO_3$ Lithium Tantalate

MIF metal ion free

MSE mean square error

MUT material under test

PTFE polytetrafluoroethylene

PVA polyvinyl alcohol

RCS radar cross section

RH relative humidity

SAW surface acoustic wave

SG signal ground

TE transverse electric

TEM transverse electromagnetic

TM transverse magnetic

UV ultraviolet

VNA vector network analyzer

Contents

Chapter 1

Introduction

"If there is magic on the planet, it is contained in the water."
–Loren Eisley

Water content influences many aspects of both our daily lives, and industrial and agricultural activities. Our comfort and well-being depend on the humidity of the living environment. If humidity is too low, people feel the dryness and easily get sick; if the humidity is too high, people feel more heat than the actual temperature shows. In this case, monitoring the humidity can help people tailor the environment for their comfort. From an industry standpoint, the requirement for controlling the humidity is extremely strict. Some equipments can only be operated in a humidity-controlled environment such as electrostatic sensitive components or high voltage equipments. In the pharmaceutical industry, production under a precisely controlled humidity environment is the key to guaranteeing quality. In agriculture, the storage of farm products requires that moisture is being properly monitored. For instance, if the moisture content is too high, farm products will rot or grow mold; on the other hand, if the products are too dry, they could disintegrate during transportation. To have comfortable living conditions and avoid damage and danger in the production processes, the demands for accurate, low cost and reliable sensors for moisture and humidity detection have increased dramatically [1–5]. Therefore, this work focuses on detecting the water content in solid materials using material characterization methods and the water vapor in gases by employing a functional layer for sensors design.

The water content in solid materials can be related to its dielectric properties, which are easily obtained through the measurements conducted by vector network analyzers (VNAs). There are several methods to characterize the permittivity of dielectric material at microwaves. In general, these are categorized as resonant methods and non-resonant methods.

The resonant methods are based on the resonance phenomena, e.g., microwave resonance in coaxial resonators, while the non-resonant methods are based on propagation, e.g., the microwave propagation in transmission lines [6]. Resonant methods are typically used to achieve accurate results of the material electrical properties at a single frequency, e.g., the cavity perturbation method (CPM) [7]. The complex permittivity of dielectric materials is calculated from the resonant frequency and quality factor of the resonators or from the changes of both. Non-resonant methods are used for material characterization over a wide frequency range, e.g., coaxial transmission method [8], which obtain dielectric information within a broadband.

To detect water vapor in gases, humidity sensitive materials play very important roles. Considerable efforts have been taken in the investigation of hygroscopic materials for humidity sensing, including materials such as polyethynylfluorenol [9], polyvinyl alcohol (PVA) [10, 11], pyrrolidone [12], poly and sodium polysulfonesulfonate [13], cellulose acetate [14], PolyXIO [15] and customized polyimides [16]. Among all of these materials, PVA has gained recognition as a promising material for relative humidity (RH) sensing due to its strong sensitivity, ease of process and low price. When PVA film is exposed to humid gas, it absorbs or desorbs water molecules in the humid gas based on the humidity level. The PVA film exhibits two main mechanisms for RH sensing application, namely the change of electrical loading and mechanical loading with different levels of humidity. The applications of electrical loading, i.e., the permittivity changes with varing humidity, have attracted great interest. The first work, which strictly uses the electrical loading of the PVA film, was reported in 2013 [17], in which the PVA film was applied to a stepped impedance resonator and electric field coupled inductor capacitor resonator for RH sensing application. Wireless chipless RH sensing applications with PVA film were later reported in [18, 19]. RH sensor performances, e.g., the operation frequency and the bandwidth, are unable to be evaluated through simulations before implementing and measuring the sensors due to the lack of an accurate model for the PVA film. An effort was made to characterize dielectric properties of PVA film at different RHs with the results later proven through simulations [20]. However, only the real part of permittivity was extracted, and the PVA model for simulation was provided only for discrete characterized RH values. Moreover, humidity sensors only measure at limited RHs, regardless of the sensing principles [21]. The responses at the rest of these RH values either remain unknown or are interpolated using a first or second order polynomial curve based on the measured points [9,11,13]. The

mechanical loading property of PVA film considers the mass loading and the viscoelastic effect. At microwaves, the mechanical loading is applied mainly to surface acoustic wave (SAW) devices, e.g., the SAW resonators and delay lines [10,11]. With the mass loading and the viscoelastic effect of the PVA film changing with different RHs, the SAW velocity varies, which is measured through the resonant frequency or time delay. In optics the viscoelastic effect of the mechanical loading can also be apply to optical fibers for RH sensing [22, 23].

The main purpose of this work is to create accurate methods to obtain electrical information of materials to investigate the influence of different patterns and thicknesses of humidity sensitive films, and based on that, to apply novel structures to facilitate sensor design at microwave frequencies, in particular for wireless and non-intrusive sensing application. The novelties in this thesis can be summarized as follows:

- a method to measure moisture content in solid materials, using a resonant material characterization method at a single frequency,
- a comprehensive model created from broadband characterization results of PVA film to enable the prediction of the humidity sensor performances by using computer simulation tools,
- a wet chemical method of patterning PVA film and an investigation of the influence of PVA film thickness to facilitate the SAW resonator-based humidity sensor design with different performances,
- a dual-load humidity sensor based on a hybrid structure of an SAW resonator and interdigital capacitors (IDCs) as reflectors to apply both, the electrical loading and mechanical loading humidity sensing mechanisms of the PVA film at the same time.

In chapter 2, precise definitions of the term moisture and humidity are given. The three most common types of moisture and humidity sensors, i.e., capacitive, inductive, and mechanical loading types are introduced, and the sensing principles of each sensor type are explained. The sensing principles in this work are categorized as capacitive and mechanical loading.

In chapter 3, the cavity perturbation method is employed for the characterization of the moisture content of tobacco, using a rectangular waveguide resonator. A linear increased tendency between the mass of moisture content and the absolute complex permittivity and loss tangent are found. The dielectric information of the tobacco is used to design a

mass flow sensor which is an open resonator, consisting of two circular waveguides with different diameters.

In chapter 4, a PVA film is chosen as the sensitive layer for humidity sensing. An in-depth and thorough discussion of using the electrical loading property of PVA film for sensing applications will be given in this chapter. A broadband characterization of PVA film at different RHs is performed, and the complex permittivity is extracted at different RHs. A comprehensive model is created from the characterization results, which can be applied to computer simulation tools to predict the sensor performances. Based on this, a chipless, wireless humidity sensor is designed by using a PVA film. A good agreement between the simulation and measurement results of the wireless sensor proves the accuracy of the PVA model.

In chapter 5, methods of analyzing and designing SAW devices are introduced. SAW resonators are employed for humidity sensors design using the mechanical loading property of the PVA film. A wet chemical method of patterning PVA film is proposed, and the influence of the PVA film thickness is investigated. Different sensor performances can be achieved with various PVA film patterns and thicknesses.

In chapter 6, a novel hybrid structure of a one-port SAW resonator is designed combined with IDCs used as the reflectors. Based on this structure, a dual-load humidity sensor is designed, which employs both, the electrical and mechanical loading of the PVA at the same time for humidity sensing applications. A figure of merit (FoM) is defined in this chapter to simultaneously evaluate the sensitivity and quality factor of the sensor. By comparing the FoM of the two sensing mechanisms, the better one is used for humidity sensing in a defined RH range.

Chapter 2

Fundamentals of Moisture and Humidity Sensing

The term "moisture" generally refers to the water content of any material. Practically speaking, however, moisture is only applied to liquids and solids. For the water vapor content in gases, the term "humidity" is rather used. The most commonly used definitions for water content are moisture, absolute humidity, and relative humidity, which are introduced in the following [24]:

Moisture- the amount of water contained in a liquid or solid by absorption or adsorption, which can be removed without altering its chemical properties.

Absolute humidity- the mass of water vapor per unit volume of wet gas, which is the density of the water vapor in a wet gas.

Relative humidity (RH)- the ratio of the actual vapor pressure of the air at any temperature to the maximum saturation vapor pressure at the same temperature. It is usually expressed as a percentage in the following:

$$\mathrm{RH} = 100\frac{P_w}{P_s}, \tag{2.1}$$

where P_w is the partial pressure of water vapor, and P_s is the saturated water pressure at a given temperature.

To detect moisture or humidity, the effects that relate to the concentration of water molecules are applied. Three types of sensors are introduced in this chapter, which include capacitive, inductive, and mechanical loading. Capacitive sensors detect moisture or humidity by measuring the capacitance change as a result of the change of the permittivity of MUT under different moisture or humidity conditions. The conductive type of sensors reveals that the moisture or humidity changes the conductance of the MUT. Through resistance measurements, the conductance can be

detected, which carries the information of the moisture or humidity. Mechanical loading type of sensors detect the moisture or humidity through the change of mass loading or viscoelasticity of sensitive materials, which alter their own respective mechanical properties under different moisture or humidity levels.

2.1 Capacitive Sensors

Permittivity and permeability are two very important parameters used to define the electromagnetic properties of a material. Permittivity describes the interaction of a material with the electric fields applied to it. Permeability denotes the interaction of a material with magnetic fields applied to it. Electric and magnetic fields interact with the material in two different ways: energy storage and energy dissipation. Energy storage describes the lossless portion of the exchange of energy between the fields and the materials, whereas energy dissipation occurs when the material obsorbs electromagnetic energy. Both permittivity and permeability are expressed as complex numbers to describe the storage, i.e., the real part, and the dissipation, i.e., the imaginary part [6]. The mathematical expression of permittivity and permeability is written as:

$$\varepsilon = \varepsilon' - j\varepsilon'', \tag{2.2}$$

$$\mu = \mu' - j\mu''. \tag{2.3}$$

However, only permittivity is considered in the capacitive sensors, since the capacitance is dependent on the permittivity. For example, the capacitance of parallel plates can be calculated as

$$C = \varepsilon \frac{A}{d}, \tag{2.4}$$

where A is the area of overlap for the two plates, and d is the distance of the separation between the two plates.

The permittivity of a material is dependent on different physical phenomena, such as ionic conduction, dipolar relaxation, atomic polarization, and electronic polarization, which play the most important role in the permittivity of a dielectric material. The variation of permittivity in the microwave range, which is interested in this work, is mainly caused

by the dipolar relaxation of water molecules [6]. Different types of polarization of a material at microwave range can be described by the Debye theory, in which the complex permittivity can be calculated as [25],

$$\varepsilon - \varepsilon_\infty = \frac{\varepsilon_0 - \varepsilon_\infty}{1 + j\omega\tau_0}, \tag{2.5}$$

where ε_∞ is the infinite frequency relative permittivity, ε_0 is the static relative permittivity, τ_0 is a generalized relaxation time, and ω is the angular frequency, i.e., $\omega = 2\pi f$. By applying Eq. 2.5, the dielectric relaxation of de-ionized water can be calculated as in Fig. 2.1.

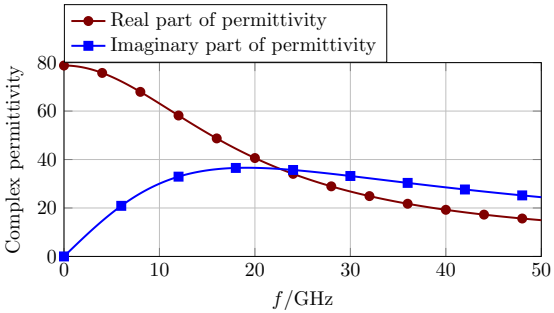

Figure 2.1: Dielectric relaxation of deionized water at 25°C.

It has been revealed that the real part of permittivity decreases with frequency. When the frequency is zero, the real part of permittivity is 78.8. When the frequency is infinite, the real part of permittivity is 5.6. The imaginary part of the permittivity first increases, reaching its the maximum value at 19.16 GHz, then decreases. The information of the water permittivity is useful for capacitive humidity sensors design. Based on the permittivity of dry MUT or sensitive layers, which both absorb and adsorb water molecules, the operation frequency of the sensors can be designed. The difference between the permittivity of the water, and MUT or sensitive layers determines whether the sensitivity of the sensor is large enough to fulfill the requirement of the design, while not introducing too much losses.

2.2 Conductive Sensors

For conductive sensors, the moisture or humidity is detected by measuring the conductance. The working principle of the conductive humidity sensors is illustrated in Fig. 2.2.

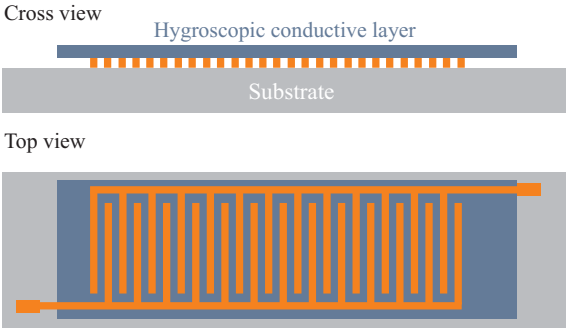

Figure 2.2: Cross and top view of a conductive humidity sensor.

The sensor is usually fabricated on a single side ceramic substrate, such as alumina with electrodes on top. The humidity sensitive material is loaded on top of the electrodes, which provides a large contact area for water molecules in the environment. The sensitive material used for the conductive sensors has the property of changing resistivity under different humidity conditions. When the sensitive layer adsorbs the water molecules, the resistivity between the electrodes changes, which can be measured by an electronic circuit.

2.3 Mechanical Loading Sensors

The mechanical loading type sensors utilize the special property of the materials that change the physical behavior such as mechanical wave velocity, with mechanical loading on top. One important application involves piezoelectric materials for humidity sensing. The piezoelectric material can generate acoustic wave when electromagnetic energy is coupled into the material. The velocity of the acoustic wave changes with mechanical loading on top of the piezoelectric substrate. By using this property, mechanical loading type sensors can be designed. The water

vapor can either be directly deposited onto the piezoelectric material, or a humidity sensitive film can be applied to the piezoelectric substrate to either absorb or adsorb the water vapor. A SAW resonator and a delay line based humidity sensors loaded with sensitive films are introduced here in Fig. 2.3.

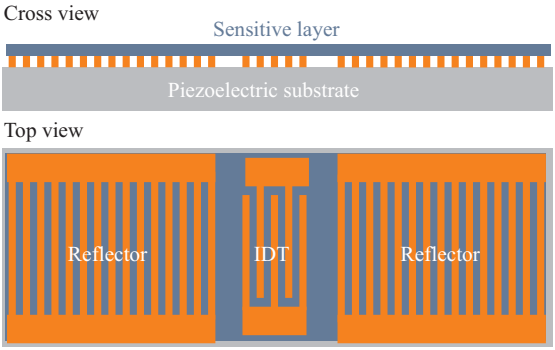

(a) Humidity sensor based on SAW resonator.

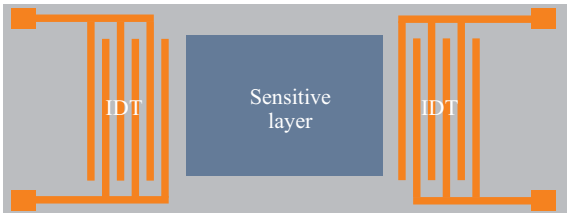

(b) Humidity sensor based on SAW delay line.

Figure 2.3: Mechanical loading type of humidity sensors based on a SAW resonator and a delay line.

Fig. 2.3a shows the SAW resonator based humidity sensor. The humidity sensitive layer is loaded on top of the structure. When the sensitive layer absorbs or adsorbs the water molecule based on the ambient humidity level, the mechanical loading of the layer changes and results in the change of the acoustic wave velocity. The frequency f is relative to the phase velocity (v), with a simple equation:

$$v = \lambda f. \tag{2.6}$$

By measuring the change of the frequency of the resonator, the humidity level can be detected.

Fig. 2.3b presents the SAW delay line based humidity sensor. The humidity sensitive layer is loaded between two interdigital transducers (IDTs), between which the acoustic wave travels. When the mechanical loading of the sensitive layer changes, the phase of the transmission parameter varies depending on the humidity level. A reference channel is sometimes necessary to suppress the temperature variation. The application details of the capacitive and mechanical loading type of sensors are given in later chapters.

Chapter 3

Characterization of Moisture in Tobacco

Material characterization of dielectric or magnetic materials can be performed through both, non-resonant and resonant methods. The latter usually have the advantages of higher accuracies and sensitivity compared to non-resonant methods, becoming more suitable for low-loss sample measurements [6]. Hence, a resonant method, i.e., the cavity perturbation method is used at a single frequency for the characterization of moisture in tobacco with low losses. In this chapter, 6 different brands of cigarettes and a Tobacco Substitution are characterized using the cavity perturbation method [7] at 1.5 GHz to extract the complex permittivity of the materials. A density-independent relationship of moisture content and complex permittivity is found through the analysis of the characterization results. The dielectric information of tobacco, which contains up to 11 % of moisture, is used for a mass flow sensor design. The sensor is made of an open cylindrical resonator that consists of two circular waveguides with various diameters. An on-sight test of the sensor is performed, where all of the measurements show a discrepancy within 10 % between the supplied and measured weights, which is sufficient in practical measurements.

3.1 Cavity Perturbation Method

The cavity perturbation method is widely used to characterize the electrical or magnetic behavior of materials, i.e. the complex permittivity. As the name of the method suggests, the material under investigation is inserted into a resonant cavity. There are two restrictions of the inserted material that must be fulfilled to satisfy the approximation of the permittivity calculation formulations. The sample must be very small compared to the resonant cavity structure, ensuring that the field doesn't change and that the insertion of the material sample only causes a small frequency shift compared to the resonant frequency of the empty cavity.

The material sample must be small, i.e., 1/10 or smaller compared to the wavelength in the cavity, or the unperturbed fields in the sample region must be uniform, due to the assumption that the fields in the sample are the solution of static problems [26]. If these restricted conditions are carried out, it can be concluded that the actual fields in a cavity with a perturbation sample are not greatly different from those in the unperturbed cavity. Accounting for other details is unnecessary, since these details are the same for the cavity with and without the sample and can be canceled out in the permittivity calculation equations.

Normally the material in the resonant cavity is characterized by a VNA, where the resonant frequency and quality factor can be measured and calculated from the scattering parameters. As is well known, the angular frequency ω is defined as $\omega = 2\pi f$, with f representing the ordinary frequency measured in Hz. When considering the dielectric loss of the material sample in the cavity, metallic loss of the cavity wall, and the coupling loss, a much easier expression is defined as a complex angular frequency [26]:

$$\omega' = \omega'_{\mathrm{r}} + j\omega'_{\mathrm{i}} = \omega(1 + \frac{j}{2Q_L}), \tag{3.1}$$

where Q_L is the loaded quality factor which calculates all of the mentioned losses.

The resonant frequencies and loaded quality factors of an empty resonant cavity and the cavity with an inserted sample material need to be measured. Through Eq. 3.1, the complex resonance frequencies of the empty cavity ω'_1 and the perturbed cavity with the sample material ω'_2 can be calculated. The difference between ω'_1 and ω'_2 normalized by ω'_2 is approximately expressed as [26]

$$\frac{\delta\omega'}{\omega'} \approx (\frac{f_{r2} - f_{r1}}{f_{r2}}) + j(\frac{1}{2Q_{L2}} - \frac{1}{2Q_{L1}}), \tag{3.2}$$

where f_{r2} and f_{r1} are the ordinary frequencies, Q_{L2} and Q_{L1} are the loaded quality factors with and without the material sample. Through Eq. 3.2, the measured quantities f and Q_L are connected to a theoretical expression of $\delta\omega'/\omega'$.

The Maxwell's equation in a lossless resonant cavity can be expressed as [27]

$$\nabla \times \bar{E} = -j\omega\mu\bar{H}, \tag{3.3}$$

$$\nabla \times \bar{H} = j\omega\varepsilon\bar{E}. \tag{3.4}$$

The electrical and magnetic field in the unperturbed cavity are noted as $\bar{E}_1$ and $\bar{H}_1$, and after inserting the material sample the electrical and magnetic field in the cavity are $\bar{E}_2$ and $\bar{H}_2$. By applying suitable dot product to Eq. 3.3 and Eq. 3.4, under the condition of an empty cavity and perturbed cavity through the subtraction of the modified equations and integrating over the cavity volume, the following equation can be obtained [26]

$$\int_{V_{cav}} (\omega_1' \varepsilon_1 \bar{E}_1 \cdot \bar{E}_2 - \omega_1' \mu_1 \bar{H}_1 \cdot \bar{H}_2) dV = \int_{V_{cav}} (\omega_2' \varepsilon_2 \bar{E}_1 \cdot \bar{E}_2 - \omega_2' \mu_2 \bar{H}_1 \cdot \bar{H}_2) dV. \tag{3.5}$$

where ω_1' and ω_2' are complex angular frequencies of the resonant cavity with and without the material sample.

In order to calculate Eq. 3.2 with the electrical and magnetic field in the cavity, Eq. 3.5 is subtracted from $\int_{V_{cav}} (\omega_2' \varepsilon_1 \bar{E}_1 \cdot \bar{E}_2 - \omega_2' \mu_1 \bar{H}_1 \cdot \bar{H}_2) dV$, and the normalized frequency difference can be calculated as [26]

$$\frac{\omega_2' - \omega_1'}{\omega_2'} = \frac{\int_{V_{cav}} \left[(\mu_2 - \mu_1) \bar{H}_1 \cdot \bar{H}_2 - (\varepsilon_2 - \varepsilon_1) \bar{E}_1 \cdot \bar{E}_2 \right] dV}{\int_{V_{cav}} (\varepsilon_1 \bar{E}_1 \cdot \bar{E}_2 - \mu_1 \bar{H}_1 \cdot \bar{H}_2) dV}. \tag{3.6}$$

Since the material sample used for the perturbation is assumed to be non-magnetic, the permeability in the empty cavity is equal to the permeability in the perturbed cavity with the same value as the permeability in the vacuum $\mu_1 = \mu_2 = \mu_0$. Following that, the first part of the numerator in the integral on the right side of Eq. 3.6 is zero. When the cavity is empty, the permittivity is equal to the permittivity of vacuum $\varepsilon_1 = \varepsilon_0$. After the sample is inserted in the cavity, the fields outside the perturbation area are considered not changing due to the assumption of the small size of the perturbed sample, i.e., $\varepsilon_2 = \varepsilon_1$. The second part on the right side of Eq. 3.6 is integrated over the sample area V_{smp} rather than the cavity area V_{cav}. Another assumption is made based on the small sample size, $\bar{E}_1 = \bar{E}_2$ and $\bar{H}_1 = \bar{H}_2$ in the denominator of Eq. 3.6. Although a small error is introduced in the sample area, it is negligible. The denominator in Eq. 3.6 is the integral of $\left|\bar{E}_1\right|^2$. Under all of these conditions, Eq. 3.6 is simplified as [26]

$$\frac{\omega_2' - \omega_1'}{\omega_2'} = \frac{-(\varepsilon_2 - \varepsilon_0) \int_{V_{smp}} \bar{E}_1 \cdot \bar{E}_2 dV}{2\varepsilon_0 \int_{V_{cav}} \left|\bar{E}_1\right|^2 dV} = \frac{-(\varepsilon_{r2} - 1)}{2} \frac{\int_{V_{smp}} \bar{E}_1 \cdot \bar{E}_2 dV}{\int_{V_{cav}} \left|\bar{E}_1\right|^2 dV}, \tag{3.7}$$

where ε_{r2} is the complex relative permittivity of the perturbed sample needed to be characterized. Equation 3.7 connects the theoretical expression of $\delta\omega'/\omega'$ to the electrical field, volume of the cavity and the sample and the relative complex permittivity of the material sample.

Based on the discourse proven above, a theoretical expression of $\delta\omega'/\omega'$ is the bridge connecting the measurement results and the electrical field in the cavity together. By substituting $\delta\omega'/\omega'$ in Eq. 3.2 with the expression in Eq. 3.7, the complex relative permittivity can be calculated as [26]

$$\varepsilon_{r2} = 1 + \left[2(\frac{f_{r1} - f_{r2}}{f_{r2}}) - j(\frac{1}{Q_{L2}} - \frac{1}{Q_{L1}})\right] / \frac{\int_{V_{smp}} \bar{E}_1 \cdot \bar{E}_2 dV}{\int_{V_{cav}} \left|\bar{E}_1\right|^2 dV}, \quad (3.8)$$

where the electrical field in the empty cavity $\bar{E}_1$ is presumed to be known, and the field after the perturbation of the sample material $\bar{E}_2$ is unknown and dictated by the cavity and sample shape.

3.2 Characterization of Tobacco

Tobacco production is one of the leading industrial branches worldwide. Due to high quality demands, the fabrication process of cigarettes is of great interest [28]. The moisture content of tobacco is a very important factor in cigarette production, which needs to be controlled to a certain extent. For instance, if the moisture content is too high, tobacco becomes a nutrient medium for molds and reduces the quality. Moreover, if it is too dry, tobacco becomes hard and brittle and will end up as powder under slight stress. The most used techniques for moisture measurements are oven techniques, which measure the mass of the sample before and after drying in the oven. The moisture content M in this specific case is calculated as

$$M = \frac{m_w}{m_w + m_d}, \quad (3.9)$$

where m_w is the mass of water content, and m_d is the mass of dry material [29]. If the volume of the material is known, the moisture content in Eq. 3.9 can be calculated as

$$M = \frac{m_w/V}{(m_w/V) + (m_d/V)} = \frac{k}{k+g} = \frac{k}{\rho}, \quad (3.10)$$

where V is the given volume of the MUT, and k, g and ρ are the density of the water, dry material and moist material, respectively [29]. Equation. 3.10 demonstrates that the moisture content depends on the

density of the water content and the moist material. However, the oven techniques suffer from the long time measurement duration and the lack of real time measurement ability. If Eq. 3.10 is applied for the moisture calculation, the changes and fluctuations in the amount of MUT cause similar responses to the changes of moisture content [29]. Due to the shape of the material, e.g., tobacco or grain, the measurement error is unavoidable. Therefore, a density independent expression, i.e., the relationship between the electrical property of the MUT and the moisture content, becomes a more suitable and reliable solution. There are many methods for a density independent moisture measurement, including measurement by using an open dielectric resonator pair, frequency swept transmission, and a microwave free space technique [30]. Many density independent expressions have been derived, e.g., the moisture content of wheat [29, 31].

In order to obtain the density independent expression of the moisture content in tobacco, a resonant cavity is built to investigate the complex permittivity of different cigarette blends at a single frequency, which is the operation frequency of the mass flow sensor using the introduced CPM. The results are related to the tobacco's moisture content, measured by a commercial moisture analyzer, and a linear expression between the moisture content and the permittivity of the tobacco is observed.

3.2.1 Measurements of Moisture Content and Weight

The moisture content of 6 different cigarette brands with various tobacco qualities and fabrication techniques from the world's biggest cigarette suppliers, and a Tobacco Substitution, which is the unblended tobacco without any taste, are analyzed. The tobaccos used for the measurements are extracted from processed cigarettes. To measure the moisture content, 2.5 g tobacco is extracted from the cigarettes of each brand. The Kern MRS Moisture Analyzer with a precision of less than 0.05 % of the relative moisture content is used to measure the moisture content of the tobacco from each brand, and the results are shown in Fig. 3.1. A large change in moisture content from 9.76 % to 12.22 % is found among different brands. The measured tobacco with the highest moisture content is the Tobacco Substitution, and the one with the lowest moisture content is Camel. The measurement results coordinate with the usual moisture content of tobacco in the range of 10 % to 14 % [32–34].

The weight measurements are carried out by a scale with a resolution of 0.1 mg. For the weight measurements, the filters of the cigarettes

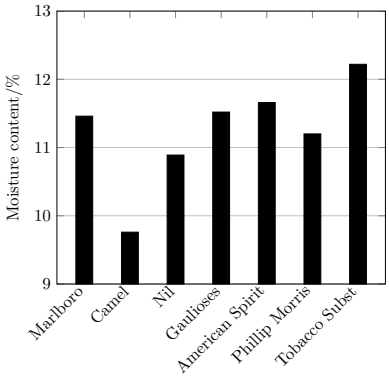

Figure 3.1: Moisture content measurement results of 6 brands of tobacco and a Tobacco Substitution.

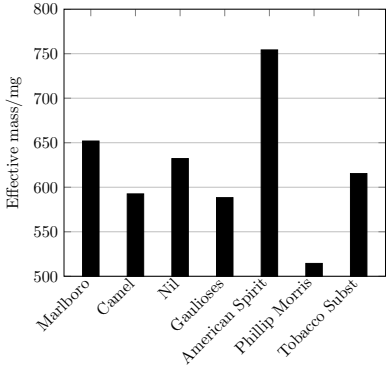

Figure 3.2: Effective mass measurement results of 6 brands of tobacco and a Tobacco Substitution.

are removed, and the measurement results are normalized to the height of a sample holder which is used to carry the tobacco to the cavity resonator for the permittivity characterization. The normalized weight of the tobacco samples is then averaged and defined as effective mass shown in Fig. 3.2. The results vary from 514.4 mg to 754.2 mg, indicating that the density of the cigarette brands is different. The effective mass of most brands is around 600 mg. The heaviest brand is American Spirit

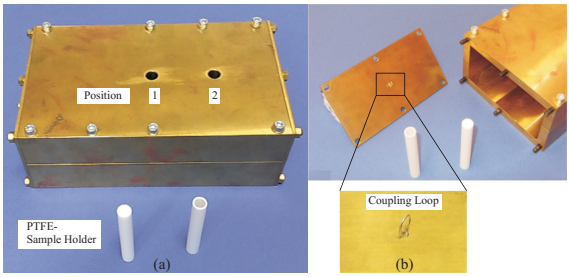

Figure 3.3: Resonant cavity for complex permittivity and loss tangent measurements at 1.5 GHz and 2 GHz.

with a value of 754.2 mg, and the lightest is Phillip Morris which weights 514.4 mg.

3.2.2 Detection of Permittivity and Loss Tangent

After measuring the weight and the moisture content of the tobacco, a rectangular waveguide resonator is built for the permittivity and loss tangent characterization as shown in Fig. 3.3.

The resonant cavity is made of brass with the shape of a German standard R22 rectangular waveguide (British standard WG 8) shorted in both ends. It is 110 mm wide, 55 mm high, and 210 mm long. Two holes are created on the top face of the cavity to place the sample, which are labeled as position 1 and 2. The extracted tobacco is carried by a cylindrical polytetrafluoroethylene (PTFE) sample holder into the resonant cavity through one of the holes in Fig 3.3a. The sample holder has an outer diameter of 10 mm, an inner diameter of 8 mm, and a permittivity of 2.05. The electromagnetic wave is coupled into the cavity by two small loops, which join in the middle of the two opposite side faces as shown in Fig. 3.3b. The cavity is designed to work at 2 different modes, and the field distribution of each mode is shown in Fig. 3.4.

The picture in the top left corner in Fig. 3.4 shows the side view of the electric field of H_{101} mode. The length of the cavity equals to half of the wavelength at 1.526 GHz. The picture in the bottom left corner shows the top view of the magnetic field of H_{101} mode working at 1.526 GHz. The two pictures in the right half of Fig. 3.4 are the side and top views of the electric and magnetic fields of H_{102} mode at 1.965 GHz, which show

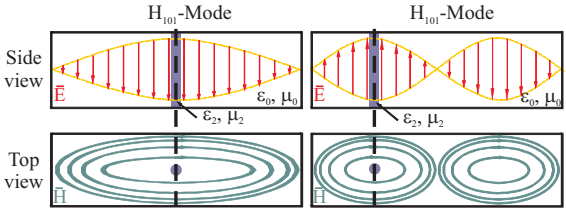

Figure 3.4: Field distribution of two resonant modes: H_{101} mode at 1.526 GHz and H_{102} mode at 1.965 GHz with electric field shown in the side view and magnetic field shown in the top view of the rectangular resonant cavity.

that the length of the cavity equals to the wavelength at 1.965 GHz. The rectangular structures with dash lines cutting through the middle represent the dielectric rods, which need to be characterized. The positions of the dielectric sample in the cavity are shown in Fig. 3.3, with position 1 representing the H_{101} mode and position 2 the H_{102} mode application. In this work, the H_{101} mode is used to measure the permittivity and loss tangent of the tobacco at 1.526 GHz.

Compared to the cavity and wavelength, the samples are created to be very small, so that the unperturbed field in the sample region is almost uniform. These restricted conditions are well satisfied in order to use the cavity perturbation method. The electric field in the upper half of Fig. 3.4 is tangential all the way to the surface of the sample due to the cylindrical shape of the sample holder. Since the electric field continues over the boundary, the electric field in the dielectric sample $\bar{E}_2$ and the electric field outside near the sample $\bar{E}_1$ express as

$$\bar{E}_2 = \bar{E}_1. \tag{3.11}$$

Substituting Eq. 3.11 into Eq. 3.8, the complex relative permittivity of the material sample can be calculated with the measurement results and dimension of the sample holder and cavity, which is

$$\varepsilon_{r2} = \varepsilon'_{r2} - j\varepsilon''_{r2} = 1 + \left[2(\frac{f_{r1} - f_{r2}}{f_{r2}}) - j(\frac{1}{Q_{L2}} - \frac{1}{Q_{L1}})\right] \frac{V_{cav}}{V_{smp}}, \tag{3.12}$$

where f_{r1} and Q_{L1} are the resonant frequency and loaded quality factor of empty cavity, f_{r2} and Q_{L2} are the resonant frequency and loaded quality factor of the perturbed cavity with tobacco sample. V_{smp} is the volume of the cylindrical sample holder, and V_{cav} is the volume of the

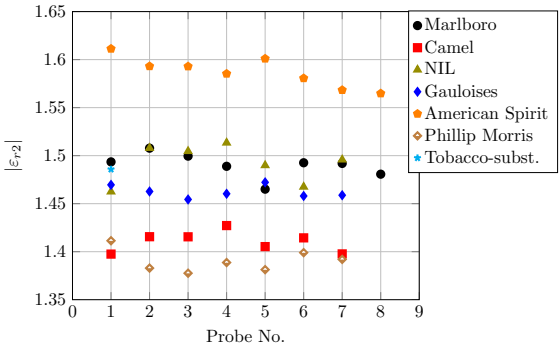

Figure 3.5: Absolute complex permittivity of different cigarette brands.

rectangular cavity. ε'_{r2} and ε''_{r2} are the real and imaginary parts of the complex relative permittivity. The loss tangent of the material sample is calculated as

$$tan\delta = \frac{\varepsilon''_{r2}}{\varepsilon'_{r2}}. \tag{3.13}$$

For each brand of cigarette, up to 8 samples are measured. After calculating with Eq. 3.12, a result of absolute complex relative permittivity is shown in Fig. 3.5. Different brands have various absolute permittivity, and the values vary from 1.375 to 1.625. The brand of American Spirit achieves the highest value, while the permittivity of Phillip Morris is the lowest. The absolute complex permittivity of the Tobacco Substitution has the value of 1.48, which can be used as test material for the microwave mass flow sensor design due to the fact that most of the cigarette brands have an effective permittivity between 1.4 and 1.5.

The loss tangent of the tobacco of each cigarette brand is calculated through Eq. 3.13 with the characterization results shown in Fig. 3.6. In general the loss of the tobacco measures from 0.0435 to 0.0798. American Spirit has the highest loss among all of the brands, while Camel and Phillip Morris both yield a relatively low loss. Most of the tobacco bands have loss tangent between 0.065 and 0.08, which can be substituted by the Tobacco Substitution with a value of 0.067 in a sensor design. From both Fig. 3.5 and Fig. 3.6, it can be seen that the changes of the dielectric property of each measured sample are very small, measuring within 5 %. The brands with the higher absolute permittivity tend to have higher a loss tangent.

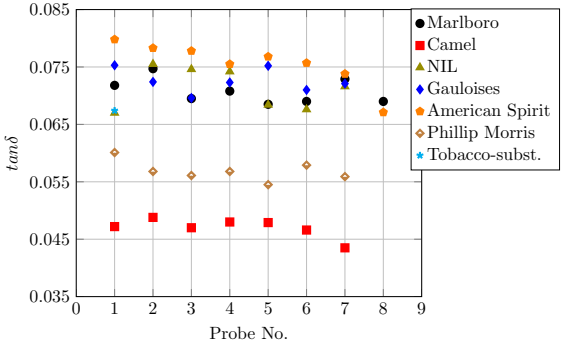

Figure 3.6: Loss tangent of different cigarette brands.

3.2.3 Density Independent Result

The moisture contents of all of the cigarettes brands measured in this work are between 9.76 % and 12.22 %, which is typical for tobacco production. The mass of the water content in different brands of cigarettes can be obtained from the measurement results shown in Fig. 3.1 and Fig. 3.2. The calculated complex permittivity of 6 brands of cigarettes and the Tobacco Substitution are related to the mass of the water content, and the results of the absolute relative permittivity and loss tangent are shown in Fig. 3.7. Both of the absolute relative permittivity and the loss tangent versus the absolute moisture show a linear behavior. The result exhibits that the difference of the absolute relative permittivity and the loss tangent of each brand of tobacco are dominated by the mass of water content.

3.3 Mass Flow Sensor Application

There are many principles which have been used to detect the mass flow, e.g., mechanical methods, electrostatic methods, microwave methods, acoustic methods and optical methods [35, 36]. The mass flow sensors using microwave methods have the advantage of non-intrusive measurement, as well as straightforward and efficient installation. These simply require transceivers to measure the moving particles, with concentration of solids determined by an injecting and back-scattered signal [37]. The velocity measurement of solids, however, is not possible due to poor

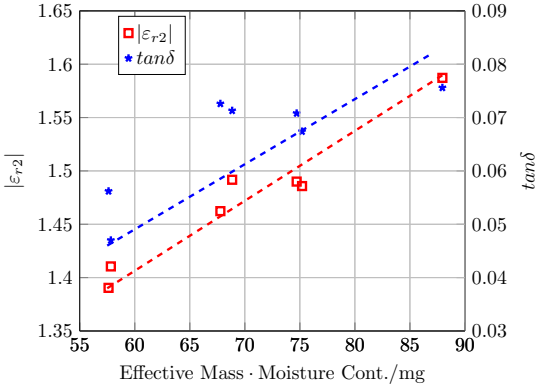

Figure 3.7: Relationship between the electric properties and mass of water content of 6 brands of cigarettes and Tobacco Substitution.

transceiver signals. Another method is based on spatial filtering velocimetry for mass flow detection of particulate solids, which can perform both material concentration and velocity measurement [38]. This type of sensor has been well researched in [39], the idea currently being used as inspiration for the design of tobacco mass flow sensor.

3.3.1 Sensor Structure

When a material is inserted into a resonator, the resonance frequency, phase and quality factor are changed by perturbation. The mass flow sensor design is a modification of a circular resonator, which is perturbed by the MUT. Instead of having a static material perturbation, the material moves through the resonator. This effect requires an open resonator. In most of the application cases, the particulate materials travel through a pipeline, a circular pipe is used as a waveguide for microwaves. The cutoff frequency of a circular waveguide, f_c, which is defined as the frequency below which no propagation of electromagnetic wave occurs in the waveguide, is calculated as [27]

$$f_c = \frac{p_{nm} v_{phase}}{2\pi r}, \tag{3.14}$$

where v_{phase} is the phase velocity of the microwave traveling in the waveguide, and r is the radius of the circular waveguide. If there are no electric fields in the wave traveling direction, transverse electric (TE) waves are propagating in the waveguide, p_{nm} is the mth root of derivative of first kind Bessel function. Different values of p_{nm} result in different f_c, and the waves in the waveguide propagate in certain patterns defined as various TE modes. If there are no magnetic field propagating in the wave traveling direction, the waves are defined as transverse magnetic (TM) waves. p_{nm} is the mth root of first kind Bessel functions, which determines the different TM modes.

The first mode that can propagate in the circular waveguide is the TE_{11} mode, defined as the fundamental mode. It has the smallest cutoff frequency among all of the TE and TM modes. The cutoff frequencies of the first few TE and TM modes are shown in Fig. 3.8. When the frequency increases, more modes will be excited causing interferences between one other for the sensing application. In the tobacco mass flow sensor application, only the TE_{11} mode is used by carefully designing the radius of the circular waveguide and the feeding method.

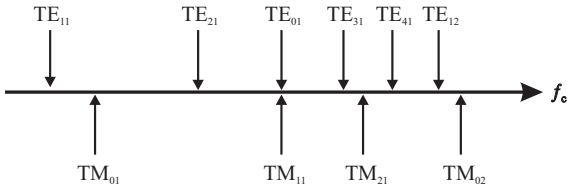

Figure 3.8: Cutoff frequencies of first a few TE and TM modes.

Pipelines are usually used to convey tobacco in the industry. For a typical application, the pipeline radius is 60 mm. When used as a waveguide, e.g., in Eq. 3.14, the cutoff frequency of this pipeline is $f_{cp} = 1.465$ GHz. The sensor is also designed based on a circular waveguide, as a means to replace the pipeline without causing any disturbances in the transmission of the tobacco. If the cutoff frequency of the circular waveguide for the sensor is designed to be below 1.465 GHz, the waves can then be excited in the sensor but stopped in the pipeline. The waves are trapped in the sensor forming an open resonator. A cross section of the sensor is shown in Fig. 3.9

Since the sensor is working below the cutoff frequency of the pipelines, the radius of the sensor is larger than the radius of the pipelines. A

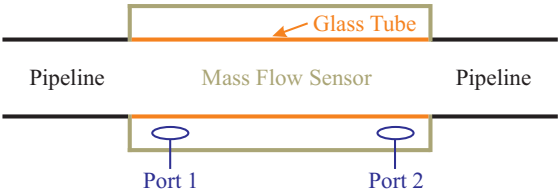

Figure 3.9: Cross section of mass flow sensor with glass tube for tobacco sensing application.

Borosilicate glass tube is implemented in the sensor cavity to ensure the undisturbed transmission of tobacco. As noted in Port1 and Port2 of Fig. 3.9, small loop antennas excited the wave in the sensor. In order to only use the fundamental mode in the sensor, the length must be carefully designed. An algorithm is thus developed to find the optimal radius and the length of the sensor.

3.3.2 Optimum Sensor Design Criteria

The resonant frequency TE_{nml} mode of a closed circular resonator is calculated as [27]

$$f_{nml} = \frac{c}{2\pi\sqrt{\mu_r \varepsilon_r}} \sqrt{(\frac{p_{nm}}{r})^2 + (\frac{l\pi}{d})^2}, \tag{3.15}$$

where c is the speed of light in the vacuum, μ_r and ε_r are the relative permeability and permittivity of the material in the resonator, respectively, and d is the length of the resonator.

To form an open circular resonator working at TE_{11} mode, the resonance frequency of the sensor f_{11l} needs to be smaller than both the cutoff frequency of the pipelines f_{cp} and that of the second mode of the sensor f_{cs}, which is TM_{01} from Fig. 3.8. The available dimension of the sensor is solved using two inequations

$$\begin{cases} f_{11l} < f_{cp} \\ f_{11l} < f_{cs}. \end{cases} \tag{3.16}$$

When the glass tube in Fig. 3.9 is not considered, the radius and length of the sensor can be solved by substituting Eq. 3.14 and Eq. 3.15 into

the inequation set 3.16, which are:

$$\begin{cases} \frac{d}{l} > \pi / \sqrt{\frac{\varepsilon_{rs}}{\varepsilon_{rp}} (\frac{p_{11}^{\mathrm{TE}}}{r_p})^2 - (\frac{p_{11}^{\mathrm{TE}}}{r_s})^2} \\ \frac{d}{l} > \pi / \sqrt{(\frac{p_{01}^{\mathrm{TM}}}{r_s})^2 - (\frac{p_{11}^{\mathrm{TE}}}{r_s})^2}. \end{cases} \tag{3.17}$$

$\frac{d}{l}$ is the length of the sensor per mode, ε_{rs}, r_s and ε_{rp}, r_p are the relative permittivity and radius of the sensor and pipelines, respectively. The p_{11}^{TE} is the first root of derivative of first kind Bessel function, and p_{01}^{TM} is first root of first kind Bessel function. Fig. 3.10 shows the solved feasible dimensions of the sensor. The curve of $\varepsilon_{rp} = 1$ is the boundary of the sensor dimension in the case of an empty tobacco conveying pipe. The area above the boundary curve is the feasible dimension combination which is suitable for the design in this condition. When the conveying pipe is partially filled with tobacco, taking place when some tobacco is left after transport, the relative permittivity is assumed to be 1.09. The feasible dimension for the sensor design is the area above the curve of $\varepsilon_{rp} = 1.09$ in Fig. 3.10. In the extreme case that the conveying pipe is completely filled with tobacco, the boundary of the dimension is shown by the curve of $\varepsilon_{rp} = 1.48$, with the relative permittivity of Tobacco Substitution.

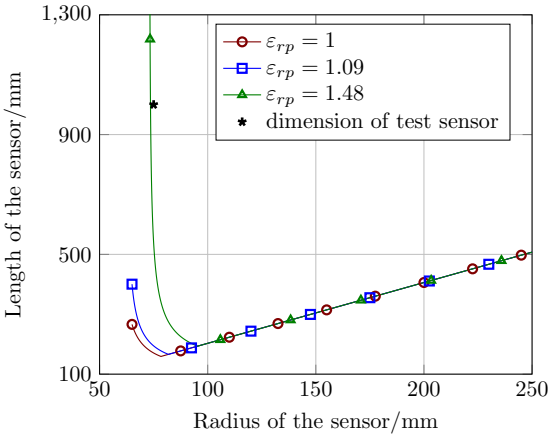

Figure 3.10: Feasible radius and length for mass flow sensor design.

A preliminary test is done with the sensor structure reported in [39]. The sensor is 1 m long with a radius of 75 mm, shown in Fig. 3.11 (a).

According to the feasible dimension shown in Fig. 3.10, the locus of the sensor dimension is within the safe area for the sensor to resonate in the extreme case. Two SMA connectors are soldered with small loops to feed the electromagnetic energy into the resonant cavity as shown in Fig. 3.11 (b) and (c). The two flanges with a radius of 60 mm at both ends of the sensor are used to connect the conveying pipe for tobacco transport. A glass tube with the same radius as the flanges is placed concentrically into the sensor, which is used to convey the tobacco through the sensor.

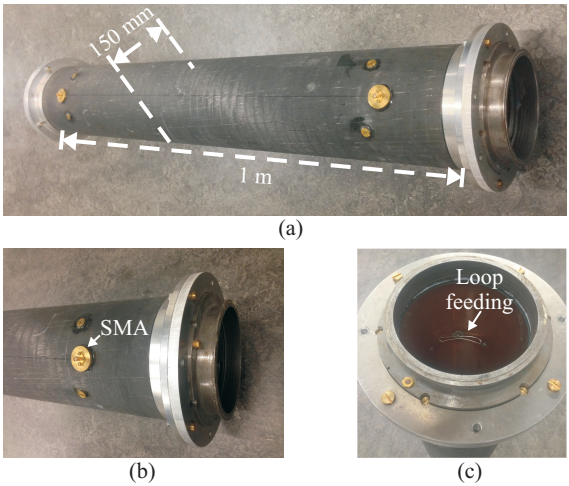

Figure 3.11: Tobacco mass flow sensor for the preliminary test, (a) over view, (b) SMA connector for signal input, (c) Loop feeding for excitation.

A graphical user interface (GUI) is designed and compiled from Matlab for the tobacco mass flow measurement as shown in Fig. 3.12. Some preliminary information needs to be given before the measurement. The permittivity and the density are already extracted from the tobacco characterization, and the lowest and highest velocities of the tobacco flow are provided by the cooperative partner. The online mode is for the real time measurement of the tobacco mass flow, and the results will be saved in the given file name. The concentration, velocity, and mass flow of the tobacco can be measured with the sensor, and the real time measurement results are shown in the three charts. In the end, a total mass is calcu-

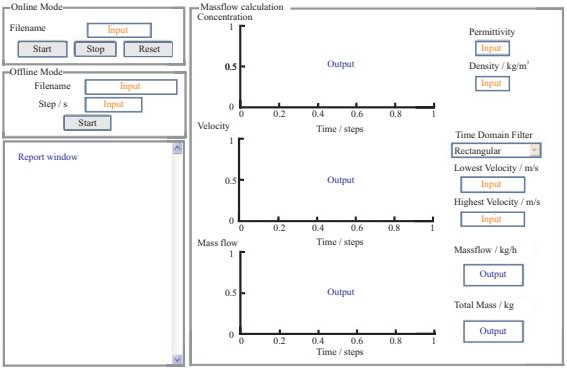

Figure 3.12: Graphical user interface for mass flow sensor.

lated for users within a certain supplied time. An offline mode function is added to the GUI, ensuring users to review all of the measurement results for further analysis.

An on-sight test of the sensor is performed at Riedel–Filtertechnik GmbH, which is a cooperative project partner. The sensor is implemented in their pneumatic tobacco conveying system with the radius of the pipeline of 60 mm. Four distinct measurements are obtained by feeding different weights of tobacco to the mass flow sensor in different time duration, e.g., 1 kg tobacco is fed into the mass flow sensor in 10 min and 20 min,

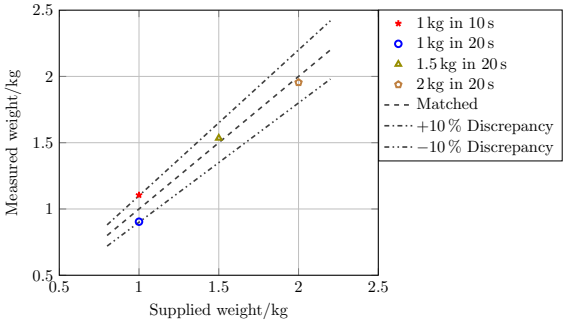

Figure 3.13: Four measurement results of the mass flow sensor with different supplied weight and time.

and 1.5 kg and 2 kg tobacco are fed into the sensor in 20 min. The measurement results are shown in Fig. 3.13. The dashed line is the ideal case in which the measurement results and the supplied weight are matched. The ±10 % discrepancy curves are the dot dashed and double dots dashed line in Fig. 3.13. These four measurement results are within a 10 % discrepancy.

Chapter 4

Relative Humidity Sensing Using Electrical Loading

In chapter 3, an effective method, the cavity perturbation method was discussed to characterize the moisture content of a solid material at a single frequency. However, nowadays the water content in gases such as air, which is known as humidity, is also of great interest. To sense the humidity, polyvinyl alcohol is employed due to its advantages of good sensitivity, easiness of process and low price. The PVA film exhibits two main characteristics for RH sensing application, which are the change of mechanical and electrical loading, i.e., the permittivity changes with RH, which will be discussed in details in this chapter. An in-depth discussion of using the mechanical loading property of PVA film for sensing applications will be given in chapter 5.

First, the method of broadband complex permittivity characterization of PVA film is introduced, and the results are extracted at different RHs from 13.7 % to 94.3 % over a frequency span from 1.5 GHz to 15 GHz. Then the hysteresis and long interval performance of the PVA film is investigated and reported. The extracted permittivities at different RHs show properties of dielectric relaxation, which can be described by the Cole–Cole equation. The coefficients in the Cole–Cole equation are calculated at different RHs. Functions of the coefficients over RH are found, by which the permittivity can be obtained at an arbitrary RH. For the first time, a comprehensive model of the PVA film is evaluated and proven as an accurate mathematical model for RH sensing applications. Second, a chipless, highly sensitive, low profile, low cost and easily fabricated passive wireless relative humidity sensor is designed based on PVA film. The sensor consists of a narrow band loop antenna loaded with the PVA film coated on an IDC at 2.85 GHz. The RH sensor generates an amplitude peak at resonance in the radar cross section (RCS), which changes with different RH. Simulations are done by applying the comprehensive model

of the PVA film to the sensor structure. The comparison of the measurements and simulation results shows good agreement, which proves the accuracy of the PVA model.

4.1 Polyvinyl Alcohol Film Characterization

In this section, the dielectric properties of PVA film is desired to be characterized in a broad frequency range, which can be used in computer simulation tools to facilitate the sensors design. Different structures exist for broadband material characterization, e.g., coaxial transmission lines, waveguides, coplanar waveguide (CPW) lines and IDCs. For the characterization of thin films, uniplanar structures like CPW and IDC are suitable due to the large exposed surface of film to the experiment environment. Considering costs, losses and manufacture difficulties of the devices, sensing RH is preferred at frequencies below 10 GHz. Since CPW lines show inevitable calibration errors at low frequencies (less than 1 GHz) [40], an IDC is used to perform the measurement with the PVA film loaded on top. To extract the material electrical properties over a broad frequency band, a mathematical model of the measurement structure is mostly used. In this work, the IDC is covered with PVA film which fit the model of a multilayered IDC. The multilayer structure is first separated into several single-layer substrates using the partial capacitance technique in [41], where the total capacitance is the sum of the capacitances of each separated single-layered IDC. To calculate the total capacitance, the single-layered IDC is transformed into a parallel plate capacitor by applying the conformal mapping method [42]. The permittivity extraction is done by comparing the admittance of the IDC extracted from measurement results to the mathematical IDC model.

The main purpose to characterize the PVA film is to obtain a more comprehensive model, so that the response of the sensors at an arbitrary RHs can be obtained. It has been shown that the permittivity of PVA film at different RHs exhibits dielectric relaxation especially at high RH [20]. There are different equations to describe the dielectric relaxation. The classical theory is the Debye theory, which is used to describe the effect for polar dielectrics [25]. Later an empirical formula, Cole–Cole equation, involving a single new constant based on experimental data was discovered as an improvement for Debye theory [43]. Different concentrations of PVA aqueous solutions have been studied at various temperatures, and it has been found that the permittivity of the aqueous solution follows the Cole–Cole equation [44–46]. Therefore, in this work

the Cole–Cole equation is applied to describe the humidity dependent PVA film permittivity.

In this section, a thorough investigation is performed for which the PVA film is characterized in a wide frequency range from 1.5 GHz to 15 GHz. A mathematical model of PVA film loaded IDCs is derived using partial capacitance techniques and conformal mapping method. Frequency dependent complex permittivities are extracted by comparing the admittance of the IDC calculated from measurement results and from the conformal mapping results. The hysteresis of the PVA film is investigated by experiments, and a long interval stability study of the PVA film is performed by comparing the characterization results of PVA films manufactured in 2013 and 2015, respectively. The characterization results are fitted to the Cole–Cole equation in order to reveal the dielectric relaxation property of the PVA film at different RH. The Cole–Cole coefficients are obtained using a nonlinear regression fitting algorithm of the characterization results. They are functions of RH values and follow exponential equations and polynomials. The coefficients of the Cole–Cole equation at an arbitrary RH can be calculated by the function, which provides the capability for RH sensing application. The low hysteresis and the stable long interval performance prove the PVA film as a good candidate for RH sensing applications.

4.1.1 Interdigital Capacitor Design and PVA Film Preparation

To ease the fabrication process and keep the self resonance frequency above the characterization band, an IDC is carefully designed for the characterization. The PVA film as the sensitive layer is prepared and loaded on top of the IDC structure.

Interdigital Capacitor

The fabricated IDC is shown in Fig. 4.1. The IDC has 10 gold finger pairs. The width of the fingers, the gaps between them and the gaps at the end of the fingers are 30 µm. The length of overlapped fingers is 215 µm, and the width of the interconnection bars is 75 µm. The uncertainty between the dimension of the design and fabricated structure is neglected, since the difference is in the nm range. The structure is realized on a 700 µm glass substrate with a constant relative permittivity of 4.47 and loss tangent of 0.025 within the frequency range of interest [47]. First, the glass is coated with 20 nm chromium adhesion and

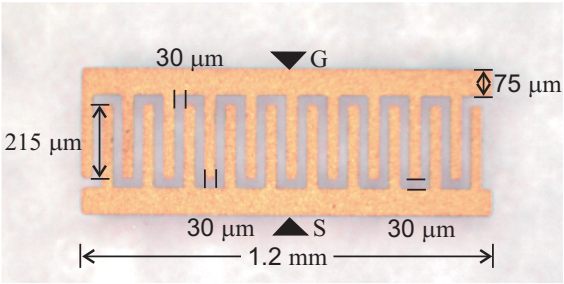

Figure 4.1: Microscopic image of the fabricated IDC for PVA characterization purpose with the designed parameters.

100 nm gold seed layer patterned with photoresist AZ6632. In a second step, the gold seed layer is electroplated to obtain a gold metallization with a thickness of 3.13 µm. Finally, the seed and the adhesion layers are removed using gold and chromium etchants. The self resonant frequency of the IDC is 62.69 GHz, which is far above the frequency band used for characterization. The radiation effects of the IDC from simulation can be neglected, since the radiation loss is almost 30 times smaller than the metallic loss.

PVA Film Preparation and Humidity Sensing Mechanism

PVA is a hygroscopic polymer of high molecular weight with a glass transition temperature about 70°C, and it has an –OH group bonded to each carbon in the backbone chain [11]. A 20 % PVA water solution is spin-coated on the IDC, and the structure is baked at 60°C for 20 min in open air to dry the PVA film. The thickness of the PVA film after spin-coating measured by a profilometer is 4.5 µm, which is sufficient to fully cover the IDC electrodes.

When the humid gas contacts the PVA film surface, water molecules in the humid gas are adsorbed through hydrogen bonding on two adjacent –OH groups of PVA molecules. This layer of water molecules cannot move freely due to the restriction from the two hydrogen bonding, which is called physically-adsorbed layer. When water keeps condensing on the surface of the PVA film, more layers are formed on top of the first layer with one hydrogen bond. These layers are less ordering, and the water molecules are mobile [48]. Due to the baking process, pores are created in the film. When the humidity increases, the physical adsorption not only takes place on the surface of the PVA film, but also along sites available

on the thickness of the film. At higher RH, multilayer adsorption of water occurs which penetrates deeper inside the film [49]. The adsorption stops when equilibrium is reached between the PVA film and environment. The time to reach the equilibrium is frequency independent.

4.1.2 Permittivity Extraction with a Multi-layer Structure

After deposition of the PVA film on top of the IDC as shown in Fig. 4.2, the device under test has 3 dielectric layers: an infinite air layer, a PVA film layer and a glass substrate layer. In this sandwich structure, the IDC electrodes are between the PVA film and the glass substrate. Two adjacent electrodes have the same electrical potential, but 180° phase difference. Under the assumption of an infinite periodic structure and infinite finger length, the electric field lines orthogonally cross the perpendicular planes, which are located in the middle between two adjacent electrodes. These planes have zero voltage, thus forming a virtual ground shown as dashed lines in Fig. 4.2. $\varepsilon_{r,\mathrm{Air}}$, $\varepsilon_{r,\mathrm{PVA}}$ and $\varepsilon_{r,\mathrm{Glass}}$ are the complex relative permittivities of the dielectric multi-layer structure given in [27]

$$\varepsilon_r = \varepsilon_r' - j\varepsilon_r'', \tag{4.1}$$

where ε_r' and ε_r'' are the real and imaginary part of relative permittivity, j is the imaginary unit.

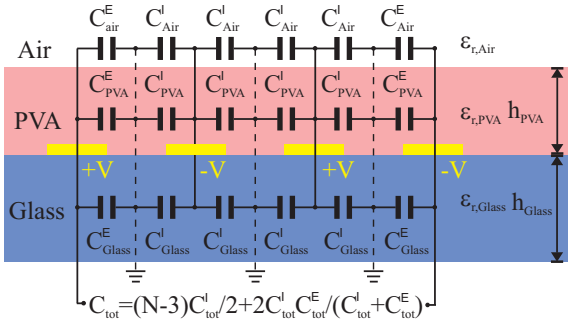

Figure 4.2: Equivalent circuit of the IDC three-layer sandwich structure with an example of four electrodes.

h_{PVA} and h_{Glass} are the thickness of the PVA film layer and the glass substrate, respectively. C^{I} stands for half of the capacitance between one interior electrode and the virtual ground, and C^{E} is the capacitance between one outer electrode and the virtual ground. The total capacitance of the structure is calculated as [50]

$$C_{\mathrm{tot}} = (N-3)\frac{C^{\mathrm{I}}_{\mathrm{tot}}}{2} + \frac{2C^{\mathrm{I}}_{tot}C^{\mathrm{E}}_{\mathrm{tot}}}{C^{\mathrm{I}}_{\mathrm{tot}} + C^{\mathrm{E}}_{\mathrm{tot}}}, \qquad N > 3. \tag{4.2}$$

According to the partial capacitance technique [41], the sandwich structure with finite dielectric layers in Fig. 4.2 can be separated into three individual dielectric layers. Both $C^{\mathrm{I}}_{\mathrm{tot}}$ and $C^{\mathrm{E}}_{\mathrm{tot}}$ can be calculated as the summation of the capacitance in each individual layer as

$$C^{\mathrm{I/E}}_{\mathrm{tot}} = C^{\mathrm{I/E}}_{\mathrm{Air}} + (\varepsilon_{r,\mathrm{PVA}} - 1)C^{\mathrm{I/E}}_{\mathrm{PVA}} + \varepsilon_{r,\mathrm{Glass}}C^{\mathrm{I/E}}_{\mathrm{Glass}}, \tag{4.3}$$

where $C^{\mathrm{I/E}}_{\mathrm{Air}}$, $C^{\mathrm{I/E}}_{\mathrm{PVA}}$ and $C^{\mathrm{I/E}}_{\mathrm{Glass}}$ are the interior and exterior capacitance in each individual layer, which are dependent on h_{PVA}, h_{Glass} and the electrode geometry [50]. The mathematical description of the sandwich IDC structure is derived by substituting Eq. 4.3 to Eq. 4.2 with the only unknown parameter of the PVA film permittivity. The admittance of the IDC calculated from C_{tot} is

$$Y^{\mathrm{CM}}_{\mathrm{IDC}} = j\omega C_{\mathrm{tot}}, \tag{4.4}$$

where ω is the angular frequency.

The reflection parameter of the IDC without PVA film S^{Bare}_{11} and with PVA film S^{Loaded}_{11} are measured by using a VNA. The metallic loss of the IDC is considered as a resistor, which is connected in parallel to the capacitor with parallel resistance of the glass dielectric loss. It is assumed that the metallic loss of IDC does not change with the loading of the PVA film. The total loss of the IDC without the PVA film is calculated by

$$Y^{\mathrm{Loss}}_{\mathrm{IDC}} = \mathrm{Real}(Y^{\mathrm{Mea}}_{\mathrm{IDC,Bare}}) = \mathrm{Real}\left(\frac{1}{Z_0}\cdot\frac{1-S^{\mathrm{Bare}}_{11}}{1+S^{\mathrm{Bare}}_{11}}\right) \tag{4.5}$$

from the measurement, where Z_0 is the characteristic impedance of the measurement system. After removing the total loss from the admittance of loaded PVA film $Y^{\mathrm{Mea}}_{\mathrm{IDC,Loaded}}$ and comparing the results with the admittance $Y^{\mathrm{CM}}_{\mathrm{IDC}}$ calculated from conformal mapping method, the complex permittivity of PVA film can be extracted:

$$Y^{\mathrm{Mea}}_{\mathrm{IDC,Loaded}} - Y^{\mathrm{Loss}}_{\mathrm{IDC}} = Y^{\mathrm{CM}}_{\mathrm{IDC}}. \tag{4.6}$$

A validation of this method is performed by extracting the permittivity of the glass substrate. The real part of the relative permittivity has an average value of 4.6 in the range of 1.5 GHz to 15 GHz, which confirms the results reported in [47, 51].

4.1.3 Measurement System and Experimental Setup

To measure the PVA film coated IDC, a climate chamber is required to provide adjustable steady RH and access to the RF measurement device, is required. The minimum measurement time duration needs to be determined to have a steady RH in the climate chamber, and a stabilized electrical response of the PVA loaded IDC. From the measurement results, the complex permittivities can be extracted at different RHs. To test the suitability of PVA film for RH sensing application, the hysteresis and long interval stability are studied as well.

Measurement Setup

The block diagram of the measurement setup is shown in Fig. 4.3a. It contains two parts: humid gas generation and on-wafer measurement setup. In the humid gas generation part, a commercial humidifier generates water vapor by ultrasonic vaporization of de-ionized water, which is adjusted by a controller. The vapor is mixed with dry nitrogen in the gas mixer where an adjustable valve is implemented to control the nitrogen flow and precisely adjust the RH. The measurements are carried out using an on-wafer probe station. Fig. 4.3b shows the experimental measurement setup. The humid gas is fed into the climate chamber, where the RH and the temperature is monitored by a commercial sensor with a RH resolution of 0.1 % and temperature measurement resolution of 0.1°C. The response of the PVA film covered IDC, i.e., the reflection parameter S_{11} is measured by a VNA. The VNA is connected to a signal ground (SG) port in Fig. 4.1. The calibration of the VNA is performed by employing a commercial calibration substrate, which sets the reference plane to the tip of the on-wafer probe.

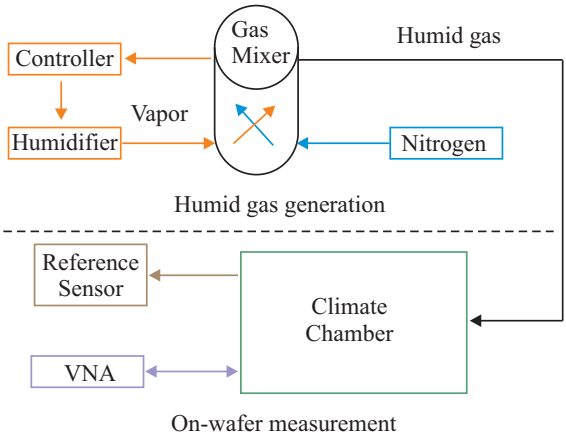

(a) Block diagram of RH measurement system.

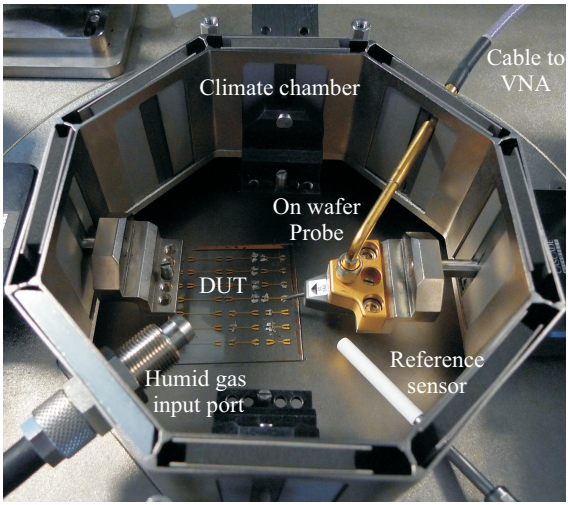

(b) Measurement setup in a climate chamber.

Figure 4.3: Measurement system and experimental setup.

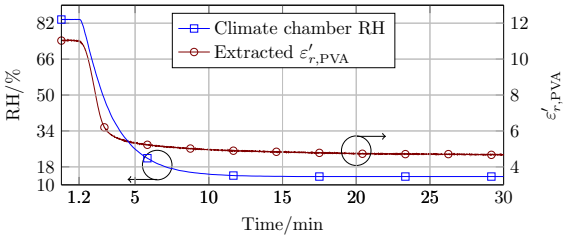

Figure 4.4: Test of exposure time of a PVA film coated IDC at 8 GHz in the RH measurement system with a change of RH from 83.6 % to 13.7 %.

In the measurement, the SG probe directly contacts the middle of the IDC as shown in Fig. 4.1. Since the probe is contacted to the IDC manually, the applied contact force differs slightly for each measurement. This is the major measurement uncertainty. To estimate this uncertainty together with the fabrication and VNA uncertainty which is much smaller than the repeatability-induced uncertainty, 30 unloaded IDCs with the same structure are measured. The maximum standard deviation of the real part of the glass relative permittivity, normalized to the mean value, is 2.5%. The maximum standard deviation of the imaginary part of the glass relative permittivity is 7.4%, and it drops to 3% above 5 GHz. The temperature in the climate chamber is stabilized between 22.7°C and 22.8°C by a water cooling system during the measurements.

Measurement Time Duration

In order to obtain the response time for the measurement, a 70 % RH change is tested from 83.6 % down to 13.7 %. The step of the humidity change is significantly larger than in any subsequent measurements, e.g., the characterization, hysteresis and long interval stability study. The time response of RH in the climate chamber and extracted permittivity are shown in Fig. 4.4. First, the RH in the climate chamber is constant at 83.6 %, which is recorded by the reference sensor. The time response of the IDC covered with PVA film is measured by the VNA at 8 GHz for 30 min. Then, the RH is turned to 13.7 % after 1.2 min. The RH in the climate chamber is steady at 13.7 % RH after 15 min. Both real and imaginary part of the extracted relative permittivity are stabilized after 20 min. In order to observe the results clearly, only the real part of relative permittivity ε'_r is shown in Fig. 4.4, which is stabilized at the value of 4.6. Hence, the exposure time is fixed at 20 min for all following

characterization measurement of PVA film.

4.1.4 Characterization Results

The complex permittivity of a PVA film is extracted by the method discussed before in the frequency range from 1.5 GHz to 15 GHz. The PVA film is characterized at 10 different RHs from 13.7 % to 94.3 %. The values of extracted permittivities at low RH and high RH have large difference. In order to reveal the characteristics clearly, 5 of the characterization results at 13.7 %, 56.2 %, 76.4 %, 83.0 % and 94.3 % RH are shown in Fig. 4.5. The real part ε_r' of the complex permittivity in upper half of Fig. 4.5 exhibits two major properties. It shows dielectric relaxation especially at higher RH, e.g., at 83 % and 94.3 %. The permittivity increases with the increased RH, and when the RH is above 50 %, the increase rate of permittivity is higher compared to the RH below 50 %. The lower half in Fig. 4.5 shows the imaginary part ε_r'' of the complex permittivity, which represents the loss of the material. It is evident that the loss of the material increases with the RH, due to the fact that the water vapor absorbed by the PVA film is very lossy in the microwave range. When the RH increases, more water vapor is absorbed by the film, which increases the loss indicated by a larger ε_r''. The error bars in Fig. 4.5 present the standard deviation of the characterization results at different RH levels.

4.1.5 Hysteresis Effects of PVA Films

To study the hysteresis of the PVA film at low, medium and high RHs, a series of measurements is performed with the same PVA film covered IDC used for the characterization. The RH in the climate chamber is first adjusted to lowest value of 13.7 %. After measuring the response of the IDC, the RH is increased to medium RH value of 56.2 % and high RH value of 83.0 %, and the responses are measured, respectively. After the response at 83.0 % is measured, the RH in the climate chamber is further increased to 94.3 % which is used as the starting point for the backward measurement. When the electrical response is steady at 94.3 % RH, the RH in the climate chamber starts to decrease. The first backward measurement is at 83.0 % to compare with the response at same value measured forward. Then, the RH is continually decreased to 56.2 % and 13.7 %. The real part ε_r' of the permittivity is extracted from each measurement, and the results for the same RH values measured forward

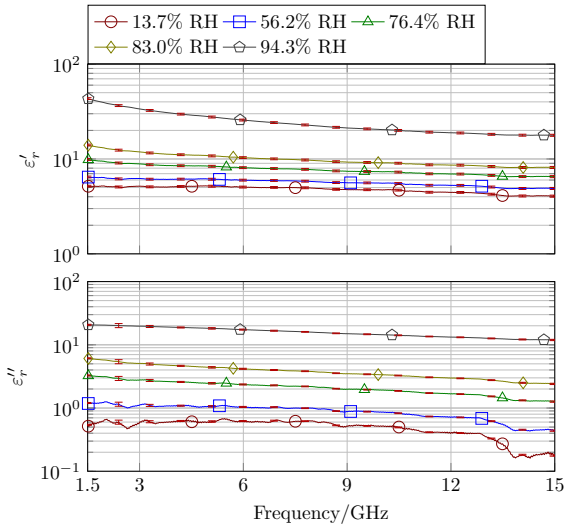

Figure 4.5: Broadband permittivity characterization results of PVA film at different RHs with error bars in red presenting measurement uncertainty.

and backward are compared in the left half in Fig 4.6. It can be conclude that at 13.7 % and 56.2 % RH, the forward and backward results agree to each other. At 83.0 % RH, the two curves show slight difference. In order to evaluate the differences, a relative difference δ between two extracted permittivities from the measurements is defined as

$$\delta = \frac{\varepsilon'_{r2} - \varepsilon'_{r1}}{\varepsilon'_{r1}}. \tag{4.7}$$

The relative difference δ_{hys} between forward and backward measurement at 13.7 %, 52.6 % and 83 % RH are calculated by the Eq. 4.7, respectively. The extracted permittivities from forward increasing RH measurements are ε'_{r1}, and the extracted permittivities from backward deceasing RH measurements are ε'_{r2}. The results are shown in the right half in Fig. 4.6, respectively. It can be seen that δ_{hys} at low, medium and high RH are positive. It means that the ε'_{r2} is larger than ε'_{r1} due to the hysteresis between absorption and desorption of the PVA film. Among the three RH levels, the maximum value of δ_{hys} is 1.7 % at 13.7 % RH. The small

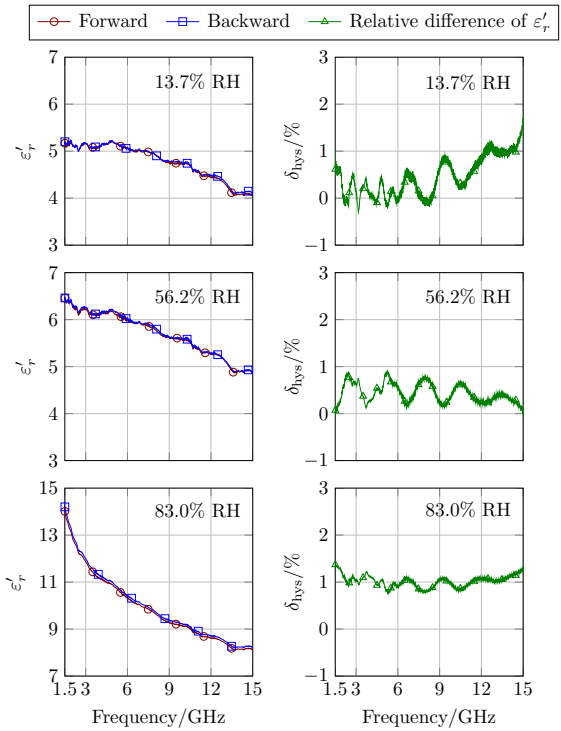

Figure 4.6: Hysterisis study by comparing the extracted real part of the permittivity ε'_r from the forward and backward measurement results at the low, medium and high RH (left) and calculation results of relative difference δ_{hys} between the extracted ε'_r measured forward and backward at the same RH value (right).

value of δ_{hys} at all measured RH levels prove that the PVA film has little hysteresis for relative humidity sensing.

4.1.6 Long Interval Stability of PVA Films

The long interval stability of PVA film for RH sensing is investigated by using two PVA films with the same thickness of 4.5 µm. One of the

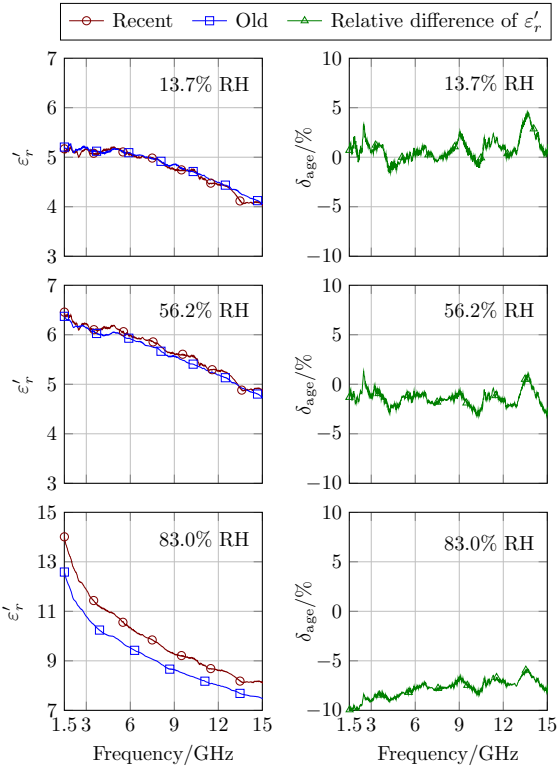

Figure 4.7: Long interval stability study by comparing the extracted real part of the permittivity ε'_r from the measurement results of recent and old PVA film sample at the low, medium and high RH (left) and calculation results of δ_{age} between the extracted ε'_r of the recent and old PVA film sample measured at the same RH value (right).

PVA film is recently produced by the procedure introduced in before in 2015, the other one is an old PVA film produced in 2013 with the same procedure. The PVA solution is stored in a light tight fridge with the temperature of 9°C since it was opened. Both films are loaded on the same IDC structure, and measured at three different RHs 13.7 %, 56.2 % and 83.0 %. ε'_r is extracted from the measurement results which is shown in the left half of Fig 4.7. The curves of ε'_r agree to each other at 13.7 %

and 56.2 % RH, and at 83.0 % a difference between the extracted results of recent and old film is noticeable.

To describe the difference between the results of recent and old PVA film sample at same RH, a relative difference δ_{age} is calculated by Eq. 4.7. ε'_{r1} is the extracted real part of relative permittivity from measurement result of recent produced sample, and ε'_{r2} is the extracted real part of permittivity from measurement of old PVA sample. The results at low, medium and high RH are shown in the right half in Fig. 4.7 respectively. The maximum relative difference between recent produced and old sample at 13.7 % RH is 4.47 %, and at 56.2 % RH the maximum relative difference is −3.14 %. At high RH of 83 %, the maximum relative difference is −10.16 %. Hence, after two years, the performance of the PVA film at low and medium RH is stable, and at high RH the relative difference is acceptable in practice.

4.1.7 Cole-Cole Modeling of the Characterization Results

The characterization results of PVA film in Fig. 4.5 show dielectric relaxation property. In order to find a more comprehensive model to describe the relaxation property of the PVA film, the Cole–Cole equation is employed [43], which describes the material dispersion as

$$\varepsilon_r = \varepsilon_{r\infty} + \frac{(\varepsilon_{rs} - \varepsilon_{r\infty})}{1 + (j\omega\tau_0)^{1-\alpha}}. \tag{4.8}$$

Here, ε_{rs} is the static relative permittivity, i.e., limiting low-frequency permittivity, and $\varepsilon_{r\infty}$ is the infinite frequency relative permittivity, i.e., limiting high-frequency permittivity, τ_0 is a generalized relaxation time and α is a curve constant with a value between 0 and 1 indicating the broadness of the symmetric relaxation curve [43, 44].

To calculate the Cole–Cole coefficients at different RHs, the real and imaginary part of permittivity of the PVA film from the characterization results are used to estimate the coefficients by a nonlinear least squares fitting algorithm. An example of Cole–Cole dispersion at 94.3 % RH is shown in Fig. 4.8. The complex relative permittivity of the PVA film at 94.3 % RH is used to fit the Cole–Cole equation with error bars on the characterization results representing the measurement uncertainty. The coefficients after fitting are $\varepsilon_{r\infty} = 7.69$, $\varepsilon_{rs} = 75.78$, $\tau_0 = 83.72\,\text{ps}$ and $\alpha = 0.3254$. A conclusion can be drawn from Fig. 4.8 that the fitted results and the characterization results of both real and imaginary part

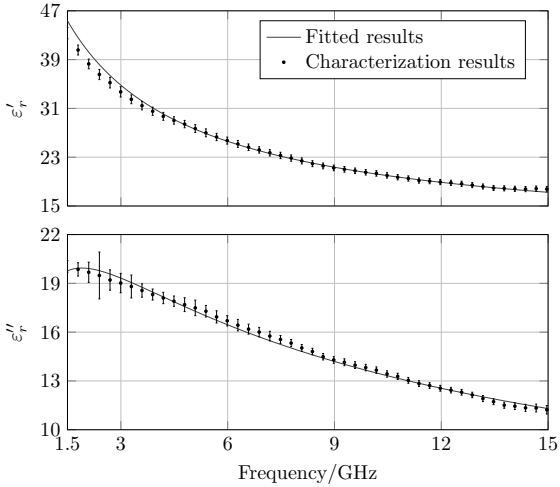

Figure 4.8: Characterization results with error bars and Cole–Cole equation fitted results of a PVA film at 94.3 % RH, where ε_r' is the real part of permittivity and ε_r'' is the imaginary part of permittivity.

of relative permittivity agree well. To evaluate the fitting process, a relative mean square error (MSE) is defined as

$$\mathrm{MSE} = \frac{1}{N}\sum_{i=1}^{N}\frac{|y_i - f_i|^2}{|y_i|}, \tag{4.9}$$

where y_i is the observed data value, f_i is the predicted value from the fitting, and N is the number of samples used in the fitting. At 94.3 % RH, the $\mathrm{MSE_p}$ in Eq. 4.9 is 0.028 %, where the observed data is the extracted complex permittivity from characterization, and the predicted value is the fitted permittivity from Cole–Cole equation.

The coefficients of the Cole–Cole equation at different RHs are shown in Table 4.1. The high frequency permittivity decreases with RH from 7.69 to 4.57, and the static permittivity decreases from 75.78 to 4.63. The relaxation time decreases with RH from 83.72 to 9 ps, and the curve constant decreases from 0.3254 to 0.017. Below 39.4 % RH the changes of all the coefficients in Table 4.1 are very small. The maximum $\mathrm{MSE_p}$ among all relative humidity levels is 1.03 % at 13.7 % RH. Above 22.7 %

Table 4.1: Fitted parameters of Cole–Cole equations of PVA film at different RHs

RH	$\varepsilon_{r\infty}$	ε_{rs}	τ_0/ps	α	$\mathrm{MSE_p}$
94.3 %	7.69	75.78	83.72	0.3254	0.028 %
83.0 %	7.40	19.94	83.40	0.1679	0.16 %
76.4 %	6.93	12.37	82.93	0.0523	0.28 %
65.7 %	6.15	8.39	82.00	0.0180	0.46 %
56.2 %	5.47	6.27	46.86	0.0180	0.50 %
47.5 %	5.19	5.48	37.34	0.0180	0.65 %
39.4 %	4.78	4.83	13.25	0.0173	0.83 %
30.6 %	4.67	4.71	10.64	0.0171	0.87 %
22.7 %	4.63	4.65	9.20	0.0170	0.88 %
13.7 %	4.57	4.63	9.00	0.0170	1.03 %

RH the $\mathrm{MSE_p}$ is smaller than 1 %. The small $\mathrm{MSE_p}$ at all RHs proves that the Cole–Cole equation can describe the dispersive properties of PVA film well.

For sensing applications, the relative humidity in the climate chamber can only be set to discrete values for the characterization. To obtain the coefficients of Cole–Cole equation at an arbitrary RH environment, the coefficients in Table 4.1 are fitted over the whole range of RH from 13.7 % to 94.3 %, where the fitting functions are given below:

$$\varepsilon_{r\infty} = 4.47 \cdot 10^{-4} \cdot \mathrm{RH}^2 - 4.73 \cdot 10^{-3} \cdot \mathrm{RH} + 4.45 \qquad \mathrm{RH} \in [13.7\,\%, 94.3\,\%] \tag{4.10}$$

$$\varepsilon_{rs} = 3.75 \cdot 10^{-5} \cdot \exp(0.15 \cdot \mathrm{RH}) + 3.56 \cdot \exp(0.01 \cdot \mathrm{RH}) \qquad \mathrm{RH} \in [13.7\,\%, 94.3\,\%] \tag{4.11}$$

$$\tau_0/\mathrm{ps} = 38.45 \cdot \tanh(0.076 \cdot \mathrm{RH} - 4.067) + 46.96 \qquad \mathrm{RH} \in [13.7\,\%, 94.3\,\%] \tag{4.12}$$

$$\alpha = \begin{cases} 2.45 \cdot 10^{-5} \cdot \mathrm{RH} + 1.65 \cdot 10^{-2} \\ \qquad\qquad \mathrm{RH} \in [13.7\,\%, 65.7\,\%) \\ 2.99 \cdot 10^{-4} \cdot \mathrm{RH}^2 - 3.67 \cdot 10^{-2} \cdot \mathrm{RH} + 1.14 \\ \qquad\qquad \mathrm{RH} \in [65.7\,\%, 94.3\,\%] \end{cases} \tag{4.13}$$

It can be observed from Eq. 4.10 to Eq. 4.13 that the coefficients of the Cole–Cole equation are functions of relative humidity. The fitted curves of the four coefficients of Cole–Cole equations together with the fitting data from Table 4.1 are plotted as functions of relative humidity in Fig. 4.9. The maximum error between the fitted curves and the fitting data of the Cole–Cole equation is evaluated by the maximum relative MSE defined in Eq. 4.9. The observed data y_i in Eq. 4.9 is the coefficient obtained at measured RHs shown in Table 4.1, and the predicted data f_i is the fitted result. The MSE of $\varepsilon_{r\infty}$ is 0.067 %, MSE of ε_{rs} is 0.38 %, MSE of τ_0 is 1.31 % and MSE of α is 2.57 %. The small MSE between the fitting data and the fitted results shows good agreement among all four coefficients.

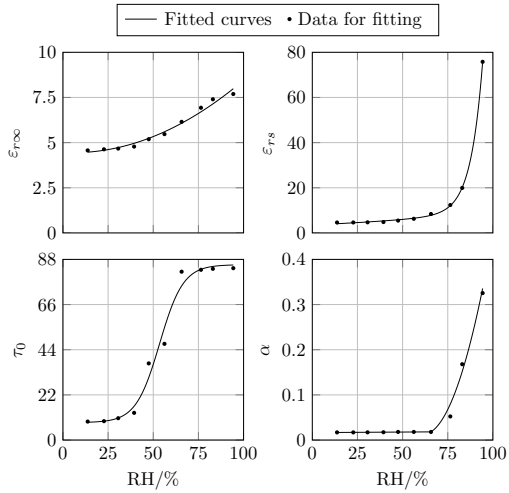

Figure 4.9: Curves of four Cole–Cole equation coefficients as functions of relative humidity compared with discrete data for fitting Cole–Cole equation .

4.2 Wireless RH Sensor Application

Wireless humidity sensors were investigated quite intensively in recent years for applications such as climate control, biomedical survey and harsh environment monitoring, etc. Researches have been carried out on e.g. single-chip integrated humidity sensor [52], and surface acoustic wave sensors [53]. However, these sensors have complex manufacture procedure and need extra antennas, which raise the cost. Therefore, a chipless, highly sensitive, low profile, low cost and easily fabricated wireless relative humidity sensor based on PVA film is designed for the humidity sensing. In the implementation, a loop antenna is designed to transmit data and form a part of the sensor structure, and a PVA film loaded IDC is used as the RH sensing element and tunes the antenna to 2.85 GHz. The sensor is interrogated remotely by a reader antenna, and the measurement results show a good sensitivity up to 5.35 MHz/%RH above 50 % RH. The sensor structure is also simulated with CST Microwave Studio with the PVA film model by the Cole–Cole equation used in the simulation. The simulation results of the sensor at the same RH points are compared to the measurement results. Very good agreement between two results are found with the maximum absolute different of 15.45 MHz and relative difference of 0.543 %. This has proven the accuracy of the PVA film model, which can be used as a trustworthy tool for the RH sensor design.

4.2.1 Sensing Concept

The basic sensing principle is shown in Fig. 4.10. A reader generates a frequency-sweeping interrogation signal, which illuminates the RH sensor in the climate chamber. The sensor first receives the signal and generates an amplitude peak at resonance in the radar cross section amplitude spectrum. Then the signal is scattered back, and then, received by the reader. When the RH in the climate chamber changes, the water content of the PVA film changes as well, which results in different permittivity of the film. Since the PVA film is loaded on top of the IDC, the capacitance of the IDC changes. Therefore, the resonant frequency of the sensor is tuned by the IDC. Thus, the changing resonant frequency carries the information of the RH.

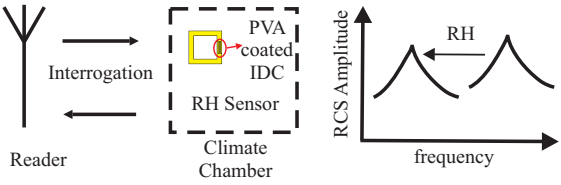

Figure 4.10: Radar cross section sensing principle overview.

4.2.2 Sensor Design and Realization

The sensor is composed of a loop antenna and a 2-finger pair IDC illustrated in Fig. 4.11. As substrate, Rogers 5880 material is used with a relative permittivity of 2.2 and thickness of 381 µm, which is shown in Fig. 4.11(a). The metallization of the sensor structure is realized on a 17 µm thick copper layer.

Considering the efficiency in the frequency band, the PVA film is spin-coated only on top of the IDC with the rest of the structure protected by transparent tapes. The structure is baked at 60°C for 30 minutes in the open air to cure the PVA film [11]. After removing the tapes, the PVA film is measured by the Dektak Mechanical Profilometer with the thickness of 3 µm as shown in Fig. 4.11(b). The realized sensor structure is shown in Fig. 4.11(c).

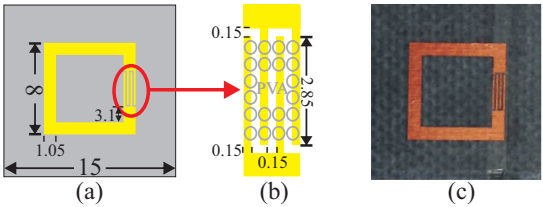

Figure 4.11: Sensor structure with all dimensions in millimeter: (a) sketch of the sensor, (b) PVA film coated IDC and (c) realized sensor.

4.2.3 Measurement Setup and Measurement Results

The RH measurement is performed with the setup in Fig. 4.12. A broadband horn antenna is used as the reader antenna with its operating frequency range from 0.75 GHz to 18 GHz, which has an average again of 10 dB around the target frequency range of 2 GHz to 3 GHz. The sensor is placed in a polystyrene foam box, which is 12 cm away from the reader antenna. At the bottom, humid gas with different humidity is fed into the box through the humid gas input port. A commercial sensor is used as the reference RH sensor with a RH resolution of 0.1 %, which is placed within the box to measure relative humidity as shown in Fig. 4.12(a). When the box is closed, it forms a small climate chamber with adjustable RH to characterize the frequency response of the RH sensor in the target frequency range as in Fig. 4.12(b).

The measurements are performed by a VNA connected to a reader antenna. Differential measurements (S_{rcs}) are carried out. The reflection parameter of the environment (S_{ref}) not including the sensor is measured, and used as reference data. Then, the sensor tag is place inside the climate chamber with every setup remaining its position, and the reflection parameter (S_{sen}) is measured which contains the relative humidity information. The S_{rcs} at different RH can be calculated by subtractions of S_{ref} from S_{sen}:

$$S_{\mathrm{rcs}} = S_{\mathrm{sen}} - S_{\mathrm{ref}}. \tag{4.14}$$

The resonant frequency of the bare structure without RH film coating is 2.891 GHz and the quality factor is 170. After the film is coated on the IDC, the sensor is characterized from 14 % to 91 % RH at 21°C, and the corresponding reflections are shown in Fig. 4.13.

To reveal the feature of the response, 3 reflections at RH of 14 %, 71 % and 91 % are highlighted with marks, and the rest are all in gray. When the RH increases from 14 % to 91 %, the resonant frequency of the sensor decreases from 2.85 GHz to 2.74 GHz. Due to the loss of water content, the amplitude at the resonance drops by 13.5 dB.

One of the key factor to evaluate the sensor performance is the sensitivity. Here an average sensitivity η of the RH sensor is defined as the ratio of the decrease of resonant frequency at two adjacent RH (f_1, f_2) divided by the increase of the two adjacent RH (RH_1, RH_2) :

$$\eta = \frac{|f_1 - f_2|}{|RH_1 - RH_2|}. \tag{4.15}$$

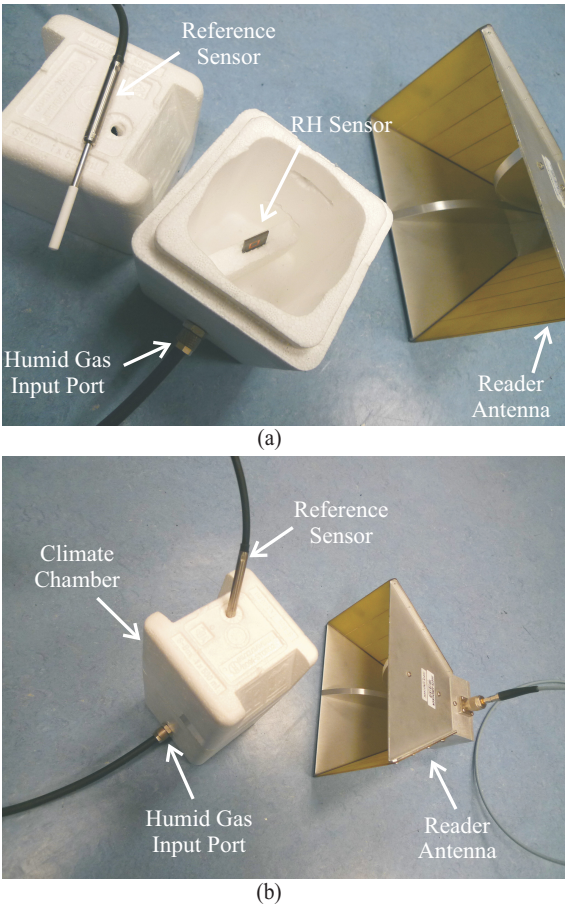

Figure 4.12: Relative humidity measurement setup: (a) overview of the setup and (b) setup in operation.

The results of resonant frequency of the sensor versus the RH values and the average sensitivity in between each two adjacent RH values are shown in Fig. 4.14.

The average sensitivity increases with the relative humidity. From 14 % to 48 % RH, the average sensitivity is 0.147 MHz/%RH, i.e., rather low.

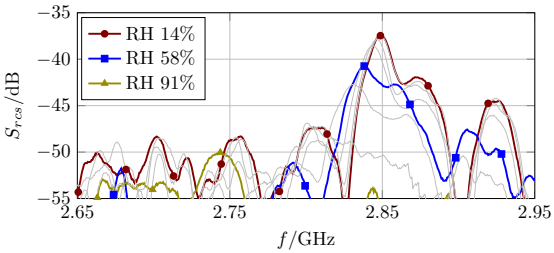

Figure 4.13: Reflection of the sensor at RH from 14 % to 91 %.

After 50 % RH, the sensitivity increases considerably. From 58.2 % to 79.4 % RH, the sensitivity is already 1.5 MHz/%RH. From 79.4 % to 91.2 %, the sensitivity is even 5.35 MHz/%RH. This is due to the fact that at high RHs, the permittivity of the PVA film changes more than at low RHs, which is in agreement with the characterization results in Fig. 4.5.

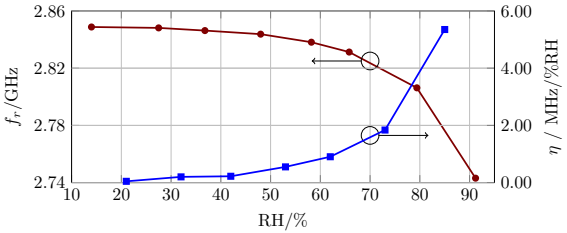

Figure 4.14: Resonant frequency and average sensitivity of the sensor at RH from 14 % to 91 %.

4.2.4 Sensor Performance Simulation

The sensor structure is simulated with CST Microwave Studio to prove the accuracy of the PVA model introduced in chapter 4.1. In the simulation, a transverse electromagnetic (TEM) wave is generated from a waveguide port and propagates towards the sensor with the magnetic field of the wave perpendicular to the sensor plane as shown in Fig. 4.15, which simulates the function of the broadband horn antenna used in the measurement.

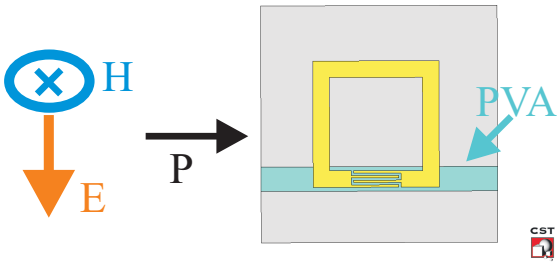

Figure 4.15: Sensor structure modeled in CST Microwave Studio.

In simulation, a 3 µm thick PVA film is placed on top of the IDC. The dielectric property of the PVA film is calculated by using the Cole–Cole equation. The coefficients of the Cole–Cole equation at the measured 8 relative humidity values are calculated by Eq. 4.10. The results are listed in Table. 4.2.

Table 4.2: Calculated coefficients of the Cole–Cole equation at measured relative humidity values.

RH	$\varepsilon_{r\infty}$	ε_{rs}	τ_0/ps	α
14.0 %	1.3926	4.9132	6.2500	0.0046
27.5 %	1.5573	5.3650	6.6300	0.0096
36.8 %	1.7008	5.7005	6.9057	0.0159
48.0 %	1.9326	6.1366	7.2583	0.0294
58.2 %	2.2448	6.5936	7.6332	0.0515
65.8 %	2.5882	7.0754	8.0648	0.0782
79.4 %	3.6592	10.4797	11.5677	0.1650
91.2 %	5.5489	40.0741	41.5095	0.3155

At each RH point, the complex permittivity is calculated, and used as input to determine the material properties of the PVA film in simulation. The simulation results of RCS are shown in Fig. 4.16. When the RH humidity increases, the resonance of the sensor shifts to lower frequencies. Due to the larger losses of the material at high RH, the magnitude and the quality factor of the sensors decrease.

A comparison between the resonant frequency from the measurement and the simulation results are shown in Fig. 4.17. The comparison of the resonant frequencies are made at the same RH. Under the same

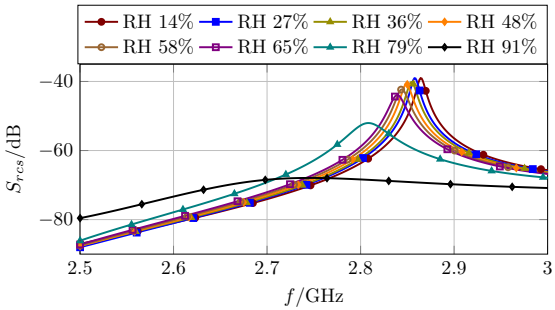

Figure 4.16: Simulation results of RCS of the RH sensor from 14 % to 91 %.

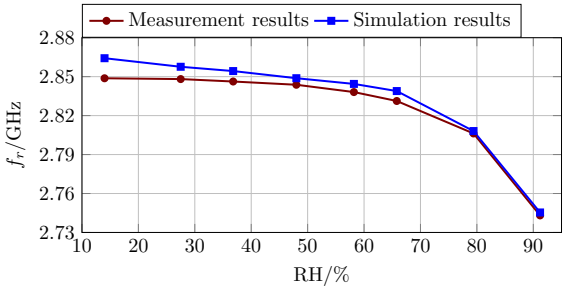

Figure 4.17: Comparison of the resonant frequency from measurement and simulation results.

scale, both curves are close to each other. The resonant frequencies from the simulation results are a bit higher than the measurement results. The distance of the two curves are larger at low RH values. When RH increases, the distances between the two curves are getting smaller. From 79 % to 91 % RH, the two segments are almost overlapping.

To evaluate the difference between the measurement and the simulation results quantitatively, the absolute difference Δf_r and relative difference δ are calculated as:

$$\Delta f_r = f_{\text{simu}} - f_{\text{mea}}, \tag{4.16}$$

$$\delta = \frac{\Delta f_r}{f_{\text{mea}}}. \tag{4.17}$$

f_{simu} is the resonant frequency from simulation results, and f_{mea} is the resonant frequency from measurement results. The results calculated by Eq. 4.16 and Eq. 4.17 are shown in Fig. 4.18.

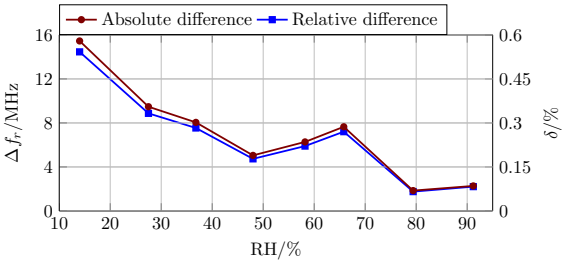

Figure 4.18: Absolute and relative difference of resonant frequency from measurement and simulation results.

The maximum absolute difference between the simulation and measurement result happens at 14 % RH with the value of 15.45 MHz, which is only 0.543 % of the measurement result. When the RH increases, the absolute differences decreases to 1.85 MHz with the relative differences value of 0.0659 % at 79.4 % RH. These little differences prove the high accuracy of the PVA model. Hence, a proper prediction of the RH responses can be performed with this PVA model implemented in a computer simulation tool.

Chapter 5

Relative Humidity Sensing Using Mechanical Loading

When the PVA film absorbs or adsorbs water molecules, it changes not only its permittivity as discussed in chapter 4, but also its mechanical loading, i.e., the mass loading and viscoelasticity. A classical application of this property for RH sensing purpose is to load SAW resonators with PVA films [10,11,54]. The information of relative humidity is transferred to the mechanical loading, and detected by the resonant frequency of a SAW resonator. In this chapter, the working principles of such sensors are discussed in detail. First, the fundamental knowledge of SAW devices are introduced, including the piezoelectric material and the methods to analyze and design the SAW devices, e.g., coupling of modes (COM) method, P-matrix method and simulation tools. Then, SAW resonators loaded with PVA films for RH sensing are investigated. A wet chemical method to pattern the PVA film is discovered, which solves the poor electrical contact and contamination problems of the SAW based RH sensors. The influence of different thickness of the PVA films on the sensor performances are investigated. Applying different patterns and thicknesses of the PVA films, RH sensors design can be facilitated with different performances and measurement convenience.

5.1 Fundamentals of Surface Acoustic Wave (SAW) Devices

SAW devices are built on piezoelectric materials, which are non-centric crystals with linear interaction between mechanical and electrical energy. The piezoelectric materials can be separated into four categories, i.e., single crystal, bulk ceramics, thin film and composite forms, which are introduced in the following [55].

The most demanded piezoelectric material is still quartz, which is a single crystal. With different cuts of the crystal, quartz has different properties, e.g., AT cut quartz has high stability over a wide temperature range, which is well suited for application requiring good frequency stability. Lithium Niobate ($LiNbO_3$) and Lithium Tantalate ($LiTaO_3$) are also very popular due to their high coupling factor between mechanical and electrical energy compared to quartz, but more sensitive to temperature. Different cuts of the material can provide different types of surface acoustic waves or bulk acoustic waves. New materials such as Berlinite and Langasite have also drawn great attention due to their special properties, e.g., for harsh environment applications. Piezoelectric ceramics such as Lead Zirconate Titanate ceramics are also often used, e.g., in fast accelerometer sensors. They have great advantages of fast electromechanical response and compact size.

5.1.1 Direct and Converse Piezoelectric Effect

The most important properties of piezoelectric materials are the direct and converse piezoelectric effect, which explains the transformation between mechanical and electrical energy within the piezoelectric materials. Before introducing the two effects, two physical quantities need to be defined, which are stress and strain.

A force per unit area is called stress. It depends not only on the position and time but also on the orientation of the surface element acted on by the force [55]. An example of various surface forces acting on a material element is shown in Fig. 5.1. A cube is placed in cartesian coordinates with 3 orthogonal axises x_1, x_2 and x_3. T_{ij} is the stress tensor, where i is the stress vector and j is the normal vector of the surface where the stress is applied to. For example, when stress is applied on a surface with the positive direction along x_1, the stress is T_{11}. If the stress is applied on surface b with the positive direction also along x_1, the stress is T_{12}.

A strain is defined as a displacement of material points under a certain system of forces, which is not the absolute movement of the points but the separation and approximation between the particles, i.e., the deformations [56]. Two different types of strains which can occur on piezoelectric materials are shown in Fig. 5.2.

When the elastic material is pressed or pulled, the material has a deformation along the direction of the forces which is defined as normal strain

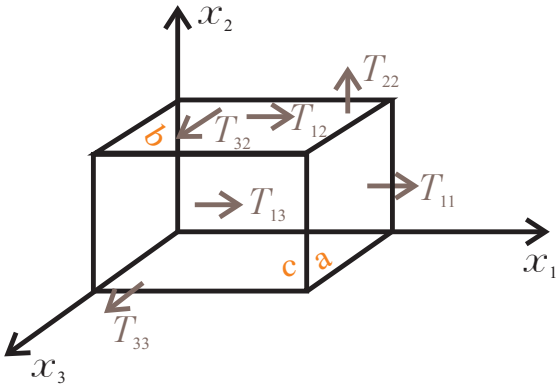

Figure 5.1: Surface forces on a material element.

shown in Fig. 5.2(a). When the angle of the edges changes as shown in Fig. 5.2 (b), the strain is called shear strain.

The relationship between the stress tensor T_λ and the strain tensor S_μ can be approximately expressed by linear functions [55], which are expressed as

$$T_\lambda = c_{\lambda\mu} S_\mu, \tag{5.1}$$

$$S_\lambda = s_{\lambda\mu} T_\mu. \tag{5.2}$$

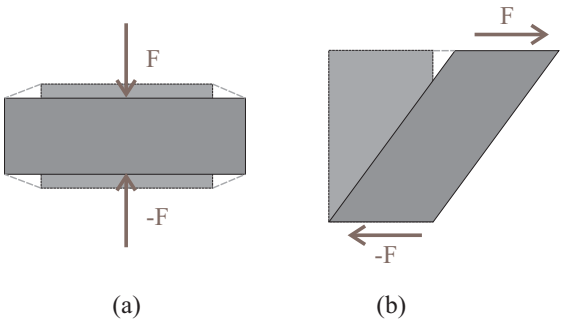

Figure 5.2: Two types of strains: (a) the normal strain and (b) the shear strain.

$c_{\lambda\mu}$ and $s_{\lambda\mu}$ describe the material properties, which are called stiffness and elastic compliance, respectively. They are both 6×6 matrix-equations.

When an extra mechanical stress is applied to the piezoelectric material, an electrical polarization is generated proportional to the strain, which is defined as the direct piezoelectric effect as shown in Fig. 5.3. The piezoelectric material is pressed by a force F in Fig. 5.3 (a), which causes a strain of the material and generates a dielectric displacement P in the material. If an opposite direction force is applied to the material as shown in Fig. 5.3 (b), the electrical polarization has the opposite direction as well.

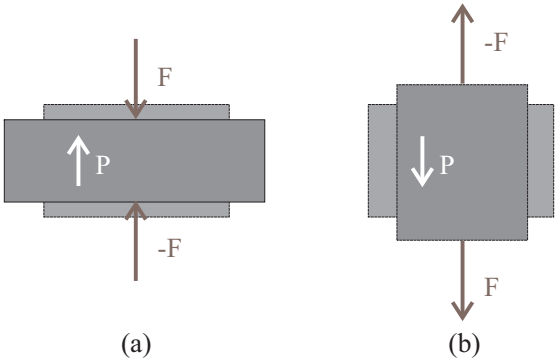

Figure 5.3: The direct piezoelectric effect generated by applying external stress on the material: (a) the piezoelectric material is pressed under forces and (b) the piezoelectric material is pulled under forces.

The direct piezoelectric effect can be described by a linear function between electric displacement D_i and the stress T_μ [55]:

$$D_i = d_{i\mu} T_\mu, \tag{5.3}$$

where $d_{i\mu}$ is called piezoelectric coefficient, which is a 3×6 matrix.

Since the piezoelectric material has the property to convert between mechanical system and electrical system, also a converse piezoelectric effect exists. When an external electrical field is applied to the piezoelectric material, a strain appears to the material as shown in Fig. 5.4. The piezoelectric material is deformed under the electrical field as shown in

Fig. 5.4 (a), while the material is strained to the opposite formation if the external electrical field changes its direction as in Fig. 5.4 (b). Both effects are the fundamental properties of the piezoelectric material, and the terms of "direct" and "converse" are named due to chronological reasons.

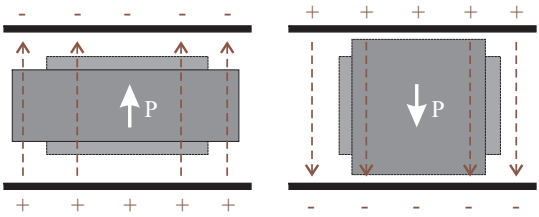

Figure 5.4: The converse piezoelectric effect generated by applying external electrical field to the material: (a) the piezoelectric material is pressed under an electric field and (b) the piezoelectric material is pulled under an electric field.

The converse piezoelectric effect has a mathematical form of [55]

$$T_\mu = h_{i\mu} D_i, \tag{5.4}$$

where $h_{i\mu}$ is a 3×6 matrix, and called piezoelectric modulus.

Considering Eq. 5.2 and Eq. 5.4, the strain can be expressed as a linear function of the electric displacement. If electromagnetic energy with alternating electric displacement is coupled into the piezoelectric material, the strain is alternating too, and hence, a mechanical wave is formed. In an ideally infinite unbounded material, the longitudinal and transverse mechanical wave can propagate. If the particle motion in the material is parallel to the wave propagation direction, the vibration is defined as longitudinal wave, while if the particle motion in the material is perpendicular to the direction of wave propagation, the vibration is called transverse wave. In a material with one bounded interface, a surface acoustic wave can propagate. If both longitudinal and transverse waves are excited and confined at the surface of the material in a depth of the order of a wavelength, the combination of the two waves is called Rayleigh wave [56].

5.1.2 Analysis Methods for SAW Devices

There are mainly two types of methods to analyze and design SAW devices, which are phenomenological methods and numerical methods. The phenomenological methods include the coupling of modes model, P-matrix model, and equivalent circuit models. The numerical methods analyze the elastic wave in the electrodes and the piezoelectric material, and calculate the properties of SAW devices from the material property and geometry. Typical numerical methods use finite element method (FEM), e.g., COMSOL simulation software, and Green's function techniques. The numerical methods are generally more accurate than phenomenological methods, but require large computation effort and time. In the following, the coupling of modes model, one of the phenomenological methods, and finite element method in COMSOL simulation software as numerical method are discussed, respectively. Both methods are nowadays commonly used for the SAW devices design and analysis.

Coupling of Modes

The coupling of modes theory originates from the theory of wave propagation in periodic media. When a wave enters a periodically perturbed region, e.g., the grating on the piezoelectric material surface, a strong reflection happens when the period of the perturbation is equal or close to half of the wavelength. This is called Bragg reflection. The reflected waves are in phase with the incident wave, which add constructively. If the perturbed media is infinite, the wave propagation is formulated mathematically as a Mathieu equation or loaded wave equation [57]:

$$\left(\frac{d^2}{dx^2} + k_0^2\right)\varphi(x) = -\zeta(x)k_0^2\varphi(x), \tag{5.5}$$

where $k_0 = \frac{\omega}{v_0}$ is propagation constant, v_0 is the SAW wave velocity in an unloaded substrate, $\omega = 2\pi f$ is the angular frequency, the field $\varphi(x)$ can be stress, displacement or electric potential, and $\zeta(x)$ stands for the p-periodic load density, which is used to describe the electric or mechanical loading due to the effects of metal electrodes or grooves on the piezoelectric material surface.

The solution of the field $\varphi(x)$ is assumed to be [57]

$$\varphi(x) = \sum_{n=-\infty}^{+\infty} \varphi_n e^{-j(\beta+2\pi n/p)x}, \tag{5.6}$$

which shows an infinite sets of harmonics, coupling to each other. Equation 5.6 can be interpreted as a main or incident wave accompanied by an infinite number of scattered waves, where β is the wavenumber of the fundamental harmonic. The wavenumbers of the infinite higher harmonics are $n\frac{2\pi}{p}$ with respect to the fundamental mode. Only a few harmonics have strong coupling, while all others are negligible because of weak coupling. This is called the coupled-mode approach or coupling of modes.

Due to the assumption of weak coupling, only two waves have large amplitudes and dominate the fields in Eq. 5.6. One is the fundamental mode with the propagation constant β, and the other one is the wave which has the same amplitude but travels in a different direction with the propagation constant of $-\beta$. Since the strong coupling happens under the Bragg condition, the propagation constant of the fundamental mode is close to half structure wavenumber π/p which is expressed as [57]

$$\beta = \frac{\pi}{p} + q, \quad q << \frac{\pi}{p}, \tag{5.7}$$

where p is the perturbation periodicity, e.g., gratings on the materials. The structure wavenumber is constant once the period of the perturbation is fixed. However, the small derivation q is dispersive over frequency. If only the two strong coupling modes are considered and the weak coupling modes are ignored, the Fourier series expansion of the field $\varphi(x)$ in Eq. 5.6 is simplified as

$$\varphi(x) = \varphi_0 e^{-jqx} e^{-j\pi\frac{x}{p}} + \varphi_{-1} e^{-jqx} e^{j\pi\frac{x}{p}}. \tag{5.8}$$

$e^{j\pi\frac{x}{p}}$ in Eq. 5.8 introduces strong spatial variation to the two waves, while e^{-jqx} varies relatively slowly the phase of the waves at different positions. Therefore, the field $\varphi(x)$ can be separated to fast spacial phase part and slow spacial phase part as

$$\varphi(x) = A(x)e^{-j\pi\frac{x}{p}} + B(x)e^{j\pi\frac{x}{p}}, \tag{5.9}$$

where the new variables $A(x)$ and $B(x)$ stand for slowly varying waves traveling in opposite directions. If a linear relationship between the amplitudes of the waves, voltage and current is assumed, the coupling of modes equation has the differential form of [57]

$$\begin{cases} \frac{dA(x)}{dx} &= -j\delta A(x) + j\kappa B(x) + j\alpha V, \\ \frac{dB(x)}{dx} &= -j\kappa^* A(x) + j\delta B(x) - j\alpha^* V, \\ \frac{dI(x)}{dx} &= -2j\alpha^* A(x) - 2j\alpha B(x) + j\omega C V. \end{cases} \tag{5.10}$$

The coupling factor κ stands for the reflectivity due to the periodic loading of the gratings. α is the transduction coefficient, which measures the excitation of waves due to the piezoelectric coupling. δ is defined as a detuning factor, which can be approximately expressed as $\delta = \pi(f - f_0)/(pf_0)$. f_0 is a center frequency which is the loaded acoustic wave velocity divided by two times of the perturbation periodicity. C is the capacitance, which measures the electrostatic storage of energy in the structure. The slowly-varying wavenumber q in Eq. 5.7, which is also known as COM dispersion relation can be calculated by the coupling factor and the detuning factor as [57]

$$q = \pm\sqrt{\delta^2 - |\kappa|^2}, \quad \mathrm{Im}(q) \leq 0. \tag{5.11}$$

Mathematically, both signs of the square root in Eq. 5.11 have equal results. However, physically the imaginary part of q, which is noted as q'' should always be non-positive, since amplitude of the waves cannot increase in passive devices. The dispersion relation is shown in Fig. 5.5 under the condition of finite reflectivity, lossless material and no scattering to the bulk acoustic wave.

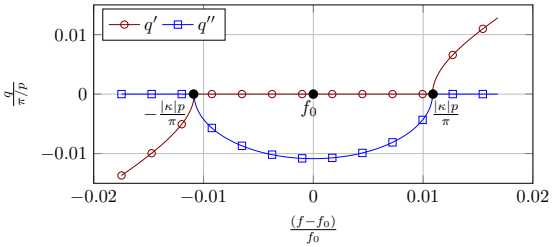

Figure 5.5: Dispersion relation of the slowly varying wavenumber $q = q_{\prime} + jq_{\prime\prime}$ with the real part $q_{\prime}$ and the imaginary part of $q_{\prime\prime}$.

Fig. 5.5 shows the most important results in COM model. When $(f - f_0)/f_0$ is within the range of $-|\kappa|\, p/\pi$ to $|\kappa|\, p/\pi$, q is pure imaginary. The frequency range is called stopband. Within this stop band, the wavelength is close to the perturbation periodicity of $2p$, which satisfies the Bragg reflection condition. Due to the Bragg reflections, the amplitudes of modes attenuate in the propagation direction, which is used for SAW resonators design.

P-matrix

It is convenient and useful to analyze and design the SAW devices from a network point of view. The structures such as IDTs and reflectors can be described by a P-matrix, which is considered as a discrete version of the continuous COM method [58, 59].

Fig. 5.6 represents a part of an interdigital transducer located between $x = x_1$ and $x = x_2$. The incident waves $a(x_1)$ and $a(x_2)$ approach from the side boundaries of the transducer, which are marked with dashed lines. Then, the incident waves are reflected by the transducer, where the reflected waves are $b(x_1)$ and $b(x_2)$. Meanwhile due to the piezoelectric effect, the current I is generated by the transducer.

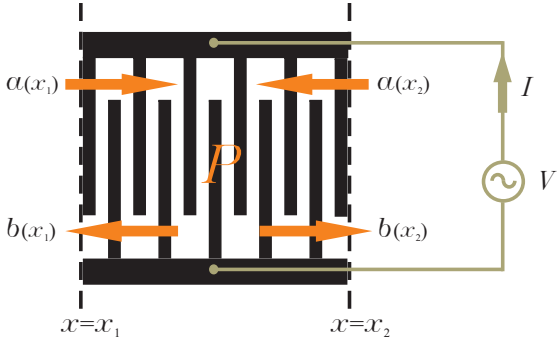

Figure 5.6: Interdigital Transducer of piezoelectric devices with two acoustic ports located at $x = x_1$ and $x = x_2$. The P-matrix is used to describe the structure, which relates the incident waves and the voltage to the reflected wave and the current.

From Eq. 5.10, a linear relationship between $A(x)$ and $B(x)$, V and I is observed, and the coefficients are all COM parameters. If we consider $a(x_1)$, $a(x_2)$ and V as input, and $b(x_1)$, $b(x_2)$ and I as output parameters, the structure in Fig. 5.6 can be defined through the matrix equation as [59]

$$\begin{bmatrix} b(x_1) \\ b(x_2) \\ I \end{bmatrix} = \begin{bmatrix} P_{11}(f) & P_{12}(f) & P_{13}(f) \\ P_{21}(f) & P_{22}(f) & P_{23}(f) \\ P_{31}(f) & P_{32}(f) & P_{33}(f) \end{bmatrix} \begin{bmatrix} a(x_1) \\ a(x_2) \\ V \end{bmatrix}. \tag{5.12}$$

The first part on the right hand side is called P-matrix. They are frequency dependent parameters, which describe both, the acoustic and

electric property of the transducer. $P_{11}(f)$ and $P_{22}(f)$ are the reflection coefficients, which describe the reflection of the incident acoustic waves due to the presence of the electrodes. $P_{12}(f)$ and $P_{21}(f)$ are the transmission coefficients, which evaluate the transmission of the the acoustic waves under the influence of the structure. These four components describe the scattering parameters of the acoustic waves. The left five are the acoustoelectric parameters, which connect the electric current and voltage to the acoustic waves. $P_{13}(f)$ and $P_{23}(f)$ are the excitation efficiency of the transducer, which describe the transferring efficiency between electric energy and mechanical energy. $P_{31}(f)$ and $P_{32}(f)$ evaluate the current generated by the transducer due to the incident waves. $P_{33}(f)$ is the admittance of the transducer.

The P-matrix can be expressed by the COM parameters. For an interdigital transducer or an electrically shorted grating, the scattering parameters in the P-matrix are [60]

$$P_{11}(f) = \frac{j\kappa^* \sin(qL)}{q\cos(qL) + j\delta\sin(qL)}, \tag{5.13}$$

$$P_{12}(f) = P_{21}(f) = \frac{(-1)^N q}{q\cos(qL) + j\delta\sin(qL)}, \tag{5.14}$$

$$P_{22}(f) = \frac{j\kappa \sin(qL)}{q\cos(qL) + j\delta\sin(qL)}, \tag{5.15}$$

where L is the length of the IDT or electrically shorted gratings. The frequency dependent magnitude and phase of reflection coefficient $P_{11}(f)$ are shown in Fig. 5.7

The magnitude of P_{11} is close to one when κL is larger than 6.82, which is much larger compared to 1. When the length of the transducer or gratings decreases, the magnitude of the reflection within the stopband becomes smaller as the curve of $\kappa L = 0.682$ shows, and the edges of the stopband get less sharp. The width of the sidelobes become broader, and the distance between the sidelobes are larger with smaller κL values.

The frequency between f_{left} and f_{right} in Fig. 5.7 is the stopband, if $\kappa L >> 1$ such as the curve of $\kappa L = 682$. f_{left} matches the point of $-|\kappa|\, p/\pi$, and f_{right} matches the point of $|\kappa|\, p/\pi$ in Fig. 5.5. From Eq. 5.13 the phase of the reflection coefficient P_{11} can be calculated. For $f = f_0$, the phase of P_{11} is $-\frac{\pi}{2}$. For $f = f_{\text{left}}$, the phase of P_{11} is 0. For $f = f_{\text{right}}$, the phase of P_{11} is $-\pi$.

The admittance $P_{33}(f)$ consists of two elements [60]:

$$P_{33}(f) = P_{33}^{sc}(f) + P_{33}^{E}(f). \tag{5.16}$$

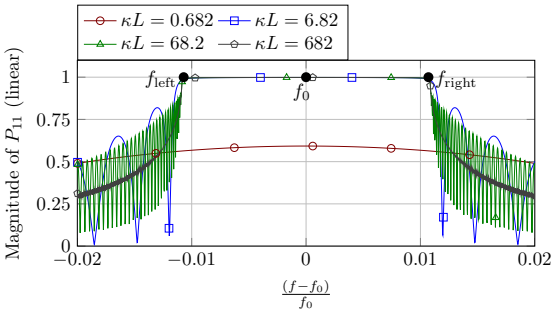

(a) Magnitude of the frequency dependent reflection coefficient $|P_{11}|$.

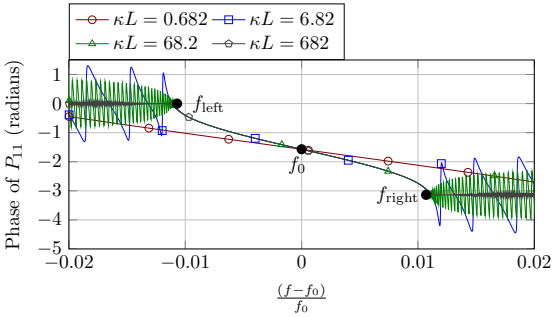

(b) Phase of the frequency dependent reflection coefficient $\varphi(P_{11})$.

Figure 5.7: Magnitude and phase of the reflection coefficient P_{11} with various values of κL as a function of $\frac{f-f_0}{f_0}$.

$P_{33}^{sc}(f)$ stands for the current due to the eigenmodes generated from the voltage and reflected from the edge of the transducer. $P_{33}^{E}(f)$ describes the currents generated from excited field. In a long transducer, the latter component in Eq. 5.16 dominates the admittance result, which is expressed as [60]

$$P_{33}^{E}(f) = -L4j\frac{\delta\left|\alpha\right|^2 + \mathrm{Re}(\kappa^*\alpha^2)}{\delta^2 - \left|\kappa\right|^2} + j\omega CL. \tag{5.17}$$

A plot of the admittance of a long transducer is shown in Fig. 5.8. The resonance frequency f_r measures at the maximum of the conductance of Y_r, which is at one edge of the stopband in Fig. 5.5 due to the constructively interfering eigenmodes. At the other edge of the stopband, the

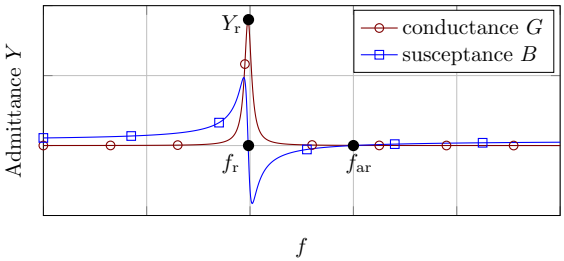

Figure 5.8: Admittance of an infinite long transducer.

resonance cannot be noticed due to the destructive interference of the eigenmodes. An anti-resonance frequency f_{ar} measures the frequency at which the susceptance is zero.

The biggest advantage of introducing the P-matrix is that the devices such as resonators and delay lines can be easily modeled by cascading the P-matrix of the structures, e.g., transducers and reflectors, which are used to compose the devices. Each structure can be described separately by the P-matrix, and connected together by sharing common acoustic ports or electrically connection. One section for cascading an IDT is shown in Fig. 5.9.

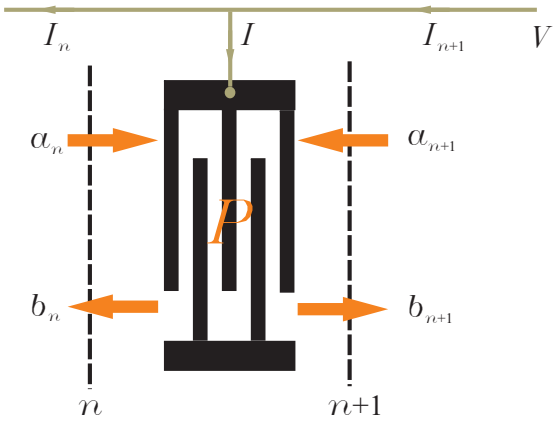

Figure 5.9: One cascading section with two acoustic wave ports and one electrical port.

The IDT has two acoustic wave ports, namely port n and port $n+1$. The acoustic waves a and b travel though the two ports. The current on the IDT is I, which is the difference between I_n and I_{n+1} on the two sides of the IDT. The voltage V is considered the same for all of the cascading sections. The P-matrix in Eq. 5.12 can be rearranged as a transmission matrix, relating quantities on the right to those on the left [61]

$$\begin{bmatrix} b_{n+1} \\ a_{n+1} \\ V \\ I_{n+1} \end{bmatrix} = \begin{bmatrix} t_{11}(f) & t_{12}(f) & t_{13}(f) & 0 \\ t_{21}(f) & t_{22}(f) & t_{23}(f) & 0 \\ 0 & 0 & 1 & 0 \\ t_{31}(f) & t_{32}(f) & t_{33}(f) & 1 \end{bmatrix} \begin{bmatrix} a_n \\ b_n \\ V \\ I_n \end{bmatrix}, \tag{5.18}$$

where t_{ii} is a function of P-matrix, which can be found in [61].

An application of the cascading method is to calculate the admittance of a one port SAW resonator. A typical one port resonator is composed of a transducer and two identical reflectors located symmetrically on both sides of the transducer. Normally a gap is located between the transducer and the reflector. The P-matrix of the gap is derived as [62]

$$P_{gap} = \begin{bmatrix} 0 & (1-\gamma_{gap})e^{-j\omega d/v_{gap}} & 0 \\ (1-\gamma_{gap})e^{-j\omega d/v_{gap}} & 0 & 0 \\ 0 & 0 & 0 \end{bmatrix}. \tag{5.19}$$

d is the width of the gap, γ_{gap} is the material loss of the unloaded gap surface and v_{gap} is the phase velocity of the SAW on an unloaded gap surface.

The admittance of the reflector-gap-transducer-gap-reflector structure is calculated as [57]

$$Y = P_{33}^{\mathrm{IDT}} - \frac{4R(P_{13}^{\mathrm{IDT}})^2}{1 - R(P_{11}^{\mathrm{IDT}} + P_{12}^{\mathrm{IDT}})}, \tag{5.20}$$

where P_{ii}^{IDT} is the component of the P-matrix of the interdigital transducer and R is the reflection coefficient of the reflectors and the gaps, which is calculated as

$$R = (1-\gamma_{gap})^2 e^{-2j\omega d/v_{gap}} P_{11}^{g}. \tag{5.21}$$

P_{11}^{g} stands for the reflection coefficient of the reflector. Similar results for delay lines or two ports resonators can also be obtained by cascading the transmission matrix of each structure.

COMSOL Multiphysics Simulation

Nowadays computer aided design softwares have been widely used for SAW devices. One of the most popular one is COMSOL Multiphysics, which includes a piezoelectric interface and can perform various types of studies such as eigenfrequency, frequency response and time dependent studies. COMSOL uses adaptive meshing together with finite element method to solve the numerical problems.

YZ cut $LiNbO_3$ used as the material for the SAW devices. An infinite IDT surface acoustic wave resonator model is build into the piezoelectric interface with the proper definition of the $LiNbO_3$ material properties such as stiffness and dielectric constant, which is shown in Fig. 5.10.

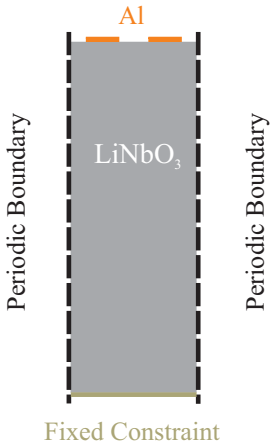

Figure 5.10: An infinite IDT surface acoustic wave resonator model in COMSOL piezoelectric interface.

The electrodes are made of aluminum with a height of 200 nm and width of 1.961 µm. The bottom boundary in the model is set as the fixed constraint. Therefore, if only one side of the piezoelectric material is unbounded, a surface acoustic wave can be formed. To realize the infinite IDT in this model, both left and right boundaries are defined as periodic boundaries, which have periodic SAW displacement and electric potential. First the eigenfrequency is studied, which is expected around 433 MHz. Two eigenmodes are found and the displacement at both eigenfrequencies are shown in Fig. 5.11.

The inner reflection of the electrodes are considered in the simulation, thus, the infinite IDT structure forms a one port resonator. Fig. 5.11a

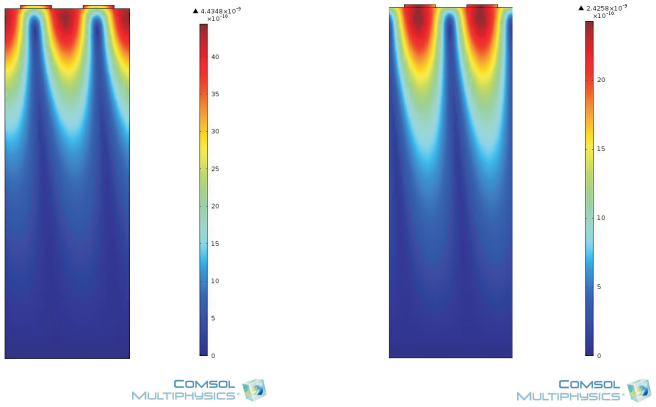

(a) Displacement of the infinite IDT structure with eigenfrequency at 432.8247 MHz

(b) Displacement of the infinite IDT structure with eigenfrequency at 442.3262 MHz

Figure 5.11: Two eigenmodes of the infinite IDT structure

shows surface acoustic wave displacement of the first eigenmode at $f_{\text{low}} = 432.8247\,\text{MHz}$. The maximum of the standing wave appears at the gap between the electrodes. To fulfill the phase requirement for resonance, the reflection coefficient is -1 at both boundaries, which means f_{low} locates at the lower edge of the stopband shown in Fig. 5.5. This mode is able to be excited by applying a differential electric potential on the two electrodes. Fig. 5.11b shows surface acoustic wave displacement of the first eigenmode at $f_{\text{up}} = 442.3262\,\text{MHz}$ with the maximum standing surface acoustic wave at the position of the electrodes. The reflection coefficient at this mode is $+1$, which means f_{up} locates at the upper edge in the stopband. To excite such mode, both electrodes need to have same electric potential. This excitation cannot be realized, since the one port resonator is usually measured by the device with a differential potential.

The frequency response of the infinite IDT can also be obtained by employing a frequency solver in COMSOL with a differential excitation applied on the two electrodes. The IDT is first meshed with unstructured quadrilateral elements. The FEM method is applied to calculated the frequency response. The simulated admittance is shown in Fig. 5.12. The resonant frequency f_r is 432.825 MHz, at which the conductance has the maximum value. The result matches the resonant frequency cal-

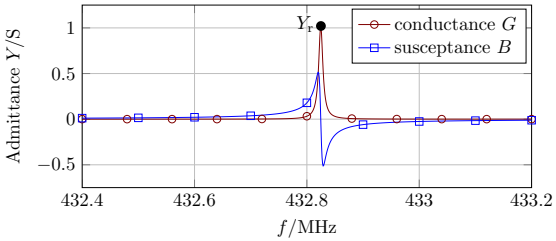

Figure 5.12: Simulation result of the admittance in the frequency domain.

culated from the eigenmode study with the differential excitation case. The quality factor is 48092.

The COM parameters can be obtained from the eigenmode and frequency simulation results. The lower and upper frequency of the stopband in Fig. 5.5 can be calculated as the zeros of Eq. 5.11 by neglecting the attenuation parameter, which is [57]

$$\begin{cases} f_{\text{low}} = f_0 \left(1 - \frac{|\kappa| p}{\pi}\right), \\ f_{\text{up}} = f_0 \left(1 + \frac{|\kappa| p}{\pi}\right). \end{cases} \tag{5.22}$$

The frequencies f_{low} and f_{up} are obtained from the eigenmode simulation results. From Eq. 5.22, the center frequency f_0 can first be determined as

$$f_0 = \frac{1}{2} \left(f_{\text{low}} + f_{\text{up}}\right). \tag{5.23}$$

Then the velocity of the surface acoustic wave can be calculated as $v = \lambda f_0$, with $\lambda = 2p$. Re-arranging Eq. 5.22, the normalized reflectivity $\kappa_p = \kappa\lambda_0$ is expressed as either

$$\kappa_p = -\frac{\left(f_0 - f_{\text{low}}\right)\pi}{f_0}, \tag{5.24}$$

or

$$\kappa_p = -\frac{\left(f_{\text{up}} - f_0\right)\pi}{f_0}. \tag{5.25}$$

To determine the attenuation factor γ_p, the bandwidth of the half maximum admittance Δf needs to be calculated from the frequency simulation result in Fig. 5.12, then the normalized attenuation factor is expressed as [63]

$$\gamma_p = \frac{\Delta f \pi}{f_0}. \tag{5.26}$$

The transduction coefficient $\alpha_p = \alpha\lambda_0$ can be determined by the maximum value of the admittance Y_r shown in Fig. 5.12, which has the form of [63]

$$\alpha_p = \sqrt{\frac{Y_r \gamma_p}{4}}. \tag{5.27}$$

The transduction coefficient can be normalized by the aperture W, which is expressed as $\alpha_n = \alpha_p / \sqrt{\frac{W}{\lambda_0}}$. With the help of a defined quality factor $Q = f_r/\Delta f$, the capacitance is calculated as [63]

$$C_p = \frac{Y_r}{2\pi f_{ar}} \frac{2Q\left(f_{ar}/f_r - 1\right)}{4Q^2\left(f_{ar}/f_r - 1\right)^2 + 1}, \tag{5.28}$$

where the anti-resonant frequency $f_{ar} = 440.869\,\mathrm{MHz}$, at which the susceptance of the infinite IDT is zero in the simulation result. The capacitance can be normalized by the aperture W as well, which is calculated as $\alpha_n = \alpha_p / \sqrt{\frac{W}{\lambda_0}}$.

All COM parameters are determined from Eq. 5.23 to Eq. 5.28. The results are shown in Table. 5.1. The results in Table 5.1 are consistent with the COM parameters extracted for YZ $LiNbO_3$ in [63, 64]. Substituting the COM parameters into Eq. 5.17, the admittance of the infinite IDT can be calculated.

Table 5.1: Normalized COM parameters from the COMSOL simulation results with an aperture of 392.2 µm and a wavelength of 7.844 µm.

Parameter	Values	Dimension (SI)
v	3432.3	m/s
κ_p	-0.0682	
α_p	0.0041	$\Omega^{-1/2}$
α_n	$5.7428 \cdot 10^{-4}$	$\Omega^{-1/2}$
γ_p	$6.4616 \cdot 10^{-5}$	Np/λ_0
C_p	$2.0615 \cdot 10^{-13}$	F
C_n	$5.2562 \cdot 10^{-10}$	F/m

A comparison of the admittance obtained from the COM model and the COMSOL simulation results is shown in Fig. 5.13. It is observed from Fig. 5.13a that the resonant frequencies of the infinite IDT calculated

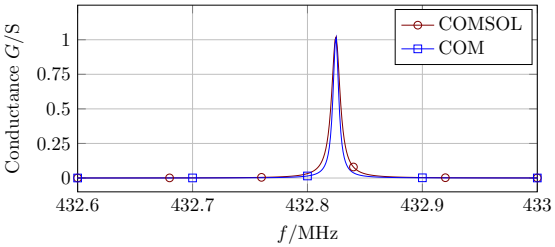

(a) Conductance of the infinite IDT calculated from the COM model and the COMSOL simulation result.

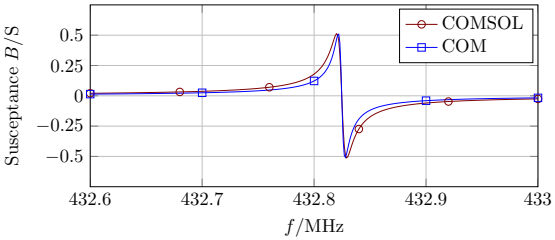

(b) Susceptance of the infinite IDT calculated from the COM model and the COMSOL simulation result.

Figure 5.13: A comparison of the admittance obtained from the COM model and simulation results from COMSOL.

from both methods are the same with the equal magnitude of conductance. However, the conductance determined from the COM model is narrower than the one obtained from COMSOL. The quality factor calculated from COM model has the value of 72138, which is 1.5 times higher than the quality factor obtained from COMSOL. Fig. 5.13b shows the susceptance of the infinite IDT. Around the resonant frequency range, both results coincide as well.

The advantage of the COM model is the short computational time, since that the SAW structure can be expressed with analytical equations. However, preliminary measurements are needed to extract the COM parameters. The numerical simulation doesn't need preliminary measurements, since the response of the SAW devices can be determined only based on the material physical properties. But the computational time of numerical simulation is at least 10 times longer than the COM

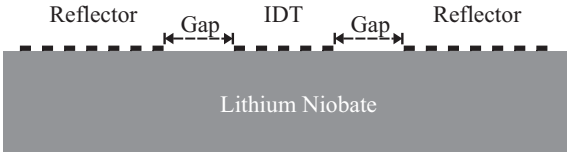

Figure 5.14: One port surface acoustic wave resonator which contains an IDT, two reflectors and gaps.

model. Nevertheless, both methods are very helpful to study and design SAW devices,

5.2 One Port SAW Resonator

The surface acoustic wave devices such as resonators and delay lines play a very important role in sensors. To detect the physical parameters from frequency responses with high quality factor, SAW resonators are usually employed for sensing applications. From the methods introduced in 5.1, the numerical simulation tool COMSOL is used to design a one port SAW resonator in an industrial scientific and medical (ISM) radio band.

The one port SAW resonator contains three parts, which are IDT, reflectors and the gaps between the IDT and reflectors as shown in Fig. 5.14. The structure is built on a YZ cut $LiNbO_3$ piezoelectric substrate with a thickness of 500 µm. The electrodes are made of aluminum with a thickness of 125 nm. The IDT contains 21 fingers with a width of 1.96 µm.

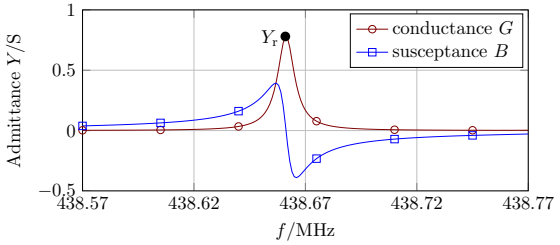

Figure 5.15: Admittance calculated from simulation result of one port surface acoustic wave resonator in COMSOL.

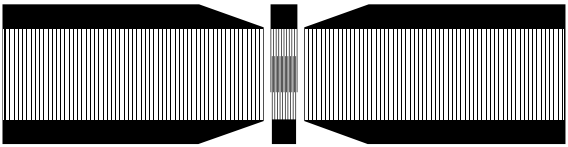

(a) Mask of the one port SAW resonator with two contact pads for on-wafer measurements and shorted electrodes in the reflectors.

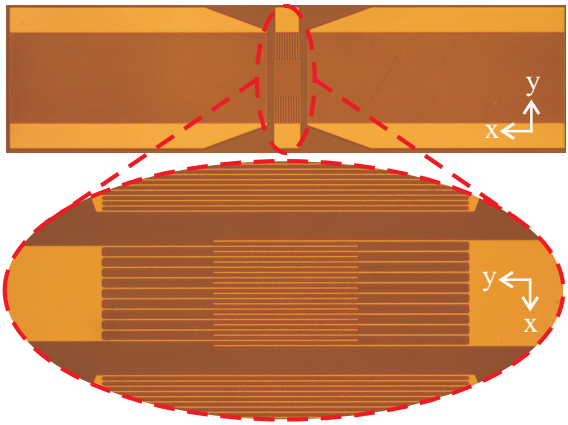

(b) Fabricated one prot SAW resonator with the magnified IDT .

Figure 5.16: Mask and fabricated one port SAW resonator.

The reflectors consist of 200 electrodes with a width of 1.96 µm as well. The distance between the fingers in the IDT and the electrodes in the reflectors are the same,having a value of 1.96 µm. The gap between the electrode edge of the IDT and the reflector is 20.59 µm. The model is simulated with the COMSOL frequency solver, assuming two perfect matched layers added at both ends of the substrate. The calculated admittance is shown in Fig. 5.15. The structure resonates at 438.66 MHz which is near the ISM band. The quality factor of the resonator is 48740, which is calculated as the resonant frequency divided by the bandwidth measured at the half of the maximum admittance.

The SAW resonator structure is fabricated by a standard photo lithography and wet etching process shown in Fig. 5.16. Fig. 5.16a presents

the mask of the structure. The IDT has two contact pads with the size of 78 µm by 69 µm, which is used for the on-wafer measurements by a SG probe. The IDT has an aperture of 109.8 µm. The electrodes in the reflectors are shorted in the design.

Fig. 5.16b shows the fabricated one port SAW resonator. The average thickness of the structure is 125 µm, measured by a Dektak Profilometer. The IDT of the resonator is magnified in the figure. The width of the electrodes is smaller than the gap between the electrodes, which is due the inevitable under etching during the fabrication process. The imperfectly etching process also results in rough edges of the electrodes, which increases the loss of the resonator.

The resonator shown in Fig. 5.16b is measured by a VNA, using a SG probe with a pitch of 350 µm. The measurement system is calibrated to the end of the probe, which has a impedance of 50 Ω. The result is shown in Fig. 5.17.

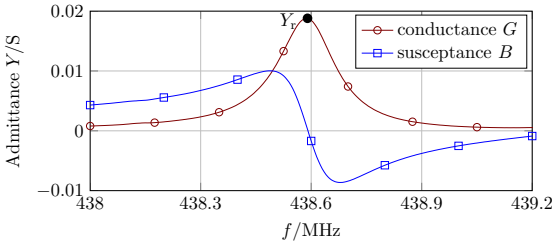

Figure 5.17: Admittance calculated from the measurement result of one port surface acoustic wave resonator.

The resonant frequency of the resonator is measured at 438.59 MHz. The difference of the resonant frequency between measurement and simulation results is 0.07 MHz, which is 0.016 % of the measured resonant frequency. The quality factor calculated from Fig. 5.17 is 2308.4, which is 4.74 % of the one from the simulation results. This is due to the losses introduced during the fabrication process.

The SAW resonator is coated with sensitive polymer to realize the functional layer for sensing humidity. A problem of the SAW based sensors is that the aluminum electrodes of the sensor are often attacked by chemically reactive gases, which results in forming an acid or a base with the humidity of the ambient air. The problem is aggravated that the measured gas is further accumulated at the surface of the devices due to

increasing of sorption by the sensing film. This has a consequence of serious performance degradation of the sensing function and even destruction of the SAW device after a limited number of measurement cycles. One of the best solutions is to use anti-corrosive metal as electrodes such as gold. The robustness against corrosion of gold electrodes has been tested to be effective, and the quality factor of gold SAW resonators are comparable to aluminum structures [65–67].

A comparison of the physical properties between aluminum and gold is shown in Table. 5.2. It can be seen that gold is much heavier than aluminum, with a density of more than 7 times larger than that of aluminum. The Young's modulus of gold is 12.8 % larger than aluminum. Poisson ratio of gold is 14.28 % larger than that of aluminum.

Table 5.2: Comparison of the physical properties between aluminum and gold.

Material	Density	Young's modulus	Poisson ratio
Aluminum	2.7 g/cm^3	70 GPa	0.35
Gold	19.3 g/cm^3	79 GPa	0.40

A one port SAW resonator made of gold electrodes is fabricated using the same mask shown in Fig. 5.16a. The average thickness of the gold electrodes is 90 nm. The structure is measured with the same setup as the resonator with aluminum electrodes. The admittance of the resonator is shown in Fig. 5.18. The structure resonates at 436.02 MHz, and the quality factor is 3007. The resonant frequency deviates 2.57 MHz, which is near the ISM band. The quality factor increases by 699. Hence, it is better for the sensing application by detecting the frequency shift. Therefore, gold electrodes are used for the following design of SAW based sensors.

5.3 Sensing Principle of SAW Devices

SAW devices are often used for sensing applications. Any change in physical properties of the surface on a SAW device or a film loaded on the surface can directly affect the wave propagation parameters, i.e. the phase velocity and the attenuation factors, which lead to the change of electric response [68, 69]. There are two types of mechanisms which contribute to the SAW based sensors, namely the electric loading and the mechanical loading. The electric loading is the acoustoelectric effect

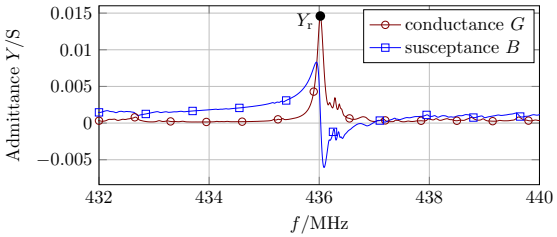

Figure 5.18: Admittance calculated from the measurement results of one port surface acoustic wave resonator with gold electrodes.

which describes the coupling between the electromagnetic wave (EMW) and the SAW on the surface of the devices. The mechanical loading considers the mass loading and the viscoelastic effect, which are caused by the sensitive film loaded on top of the SAW devices. All the three effects change the SAW phase velocity according to equation [68]:

$$\frac{\Delta v}{v} = -c_m f_0 \Delta(m/A) + 4c_e \frac{f_0}{v^2} \Delta(hG') - \frac{K^2}{2} \Delta \left[\frac{\sigma^2}{\sigma^2 + v^2 C^2} \right]. \quad (5.29)$$

The first part on the right hand side in Eq. 5.29 calculates the mass loading effect. c_m is the coefficient of the mass sensitivity, and $\Delta(m/A)$ is the change in mass per unit area. f_0 is the center frequency. The second part describes the viscoelastic effect which contributes to the change of velocity. c_e is the coefficient of the elasticity, h stands for the film thickness, and G' is the real part of the shear modulus. The third part on the r.h.s. is the acoustoelectric effect. K^2 stands for the electromechanical coupling coefficient, σ is the sheet conductivity of the film, and C is the capacitance per unit length. A comprehensive discussion of these three effects on the attenuation factors can be found in [69].

In this work, a humidity sensitive film PVA is loaded on top of the SAW devices. Both the electric loading and the mechanical loading have influence on the sensor's response. The effect of electric loading is studied by simulations. An infinite IDT with a sensitive film on top is built in COMSOL, which is shown in Fig. 5.19.

The sensitive film is considered as a dielectric layer with a relative permittivity $\varepsilon_{\text{sens}}$ and a thickness h_{sens}. The edges of the sensitive film are set to be periodic. The electrodes in the model are made of gold with a thickness of 80 nm, which is the same as used in the humidity sensors.

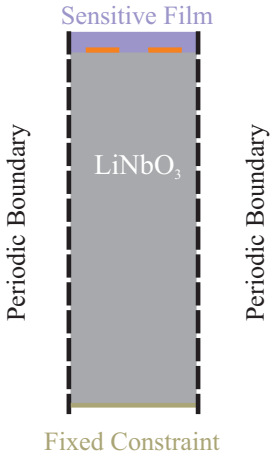

Figure 5.19: Infinite IDT model with sensitive film loaded on top used in COMSOL.

First, the influence of the thickness of the sensitive film on the electric loading effect of the infinite IDT is studied. $\varepsilon_{\text{sens}}$ is chosen arbitrarily with a value of 8. The thickness changes from 300 nm to 900 nm with a step of 100 nm. Fig. 5.20 shows the resonant frequency f_r from this simulation.

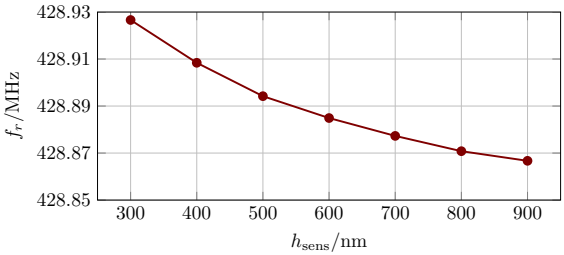

Figure 5.20: The electric loading effect with different PVA film thickness.

The resonant frequency of the infinite IDT decreases with increasing thickness of the PVA film. An average decreasing rate with increasing thickness is about -0.01 kHz/nm. A one port SAW resonator with the structure of reflector-gap-IDT-gap-reflector is used in COMSOL with a

865 nm thick PVA film loaded on top. The relative permittivity of the film at different RHs can be obtained by the comprehensive model introduced in section 4.1.7. The simulation model doesn't consider the mechanical loading of the PVA film. This sensor is characterized from 15 % RH to 60 % RH in the measurement setup described in section 4.1.3, and both, electric loading and mechanical loading contribute to the frequency change in the measurement results. A comparison between the resonant frequency from simulation and measurement results is shown in Fig. 5.21.

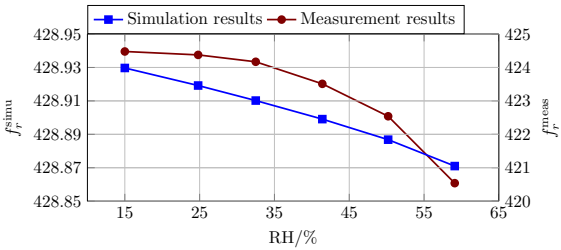

Figure 5.21: Comparison of the resonant frequencies between the simulation and measurement results of a one port SAW resonator covered with a PVA film.

The resonant frequency from simulation changes about 58.7 kHz by changing RH from 15 % to 60 %, while the resonant frequency from the measurement results varies 3939.8 kHz, which is 67 times more than simulation results. The significant difference between the simulation and measurement results are due to the mechanical loading effect of the PVA film. Therefore, for the SAW resonator based humidity sensor with sensitive film loaded on top, the mechanical loading dominates the sensor response.

5.4 Relative Humidity Sensors with Different PVA Film Patterns

As discussed in Chapter 4, PVA film is a very promising material for humidity sensing with good sensitivity, low cost and easiness of fabrication. Another application of PVA film in humidity sensing is to use the property of its mechanical loading which changes with the environment humidity. A major part of utilizing this property is to coat the PVA films

on surface acoustic wave resonators. The velocity of SAW changes with different mechanical loading, and thus changes the resonant frequency of SAW resonator. The planar structure, high electrical quality factor, small size of the SAW resonators covered with PVA film play an important role for detecting the humidity. However, after loading the PVA film, the measurement terminals, i.e., the contact pads of the RH sensors, are covered by the PVA film as well. This creates a poor electrical contact to sensors and contaminates the measurement probes. Meanwhile, the PVA film covered terminals prevents the sensors from being integrated to other components such as antennas in order to realize more functions.

In this section, a wet chemical method of patterning PVA film in micrometer resolution is introduced to solve the stated problems. Two different patterns of PVA films are applied as functional layers to a one port SAW resonator with anti-corrosive gold electrodes for RH sensing. Both patterns have open windows through PVA film on the top of RH sensor terminals, which bring the sensors with clean contact pads for measurement and integration. The frequencyhumidity responses of the two sensors are characterized, and the performances are compared. The sensor with PVA film patterned only on the reflectors of the SAW resonator has larger RH operation range, higher maximum reflection and higher quality factor. The other one with PVA film opened at IDT pads shows higher sensitivity.

5.4.1 PVA Film Pattern

PVA is a hygroscopic polymer which has high molecular weight with a glass transition temperature about 70°C. It has an –OH group bonded to each carbon in the backbone chain [70]. A 10 % PVA solution, provided by Wacker Chemie AG is prepared, and the photolithographic pattern procedure is shown in Fig. 5.22. First the PVA solution is spin-coated on a one port SAW resonator. The structure is baked at 60°C for 20 min in the open air to dry the PVA film. Then a positive photoresist AZ6632 from MicroChemicals GmbH is spin-coated on top of the PVA film with the thickness of 2.61 µm. Afterwards it is prebaked at 60°C for 5 min and exposed under ultraviolet (UV) light for photolithography with the desired pattern shaped mask. The AZ726 metal ion free (MIF) developer, which contains 2.38 % tetramethylammonium hydroxide and surfactant from AZ Electronic Materials GmbH, while the PVA film is etched in the same development bath. At the end, the photoresist is stripped with

acetone and proponone. The fabrication of the RH sensor with patterned PVA film is then ready for RH characterization.

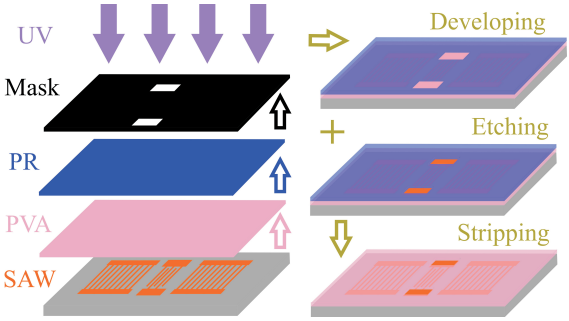

Figure 5.22: Process of patterning PVA film.

5.4.2 Sensor Structures and Measurement Results

With the method of photolithographically patterned PVA films, the sensor design is facilitated to fulfill different application requirements. Two different patterns of PVA films are investigated for RH sensing, which are loaded on gold electrodes one port SAW resonator. The first one is to cover the whole area of the SAW resonator with PVA film except the IDT pads shown in Fig. 5.23. The open area of the contact pad on the sensor is 100 µm by 73 µm and the thickness of the film is around 865 nm.

The frequency–humidity response of the sensor is measured on-wafer with a signal ground probe in a climate chamber, which is introduced before in section 4.1. The scattering parameter S_{11} is measured using a vector network analyzer. The time duration between two RH measurements is 20 min, so that both, the RH in the climate chamber and the electrical response of the sensor are stabilized. In order to eliminate the interrogation signal and the EMW reflection from the IDT, a time gate from 101 ns to 1 ms is implemented on the results. After excitation, the energy is stored in the SAW resonator. The SAW wave is delayed due to a lower phase velocity compared to EMW, and retransmitted to the VNA. After applying the time gate, the signal contains only the SAW energy, and hence, the RH information can be retrieved from resulting peaks after Fourier transform [71]. The results are shown in Fig. 5.24.

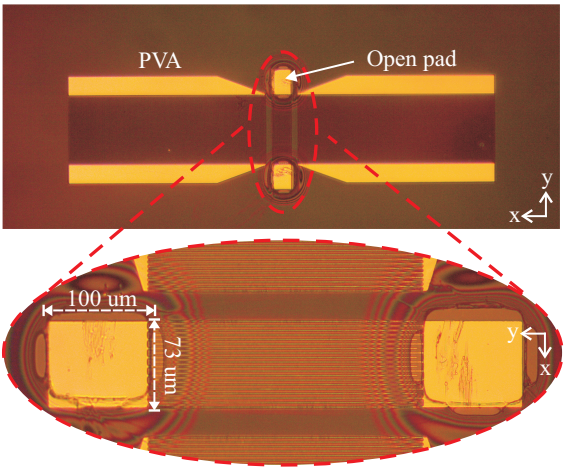

Figure 5.23: RH sensor with PVA film open at IDT pads.

The sensor is characterized at 7 different RHs from 15 % to 69.4 % RH at 20°C. The results of S_{11} after time gated of 6 responses, i.e., 15 %, 32.5 %, 41.4 %, 50.2 %, 59.1 % and 64.9 % RH are shown in Fig. 5.24. When the RH increases, the resonant frequency of the sensor decreases and the resulting peaks became broader. The maximum RH, i.e., the maximum RH which the sensor can detect, is 59.1 % with this PVA thickness and pattern, since there are no detectable peaks within the

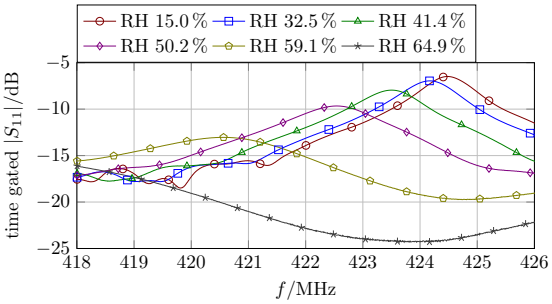

Figure 5.24: Measurement results of RH humidity sensor with PVA film open at IDT pads after time gate.

interested frequency band at higher RHs.

After the measurements, the first pattern of the PVA film on top of the SAW resonator is washed away by AZ726 MIF developer and de-ionized water. The SAW resonator is measured, and the response is the same as that before the deposition of the first PVA film pattern. The second pattern is then realized with the PVA film loaded only on the reflectors of SAW resonator shown in Fig. 5.25. The size of the PVA film is 982 µm by 825 µm with a measured thickness of 910 nm.

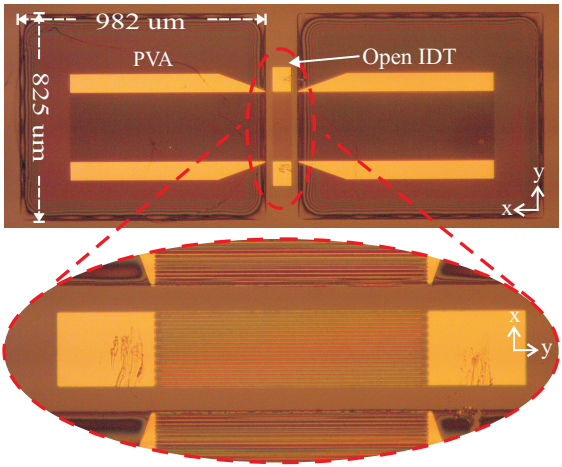

Figure 5.25: RH sensor with PVA film loaded on the reflectors of the SAW resonator.

The sensor is characterized at 10 different RHs from 16 % to 77.2 % with the above mentioned setup, and 6 of the time gated results are shown in Fig. 5.26. The resonance frequency peak becomes undetectable at 77.2 % with this PVA film pattern, and the cutoff RH is 72.8 %. However this is 13.7 % more than the sensor with the first PVA film pattern.

5.4.3 Comparison of the Sensors Performances

The RH sensors covered with two different PVA film patterns with almost the same thickness show different performances. The average sensitivity, the maximum reflection and the broadness of the peaks, from which the

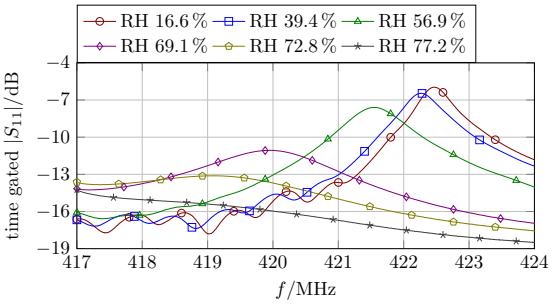

Figure 5.26: Measurement results of RH humidity sensor with PVA film loaded on the reflectors of the SAW resonator only, after time gating.

quality factor is evaluated, are compared. The results are discussed as follows.

The average sensitivity η of the RH sensor is defined as::

$$\eta = \left| \frac{\Delta f}{\Delta \mathrm{RH}} \right| = \left| \frac{f_1 - f_2}{\mathrm{RH}_1 - \mathrm{RH}_2} \right|, \tag{5.30}$$

where Δf is the difference between the resonance frequencies f_1 and f_2 at two RH measurements, and ΔRH is the difference between the corresponding relative humidity values RH_1 and RH_2.The results of the average sensitivity are calculated and plotted at the middle of two RH values in Fig. 5.27.

It can be seen that for both cases the average sensitivity increases with RH. The sensor with open PVA film on IDT pads has a smaller RH operation range, but within the operation range it has an overall average sensitivity of 89.34 kHz/%RH, which is 3.87 times higher than the sensor with PVA film patterned on the reflectors in the same range. It is because the PVA film covers a larger area of the SAW resonator, which introduces more mechanical loading changes with the variation of RH.

The maximum reflection is the maximum magnitude of S_{11} after time gating. The results are shown in Fig. 5.28. The maximum reflection magnitude of the sensor with PVA film loaded on the reflectors is higher than the sensor with open windows of PVA film on the IDT pads, e.g., at approximate 15 % RH the maximum magnitude of PVA film laded on

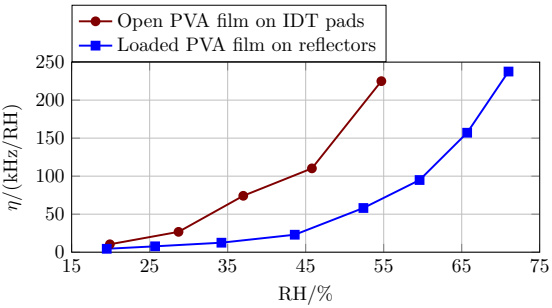

Figure 5.27: Comparison of the average sensitivity of the RH sensor with two PVA film patterns open on IDT pads and loaded on SAW reflectors.

the reflector is 0.53 dB higher and at approximate 59 % RH it is 5.44 dB higher than the sensor with open windows of PVA film on IDT pads.

The quality factor Q is defined as the resonance frequency f_{res} of the SAW resonator divided by the −3 dB bandwidth of the time gated results $\mathrm{BW}_{3\mathrm{dB}}$. The outcome is shown in Fig. 5.29.

Because high quality factor is preferable in sensing application, the sensor with loaded PVA film on the reflectors is preferable in practice, since its average Q is nearly 141 higher compared to the sensor with open PVA

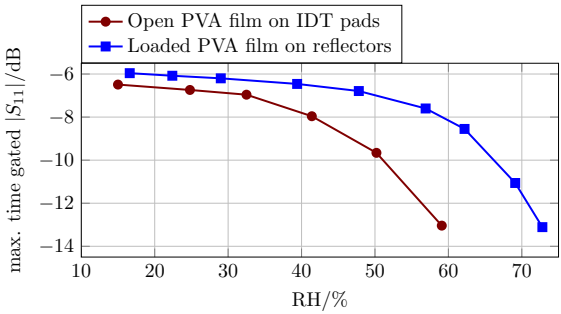

Figure 5.28: Comparison of the maximum magnitude of the RH sensor with PVA film patterns open on IDT pads and loaded on SAW reflectors.

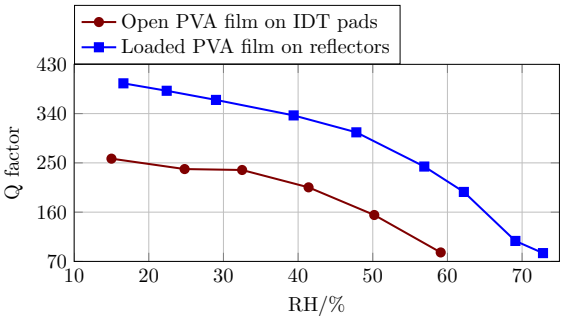

Figure 5.29: Comparison of the quality factor of the RH sensor with PVA film patterns open on IDT pads and loaded on SAW reflectors.

film on IDT in the RH range from 15 % to 59 %. There are several reasons for the improvements of the maximum reflection and Q factor of the sensor with PVA film loaded on the reflectors. First, the impedance matching of the sensor with PVA film loaded on the reflectors is better, which means the coupling between EMW and SAW is improved. Second, since there is no PVA film on the IDT, the dielectric losses of the EMW are lower during the coupling. Last, since there is also no PVA film on the substrate between the IDT and reflectors of the SAW resonator, the attenuation of the SAW is lower.

5.5 Relative Humidity Sensors with Different PVA Film Thickness

In section 5.4, it is proven that different PVA film patterns can facilitate the humidity sensors design with various performances such as different operation range, sensitivity and quality factor. Besides the patterns, another way to alter the performances of the humidity sensors is to employ different thickness of the PVA film. Since the SAW resonator based humidity sensors detect the humidity by the change of mechanical loading, different thickness of PVA film can absorb various mass of water molecules and obtain different size of swelling under the same environmental humidity. Therefore, with the help of the PVA film patterning method introduced in 5.4, humidity sensors with two different thickness of PVA film loaded on the reflectors of the same one port SAW

resonator are characterized at different relative humidity levels. The operation range, sensitivity and quality factor of the two humidity sensors are compared. The sensor with thicker PVA film has higher sensitivity, while the sensor with thinner PVA film shows properties of larger operation range and higher quality factor.

5.5.1 Sensor Structure and Measurement Results

A one port SAW resonator is employed for the study of the influence of different thickness of PVA film for humidity sensing application. The SAW resonator has the same structure shown in Fig. 5.14, and it is made of gold with a thickness of 108 nm. The IDT contains 21 fingers with an aperture of 267 µm. The reflector has 200 shorted electrodes, and each electrode is 1.96 µm wide and 275 µm long. The gap between the IDT and the reflector is 590.17 µm.

The wet method of patterning the PVA film introduced in section 5.4 is applied. The PVA film is only loaded on the reflectors of the SAW resonator. The sensor structure is shown in Fig. 5.30. By varying the speed of the spin coating of the PVA solution, different thickness of the PVA film can be obtained. Two different thickness of the PVA film of 315 µm and 531 µm are realized for the humidity sensing application.

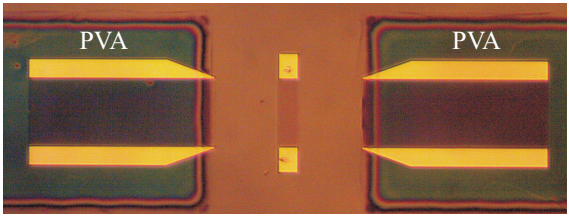

Figure 5.30: One port SAW resonator with different thickness of PVA film loaded on the reflectors for humidity sensing application.

The humidity characterization of the sensors is performed in the same climate chamber shown in Fig. 4.3. The S_{11} of the sensors are measured with a VNA through a signal ground wafer probe. A time gate from 101 ns to 1 ms is implemented to the measurements to eliminate the interrogation signal and the electromagnetic wave reflection from the IDT.

The SAW resonator is first coated with 315 µm PVA film, and then characterized at 8 RHs from 12 % to 89 %. The results of S_{11} after time gating at 5 RHs are shown in Fig. 5.31.

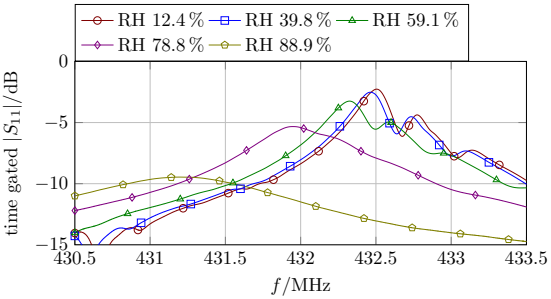

Figure 5.31: Measurement results of the RH humidity sensor with a 315 nm thick PVA film.

The resonant frequency of the sensor decrease with increasing RH in the range from 430.5 MHz to 433.5 MHz. The curves get broader with increasing RH, which indicates decreasing quality factors. The cutoff RH of this sensor is 88.9 %. After the measurements, the PVA film on the SAW resonator is washed away by AZ726 MIF developer and further cleaned by de-ionized water. Then, the PVA solution is spin-coated on the reflector of the SAW resonator with slower speed again. The thickness of the PVA film is measured about 531 nm. The S_{11} of the sensor is measured at 7 different RHs, and the time gate from 101 ns to 1 ms is implemented to the measurements. Five time gated S_{11} curves from 17.8 % to 72.3 % are shown in Fig. 5.32.

The resonant frequencies of this sensor shift to lower frequency range from 429 MHz to 432 MHz compared to the results of the sensor with 315 nm thick PVA film. The cutoff RH is 72.3 %.

5.5.2 Comparison of the sensor performances

The two RH sensors are using the same SAW resonator, the only difference between them is the thickness of the PVA film. The sensor performance, the operating range, the average sensitivity and the quality factor of both sensors are compared, and the results are discussed in the following.

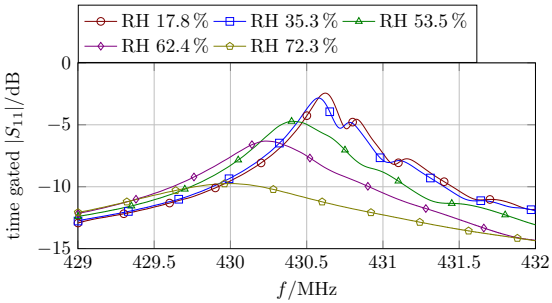

Figure 5.32: Measurement results of RH humidity sensor with 531 nm thick PVA film.

First, the resonance frequencies of both sensors at different RHs are compared in Fig. 5.33. The average resonant frequency of the sensor with 315 nm thick PVA film is 1.77 MHz smaller than the average resonant frequency of the sensor with 531 nm thick PVA film. Since the sensors are based on the same SAW resonator, thicker loaded film shifts the operating frequency to lower values. The sensor with 315 nm thick PVA film has larger operating range, since the cutoff RH is 16.6 % larger than the cutoff RH of the sensor with 531 nm thick PVA film.

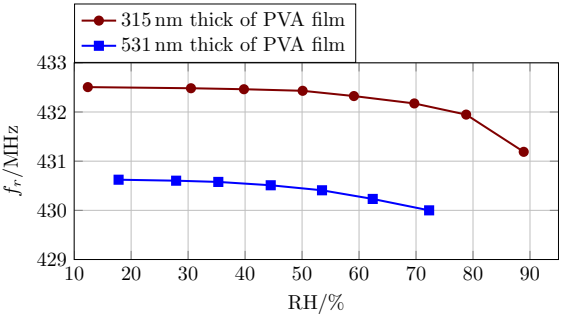

Figure 5.33: Resonant frequencies of the RH sensor with PVA film thickness of 315 nm and 531 nm.

The average sensitivity, which is defined in Eq. 5.30, is calculated for both thickness, and the results are plotted at the middle of two RHs in

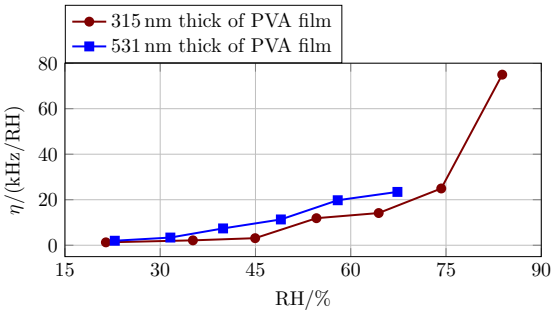

Figure 5.34: Average sensitivity of the RH sensor with PVA film thickness of 315 nm and 531 nm.

Fig. 5.34. Although the sensor with the 531 nm PVA film has a smaller operating range, it has an overall average sensitivity of 11.22 kHz/%RH, which is 1.72 times higher than the sensor with 315 nm PVA film within its operating range. It means, that thicker PVA film can result in higher sensitivity for humidity sensing.

The quality factor is also compared between the humidity sensor with two PVA film thickness, which is calculated by the resonance frequency divided by −3 dB bandwidth of the time gated results of S_{11}. The results are shown in Fig. 5.35. The average quality factor of the sensor with 315 nm thick PVA film on the reflectors is 1.51 times higher than the

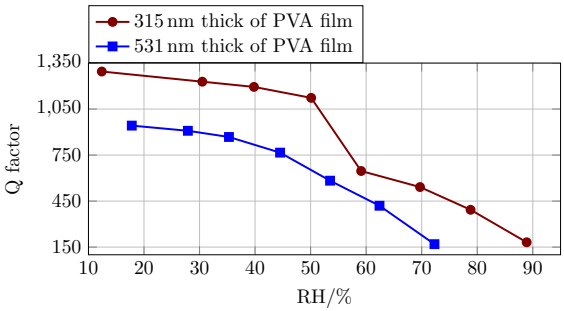

Figure 5.35: Quality factor of both RH sensors with PVA film thickness of 315 nm and 531 nm.

sensor with 531 nm thick PVA film within its operating range from 17.8 % to 72.3 % RH. This result shows, that thick PVA film causes larger losses, which decreases the quality factor more than the sensor with thinner PVA film.

To conclude, depending on the application requirements, the humidity sensor can be specifically designed by the thickness of the PVA film with a certain trade-off of the performance parameters.

Chapter 6

Dual-load Relative Humidity Sensor

The application of the electrical property of the PVA film for humidity sensing has been discussed in Chapter 4. The permittivity of the PVA film changes with different humidity values in an experimental environment. Then, the application of the mechanical loading property of the PVA film for humidity sensing has been discussed in Chapter 5, where the mechanical loading of the PVA is dependent on the environmental humidity level, which results in a changing of velocity of the surface acoustic wave. Both mechanisms for humidity detection are used nowadays, individually.

In this chapter, an attempt is made by realizing a dual-load humidity sensor, using both, electrical and mechanical loading properties of a PVA film in a single structure. By using the dual-load sensor, performance, i.e., the operating range, sensitivity and the quality factor can be improved compared to the humidity sensors using either the electrical or the mechanical loading mechanisms of the PVA film. To realize such a sensor, the one port SAW resonator with anti-corrosive, gold electrodes is combined with an LC resonator. Two IDCs with the same pitch as the IDT are used as reflectors in the SAW resonator. Hygroscopic PVA films are patterned on the IDC reflectors as functional layers to sense the RH. The SAW resonator operates between 433 MHz to 434 MHz. The LC resonator, consisting of the IDC reflectors as variable capacitance and a lossy inductor as inductance, is designed in a frequency band below 350 MHz in the simulation. An exposure of the PVA film to different RH environments causes both, a mechanical loading and a permittivity change. The change of resonance frequency of the SAW resonator is dominated mainly by the change of the mechanical loading of PVA film at different RHs. The resonance frequency of the LC resonator varies with the change of the PVA film permittivity. Due to the two different RH sensing mechanisms, the sensor has an enlarged RH operation range and better sensor performances.

The sensitivity and the quality factor are two important parameters for evaluation of the performances of such a sensor. However, there is a certain trade-off in RH sensing, using PVA film. If better sensitivity is achieved, Q factor is lower, since thicker film is needed according to the last subchapter 5.4.2. A figure of merit (FoM), containing these two parameters, is defined and used to evaluate the sensor performances additionally. Then, the extracted FoM for both sensing mechanisms are compared over the whole RH range, and the better one is chosen to detect the RH with a certain range of RH.

6.1 One Port SAW Resonator

The SAW resonator is fabricated on YZ cut $LiNbO_3$ substrate with 20 nm chromium and 80 nm gold layer evaporated on top, which is shown in Fig. 6.1. The IDT has 10-pair electrodes with a pitch of 3.9 µm. The reflectors are made of two 100 finger pairs of IDCs with the same pitch as the IDT, and the length of the overlapped fingers is 275 µm.

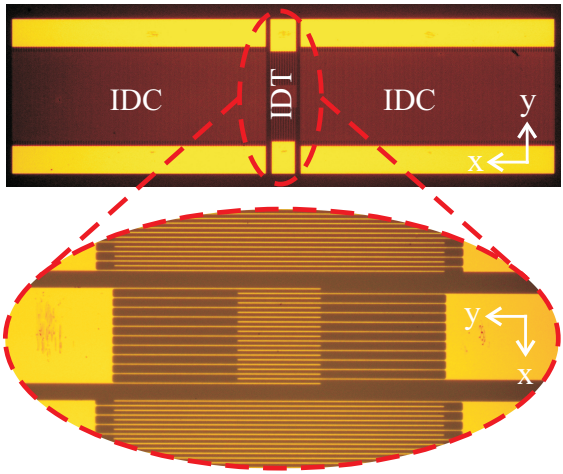

Figure 6.1: SAW resonators with IDCs used as reflectors.

The structure is measured on-wafer with a SG probe, and the scattering parameter S_{11} is measured by using a vector network analyzer. A time gate from 300 ns to 1 ms is implemented to the measurements to eliminate

the interrogation signal and the electromagnetic wave reflection from the IDT. The frequency response of the SAW resonator is shown in Fig. 6.2. The SAW resonator with the IDCs as reflectors has the same frequency response as the resonator with short gratings as reflectors. The SAW resonator resonates at 436.6 MHz with a quality factor of 1431.

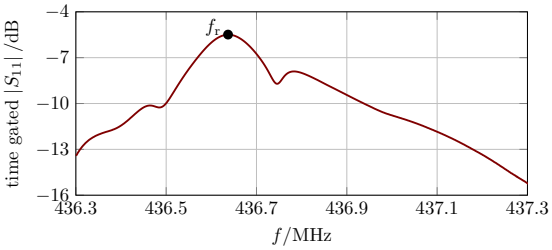

Figure 6.2: Time gated SAW resonant frequency peaks.

6.2 Dual-load Sensor Structure

A 10 % PVA solution is prepared and spin-coated on the structure. With the treatment and the photolithographic method of patterned PVA film introduced in Chapter 5.4, a thickness of 360 nm PVA film is patterned on the IDC reflectors only as shown in 6.3.

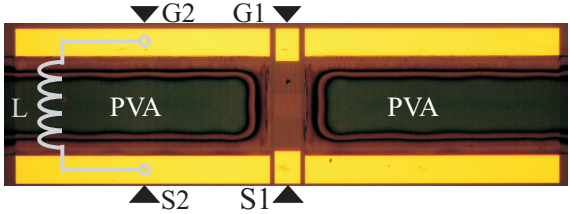

Figure 6.3: Dual-load RH sensor structure with IDC reflectors coated with PVA film only.

6.2.1 SAW Resonator for Humidity Sensing

After the PVA film is loaded on the IDC reflectors, a dual-load relative humidity sensor is realized. The mechanical loading sensing mechanism is first characterized by measuring the humidity frequency response of the SAW resonator through terminal S1G1 as shown in Fig. 6.3. The results are also filtered by the time gate from 300 ns to 1 ms. The SAW resonator for RH sensing is characterized at 7 different RHs from 14 % to 78 % RH at 20°C, where 5 of them are shown in Fig. 6.4.

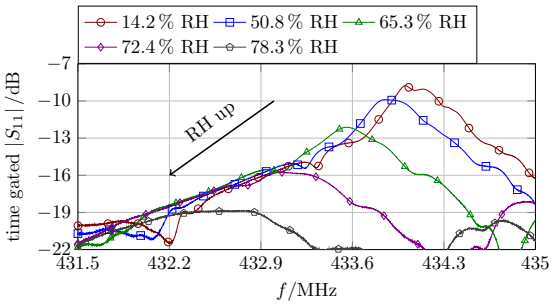

Figure 6.4: Time gated SAW resonant frequency peaks with PVA film loaded on the IDC reflectors.

While the resonance is shifted from 436.6 MHz to a frequency range between 433 MHz and 434 MHz, the quality factor drops from 1431 to a value below 650. When the RH increases, both, the resonance frequency and the quality factor decrease. The maximum RH, which the sensor can detect, is defined as the cutoff RH, which is 72.4 % for the SAW resonator, since there are no detectable peaks within the interested frequency band at higher RHs.

6.2.2 LC Resonator for Humidity Sensing

There is no excitation of the acoustic wave for frequencies below 350 MHz in this sensor configuration. Thus, the IDC reflectors can be used as capacitors. One of the IDC reflectors with loaded PVA film on top is characterized through terminal S2G2 shown in Fig. 6.3 at 6 different RH values from 16.8 % to 89.3 %. The IDC reflector is modeled as a capacitor and an equivalent series resistor. The capacitance and the quality factor

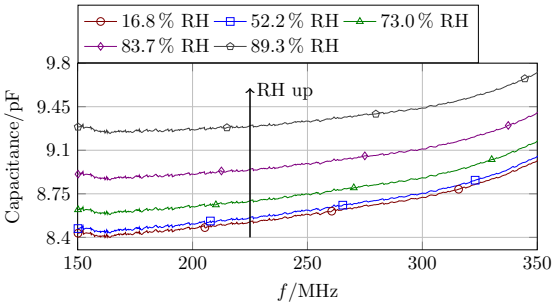

(a) Calculated results of capacitance.

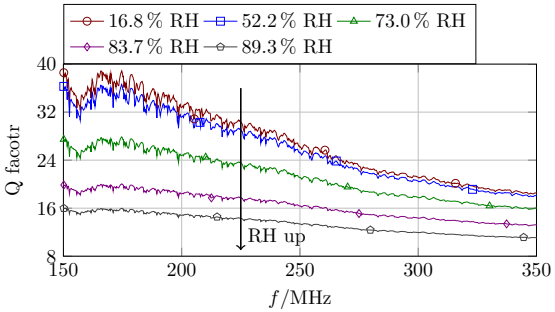

(b) Calculated results of quality factor.

Figure 6.5: Calculated results of capacitance and quality factor of PVA film loaded IDC reflector from the measured scattering parameter at different RHs.

are calculated with the model from the measured scattering parameter as shown in Fig. 6.5.

It can be observed, that the capacitance of the IDC reflector increases with the RH, since the permittivity of the PVA film increases with RH as is already discussed in Chapter 4. The quality factor of the IDC reflector decreases with increased RH due to the increased dielectric loss of the PVA film.

6.3 Sensing Performance Comparison of SAW Resonator and LC Resonator

In order to form an LC resonator, an inductor is connected parallel to the IDC reflector as shown in Fig. 6.3. The parallel LC resonator is simulated by using Agilent ADS schematic simulator applying the measured results of IDC reflector at different RHs and a lossy inductor of 30 nH, which has a measured quality factor of 46 at 900 MHz and a self resonance frequency of 2.35 GHz. The resonance frequency of the parallel LC resonator along with the SAW resonator are shown in Fig. 6.6.

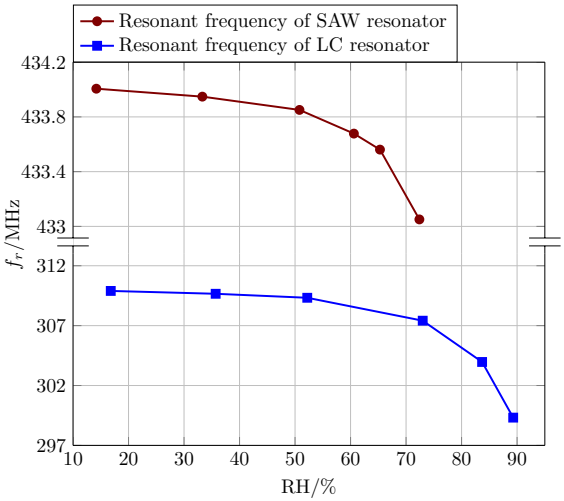

Figure 6.6: Resonant frequency of the SAW resonator and the LC resonator at different RH.

The resonance frequency of both, SAW and LC resonators decrease with increasing RH levels. The RH operation range of the SAW resonator is below 72.4 %, while the RH operation range of LC resonator is up to 89.3 % RH. An improvement of 16.9 % in the RH operation range is realized by using the dual-load humidity sensor compared to the conventional one port SAW resonator based humidity sensors.

A sensitivity of the sensor η is defined as the normalized resonance frequency shift of f_1 and f_2 over the corresponding relative humidity change

of RH_1 and RH_2, as expressed in Eq. 6.1:

$$\eta = \left| \frac{\Delta f}{f_0 \cdot \Delta \mathrm{RH}} \right| = \left| \frac{f_1 - f_2}{(f_1 + f_2)/2} \cdot \frac{1}{\mathrm{RH}_1 - \mathrm{RH}_2} \right|. \tag{6.1}$$

The sensitivities are calculated between two RH measurements, and the values are placed between the resonance frequency points with the unit of 10^{-4}/%RH in Fig. 6.7. Below the cutoff RH, the SAW resonator has an overall average sensitivity of 0.38×10^{-4} /%RH, while the overall average sensitivity of LC resonator is 12.6 times higher with the value of 4.79×10^{-4} /%RH.

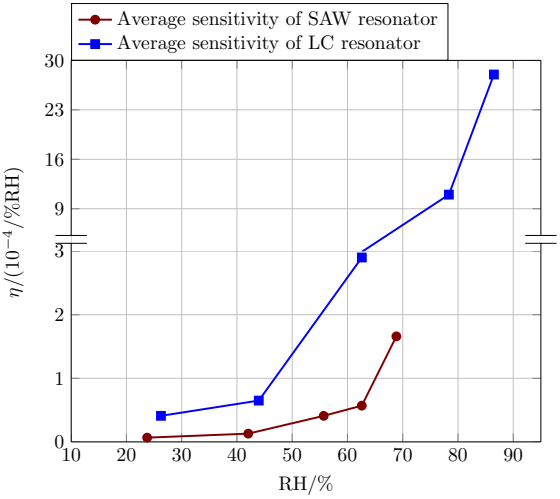

Figure 6.7: Calculated average sensitivity of the SAW resonator and the LC resonator at different RHs.

The quality factor of the SAW resonator and the LC resonator are calculated and compared in Fig. 6.8. When the RH increases, the quality factor of both resonators decreases. The quality factor of the SAW resonator is much higher than the quality factor of LC resonator, the minimum quality factor of SAW resonator is 267 which is 30.7 times higher than the minimum quality factor of the LC resonator.

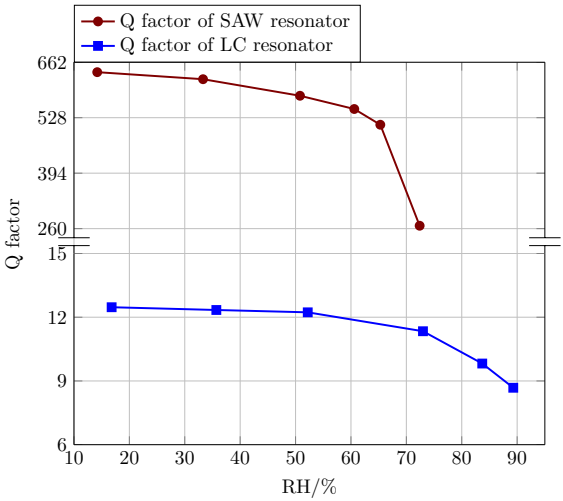

Figure 6.8: Quality factor of the SAW resonator and the LC resonator at different RH.

6.4 Figure of Merit

Considering the average sensitivity in Fig. 6.7 and quality factor in Fig. 6.8 of both, SAW resonator and LC resonator for RH sensing, a tradeoff between sensitivity and quality factor can be found. It is evident that, when the sensitivity increases, the quality factor decreases. To evaluate a tradeoff, a figure of merit is defined as key sensor performance, which considers both, sensitivity η and quality factor in the following way:

$$\mathrm{FoM} = \mathrm{Q} \cdot \eta, \tag{6.2}$$

The FoM of the dual-load RH sensor is calculated and plotted at the RH values from 30 % to 90 % shown in Fig. 6.9. The FoM of the SAW resonator for RH sensing first increases with RH and then it starts to decrease above 72.4 %. Above this cutoff RH, the SAW resonator is considered out of operation for RH sensing, since the FoM drops to zero at 78.3 %. In contrast, the FoM of the LC resonator increases significantly. By comparing the FoM of both resonators, an optimum RH operation range for each resonator can be defined. For sensing the RH below 72.4 %, the SAW resonator is better suited due to the significant

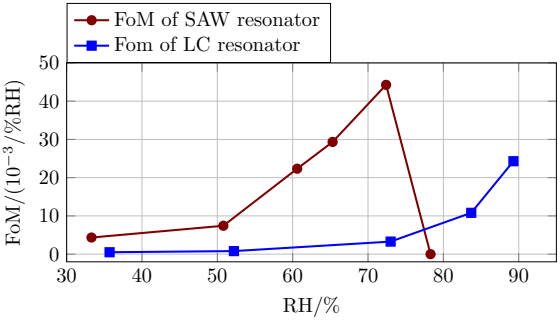

Figure 6.9: Figure of merit of the SAW resonator and the LC resonator for RH sensing.

higher FoM, while above this cutoff RH, the LC resonator is preferred instead because of better FoM. Thus, expanding a larger operating range for RH sensing, compared to the sensors with single loading mechanism. Of course different thickness of PVA film or different density of the PVA solution is used to form the functional layer, the cutoff RH of the SAW resonator and the FoM for both sensing structures will be different. In any design, the one with better FoM is used for RH sensing in a defined RH range.

Chapter 7

Conclusion and Outlook

This work focuses on the methods of moisture and humidity detection and the applications for efficient sensor designs. A method of material characterization of the moisture content was introduced, and the moisture content of different kinds of tobacco were measured for a specific application by using the proposed methods. The information of the tobacco moisture content was later used for a mass flow sensor design. Consequently, the methods of humidity measurements, i.e., the water vapor content in air, were discussed. A material named polyvinyl alcohol (PVA) was chosen as a sensitive layer for relative humidity (RH) sensing. The PVA film exhibits two properties when confronts with water vapor: the permittivity of the PVA film changes, and the mechanical loading of the film varies. To characterize the permittivity change, a comprehensive model of the PVA film at different RHs was found. Applying this model to computer simulation tools, the performances of RH sensors, with PVA films can be predicted. To utilize the mechanical loading property of the PVA film, a one port surface acoustic wave humidity sensor was designed. By varying the patterns and thickness of the PVA film, different sensor performances can be observed. In the end, a novel structure of a dual-load one port SAW resonator was proposed for humidity sensing application, which can use both the permittivity change and mechanical loading for humidity sensing, simultaneously. The sensor has shown unique features with improved overall sensor performances.

To characterize the electrical behavior of a material such as complex permittivity, the cavity perturbation method is precise at a single frequency, which was employed accordingly. A rectangular resonator was used for sample characterization, using small loops for electromagnetic wave coupling. The complex permittivity of the material under test can be calculated through the resonant frequency and quality factor before and after the sample is inserted into the resonator as a small perturbation. 6 different brands of cigarettes and a Tobacco Substitution were

characterized using the cavity perturbation method, and the absolute permittivity and loss tangent were calculated. The weight and moisture content of each brand of cigarettes were each measured by a scale and moisture analyzer. The calculated absolute complex permittivity and loss tangent of 6 brands of cigarettes and the Tobacco Substitution were related to the mass of the water content, a linear increased tendency between the mass of moisture content and the absolute complex permittivity and loss tangent were proven. The tobacco moisture content was used as pre-knowledge for a mass flow sensor design, which is based on an open cylindrical resonator. The resonator contains two circular waveguides with different diameters, which were employed as the tobacco conveying pipeline. Since the cutoff frequency of the pipeline is larger than the cutoff frequency of the sensor, the energy is trapped into the sensor, forming an open resonator. Based on the requirement of the dimension limitation, a feasible radius and length of the sensor were calculated, and a 1 m long sensor with a radius of 75 mm was built for testing. 4 measurements were obtained by feeding different weights of tobacco to the mass flow sensor in various time duration, with all of the measurements resulting in a 10 % discrepancy.

After introducing the method of characterizing the moisture content of a solid material, the approaches of detecting the humidity in the air were proposed. Polyvinyl alcohol was chosen as the sensitive layer for humidity sensing due to the advantages of good sensitivity, ease of process, and low price. The PVA film exhibits two characteristics for humidity sensing, i.e., the change of electrical loading and mechanical loading. Both of the sensing mechanisms were discussed in this work.

The change of electrical loading of PVA film suggests the permittivity changes with different humidity levels. A broadband characterization of PVA film, using an interdigital capacitor has been performed for RH sensing application in a climate chamber with a variable humidity level. A conformal mapping method was used to mathematically model the PVA film covered IDC for the extraction of the PVA film complex relative permittivity at different RHs. Substantially, dielectric relaxation of PVA film was observed at a high RH. Low hysteresis and stable long interval performance of PVA films have been proven based on experiments, which make PVA films a promising material for RH sensing. A comprehensive model for the electrical property of PVA films was described by the Cole–Cole equation with coefficients calculated from a fitting algorithm of the characterization data. The function of each coefficient in the Cole–Cole equation over relative humidity was found, in which the permittivity at an arbitrary RH can be obtained. This mathematical

model of electrical property of PVA films can be used to accurately predict the RH sensor performances by computer simulation tools, so that the operating frequency, the bandwidth, and sensitivity of the RH sensors can be designed. In order to verify the mathematical model of the PVA film, a chipless, highly sensitive, low profile, low cost and easily fabricated wireless relative humidity sensor based on a PVA film was designed and characterized. By measuring the reflection of the radar cross section of the sensor at different RHs, a maximal 5.35 MHz/%RH sensitivity above 50 % RH was achieved with the interrogation distance of 12 cm. A simulation model was built in CST Microwave Studio with the PVA film dielectric property calculated by the Cole–Cole equation at a measured RH. A good agreement between the simulation and measurement results has proven the accuracy of the PVA film model, and offered great practicability and aid for the RH sensor design.

To utilize the mechanical loading property of the PVA film, surface acoustic wave resonators were employed. A humidity sensor was formed by loading the PVA film on top of the SAW resonator. When the PVA film absorbs or adsorbs water molecules in the air, the mechanical loading of the film changes, leading to a change of in SAW velocity. From the reflection parameters obtained by the vector network analyzer, the resonant frequency change can be detected with varying humidity. To facilitate the convenient measurement and integration ability of the humidity sensor, a photolithographic method of patterning PVA films with micrometer resolution was found using its solubility characteristic. Likewise, the design freedom of RH sensors was increased in order to fulfill different application requirements. Two RH sensor topologies based on a SAW resonator with different patterns of PVA films were designed, and their performances were compared. The sensor with open PVA film on IDT pads has shown better average sensitivity, while the sensor with PVA film loaded on the reflectors has shown larger operating RH range, higher maximum reflection and higher quality factor. Later the influence of PVA film thickness on the sensor performances was studied. The humidity sensor with thicker PVA film presented higher sensitivity, while the sensor with thinner PVA film indicated the properties of higher operation range and larger quality factor. According to different application requirements, various PVA films can be selected for the sensor design.

To use both, the electrical loading and mechanical loading at the same time, a dual-load RH sensor was designed and realized by an anti-corrosive SAW resonator and LC resonator, where the capacitor was employed as the IDC reflector of the SAW resonator and coated with PVA film. Two different sensing mechanisms were applied in the sensor: the resonance

frequency of SAW resonator was mainly determined by the RH due to the altered mechanical loading of PVA film, while the LC resonator was tuned by the RH dependent PVA film permittivity. The sensor has enlarged the RH operation range by using this dual-load sensing mechanism. A figure of merit was defined to evaluate the sensor performances, which considered the sensitivity and the quality factor at the same time. By comparing the FoM of the two resonators, the better one of the two can be used for RH sensing in a defined RH range.

To further improve the operation range, sensitivity, and quality factor, a multi-structure humidity sensor can be a promising approach that will demand attention in the future. This sensor might consist of several structures such as EMW resonators and SAW resonators loaded with different patterns and various thickness of the PVA films. They can work as frequency division, i.e., each sensor element achieves its optimal performance in a defined frequency range, or time division, in which each sensor element works separately in time by applying a different time window.

Bibliography

[1] A. Penirschke and R. Jakoby. Metamaterial transmission line resonators for structural moisture sensing in buildings. In *Instrumentation and Measurement Technology Conference (I2MTC), 2013 IEEE International*, pages 713–716, May 2013.

[2] D. Lu, A. Penirschke, and R. Jakoby. Dielectric characterization of tobacco at microwaves. *International Conference on Electromagnetic Wave Interaction with Water and Moist Substances*, pages 172–176, 2013.

[3] D. Cirmirakis, A. Demosthenous, N. Saeidi, and N. Donaldson. Humidity-to-frequency sensor in cmos technology with wireless readout. *Sensors Journal, IEEE*, 13(3):900–908, March 2013.

[4] Xingwang Wang and Yue Liu. The study of the agricultural product storage temperature and humidity control system. In *Computer Science and Network Technology (ICCSNT), 2013 3rd International Conference on*, pages 46–49, Oct 2013.

[5] E. Traversa. Ceramic sensors for humidity detection: the state-of-the-art and future development. *Sensors and Actuators B: Chemical*, 68:135–156, 1995.

[6] L. F. Chen, C. K. Ong, C. P. Neo, V. V. Varadan, and V. K. Varadan. *Microwave Electronics: Measurement and Materials Characterization*. John Wiley & Sons, Ltd, Chichester, UK, 2005.

[7] R.A. Waldron. Perturbation theory of resonant cavities. *Proceedings of the IEE - Part C: Monographs*, 107(12):272–274, September 1960.

[8] M.A. Saed. A method of moments solution of a cylindrical cavity placed between two coaxial transmission lines. *IEEE Transactions on Microwave Theory and Techniques*, 39:1712–1717, 1991.

[9] C. Caliendo, E. Verona, A. D'Amico, A. Furlani, G. Iucci, and M.V. Russo. A new surface acoustic wave humidity sensor based on a polyethynylfluorenol membrane. *Sensors and Actuators B: Chemical*, 18:82–84, 1994.

[10] Y-T Chen and HL Kao. Humidity sensors made on polyvinyl-alcohol film coated saw devices. *Electronics Letters*, 42:948–950, 2006.

[11] M. Penza and G. Cassano. Relative humidity sensing by pva-coated dual resonator saw oscillator. *Sensors and Actuators B: Chemical*, 68:300–306, 2000.

[12] A. Buvailo, Y. Xing, J. Hines, and E. Borguet. Thin polymer film based rapid surface acoustic wave humidity sensors. *Sensors and Actuators B: Chemical*, 156:444–449, 2011.

[13] Y. Li, M. Yang, M. Ling, and Y. Zhu. Surface acoustic wave humidity sensors based on poly (p-diethynylbenzene) and sodium polysulfonesulfonate. *Sensors and Actuators B: Chemical*, 122:560–563, 2007.

[14] T. Nomura, K. Oofuchi, T. Yasuda, and S. Furukawa. Saw humidity sensor using dielectric hygroscopic polymer film. *Ultrasonics Symposium, 1994. Proceedings., 1994 IEEE*, 1:503–506, 1994.

[15] N. Tashtoush, J. Cheeke, and N. Eddy. Surface acoustic wave humidity sensor based on a thin polyxio film. *Sensors and Actuators B: Chemical*, 49:218–225, 1998.

[16] Y.-H. Kim, K. Jang, Y. J. Yoon, and Y.-J. Kim. A novel relative humidity sensor based on microwave resonators and a customized polymeric film. *Sensors and Actuators B: Chemical*, 117:315–322, 2006.

[17] E.M. Amin, N.C. Karmakar, and B. Winther-Jensen. Polyvinyl-alcohol (pva)-based rf humidity sensor in microwave frequency. *Progress In Electromagnetics Research B*, 54:149–166, 2013.

[18] E.M. Amin, M.S. Bhuiyan, N.C. Karmakar, and B. Winther-Jensen. Development of a low cost printable chipless rfid humidity sensor. *Sensors Journal, IEEE*, 14(1):140–149, Jan 2014.

[19] D. Lu, Y. Zheng, M. Schuessler, A. Penirschke, and R. Jakoby. Highly sensitive chipless wireless relative humidity sensor based on polyvinyl-alcohol film. *Antennas and Propagation Society International Symposium (APSURSI)*, pages 1612–1613, 2014.

[20] D. Lu, Y. Zheng, A. Penirschke, Y. Wiens, W. Hu, and R. Jakoby. Humidity dependent permittivity characterization of polyvinyl-alcohol film and its application in relative humidity rf sensor. *European Microwave Conference (EuMC)*, pages 163–166, 2014.

[21] P. Story, D. Galipeau, and R. Mileham. A study of low-cost sensors for measuring low relative humidity. *Sensors and Actuators B: Chemical*, 25:681–685, 1995.

[22] Jingyi Yang, Xinyong Dong, Kai Ni, Chi Chiu Chan, and P.P. Shum. Relative humidity sensor based on optical fiber gratings and polyvinyl alcohol. In *Advanced Infocomm Technology (ICAIT), 2014 IEEE 7th International Conference on*, pages 137–142, Nov 2014.

[23] Tao Li, Xinyong Dong, Chi Chiu Chan, Kai Ni, Shuqin Zhang, and P.P. Shum. Humidity sensor with a pva-coated photonic crystal fiber interferometer. *Sensors Journal, IEEE*, 13(6):2214–2216, June 2013.

[24] Jacob Fraden. *Handbook of Modern Sensors: Physics, Designs, and Applications*. Springer-Verlag New York, 2010.

[25] P. Debye. Polar molecules. *Journal of the Society of Chemical Industry*, 48:172, 1929.

[26] M. Sucher and J. Fox. *Handbook of Microwave Measurements Vol. 2, 3rd ed.* Polytechnic Press of the Polytechnic Institute of Brooklyn, 1963.

[27] D.M. Pozar. *Microwave Engineering, 3rd ed.* Wiley, 2005.

[28] H Moeller, J. Tobias, W. Traute, and R. Knoechel. Microwave-resonator and measuring device, Jul. 2005.

[29] A.W. Kraszewski, S. Trabelsi, and S.O. Nelson. Comparison of density-independent expressions for moisture content determination in wheat at microwave frequencies. *Journal of Agricultural Engineering Research*, 71(3):227 – 237, 1998.

[30] Klaus Kupfer. *Electromagnetic Aquametry: Electromagnetic Wave Interaction with Water and Moist Substances*. Springer Science & Business Media, 2005.

[31] S. Trabelsi, A.W. Kraszewski, and S.O. Nelson. A new density-independent funsction for microwave moimoist content determination in particulate materials. In *IEEE Instrumentation and Measurement Technology Conference Proceedings*, Ottawa, Canada, May 19-21, 1997.

[32] R. Scharnow. Codiertes Handbuch der Güter des Seetransports, VE Kombinat Seeverkehr und Hafenwirtschaft - Deutfracht/Seereederei. Ingenieurhochschule für Seefahrt Warnemünde/Wustrow. Bd. 1:

Stückgut A-K, Bd. 2: Stückgut L-Z, Bd. 3: Spezialgut, Rostock 1986.

[33] R. Scharnow. Praxis des Seetransports. Band 1: Warenkunde-Ladungspflege, 1. Auflage, transpress VEB Verlag für Verkehrswesen, Berlin 1981.

[34] Reemtsma GmbH & Co: Informationen zum Thema Tabak, Hamburg, 31.10.1996.

[35] Yong Yan. Mass flow measurement of bulk solids in pneumatic pipelines. *Measurement Science and Technology*, 7:1687–1706, 1996.

[36] Y. Yan and D. Stewart. Guide to the flow measurement of particulate solids in pipelines. Technical report, Institute of Measurement and Control, National Engineering Laboratory and the University of Greenwich, 2001.

[37] 1995 "Granuflow", GMR 130, Mass Flow Indicator,Endress and Hauser,Technical Information, TI 008G/01/e.

[38] A. Penirschke and R. Jakoby. Microwave mass flow detector for particulate solids based on spatial filtering velocimetry. *Microwave Theory and Techniques, IEEE Transactions on*, 56(12):3193–3199, Dec 2008.

[39] A. Penirschke. *Hochauflösende Mikrowellensensoren zur berührungs-losen Detektion der Konzentration und Strömungsgeschwindigkeit von pulverisierten Feststoffen.* PhD thesis, TU Darmstadt, April 2009.

[40] Z. Wang, J. Liu, and L. Liu. Permittivity measurement of $Ba_{0.5}Sr_{0.5}TiO_3$ ferroelectric thin films on multilayered silicon substrates. *IEEE Transactions on Instrumentation and Measurement*, 55:350–356, 2006.

[41] S. Gevorgian, L.J.P. Linner, and E.L. Kollberg. Cad models for shielded multilayered cpw. *IEEE Transactions on Microwave Theory and Techniques*, 43:772–779, 1995.

[42] S. Gevorgian, T. Martinsson, P.L.J. Linner, and E.L. Kollberg. Cad models for multilayered substrate interdigital capacitors. *IEEE Transactions on Microwave Theory and Techniques*, 44:896–904, 1996.

[43] Kenneth S. Cole and Robert H. Cole. Dispersion and absorption in dielectrics i. alternating current characteristics. *The Journal of Chemical Physics*, 9:341–351, 1941.

[44] R. Sengwa and K. Kaur. Dielectric dispersion studies of poly(vinyl alcohol) in aqueous solutions. *Polym. Int.*, 49:1314–1320, 2000.

[45] Y.E. Ryabov, Y. Feldman, N. Shinyashiki, and S. Yagihara. The symmetric broadening of the water relaxation peak in polymer-water mixtures and its relationship to the hydrophilic and hydrophobic properties of polymers. *JOURNAL OF CHEMICAL PHYSICS*, 116:8610–8615, 2002.

[46] S. Sinha, S.K. Chatterjee, J. Ghosh, and A.K. Meikap. Dielectric relaxation and ac conductivity behaviour of polyvinyl alcohol-hgse quantum dot hybrid films. *Journal of Physics D: Applied Physics*, 47:275301, 2014.

[47] O.H. Karabey. *Electronic Beam Steering and Polarization Agile Planar Antennas in Liquid Crystal Technology*. Switzerland: Springer International Publishing, 2014.

[48] Z. Chen and C. Lu. Humidity sensors: A review of materials and mechanisms. *Sensor Letters*, 3:274–295, 2005.

[49] M.V. Fuke, P.V. Adhyapak, U.P. Mulik, D.P. Amalnerkar, and R.C. Aiyer. Electrical and humidity characterization of m-na doped au/pva nanocomposites. *Talanta*, 78:590–595, 2009.

[50] R. Igreja and C. Dias. Analytical evaluation of the interdigital electrodes capacitance for a multi-layered structure. *Sensors and Actuators A: Physical*, 112:291–301, 2004.

[51] SCHOTT. Schott Borosilicate Float Glass Borofloat 33 Data Sheet. http://www.howardglass.com/pdf/borofloat.pdf.

[52] T.J. Harpster, B. Stark, and K. Najafi. A passive wireless integrated humidity sensor. In *Micro Electro Mechanical Systems, 2001. MEMS 2001. The 14th IEEE International Conference on*, pages 553–557, 2001.

[53] Bodong Li, O. Yassine, and J. Kosel. Integrated passive and wireless sensor for magnetic fields, temperature and humidity. In *SENSORS, 2013 IEEE*, pages 1–4, Nov 2013.

[54] M. Penza and V.I. Anisimkin. Surface acoustic wave humidity sensor using polyvinyl-alcohol film. *Sensors and Actuators A: Physical*, 76:162–166, 1999.

[55] J. Tichy, J. Erhart, E. Kittinger, and J. Privratska. *Fundamentals of Piezoelectric Sensorics*. Springer Science & Business Media, 2010.

[56] Antonio Arnau Vives, editor. *Piezoelectric transducers and applications*. Springer, Berlin, 2008.

[57] V. Plessky and J. Koskela. Coupling-of-modes analysis of saw devices. *International Journal of High Speed Electronics and Systems*, 10:867–947, 2000.

[58] G. Tobolka. Mixed matrix representation of saw transducers. *Sonics and Ultrasonics, IEEE Transactions on*, 26(6):426–427, Nov 1979.

[59] G. Kovacs. A generalised p-matrix model for saw filters. In *Ultrasonics, 2003 IEEE Symposium on*, volume 1, pages 707–710 Vol.1, Oct 2003.

[60] V.P. Plessky. Saw impedance elements. *Ultrasonics, Ferroelectrics, and Frequency Control, IEEE Transactions on*, 42(5):870–875, Sept 1995.

[61] D.P. Morgan. Cascading formulas for identical transducer p-matrices. *Ultrasonics, Ferroelectrics, and Frequency Control, IEEE Transactions on*, 43(5):985–987, Sept 1996.

[62] G. Scholl, A. Christ, W. Ruile, P.H. Russer, and R. Weigel. Efficient analysis tool for coupled-saw-resonator filters. *Ultrasonics, Ferroelectrics, and Frequency Control, IEEE Transactions on*, 38(3):243–251, May 1991.

[63] J. Koskela, V.P. Plessky, and M.M. Salomaa. Saw/lsaw com parameter extraction from computer experiments with harmonic admittance of a periodic array of electrodes. *Ultrasonics, Ferroelectrics, and Frequency Control, IEEE Transactions on*, 46(4):806–816, July 1999.

[64] V.P. Plessky and T. Thorvaldsson. Periodic green's functions analysis of saw and leaky saw propagation in a periodic system of electrodes on a piezoelectric crystal. *Ultrasonics, Ferroelectrics, and Frequency Control, IEEE Transactions on*, 42(2):280–293, March 1995.

[65] I.D. Avramov, A. Voigt, and M. Rapp. Rayleigh saw resonators using gold electrode structure for gas sensor applications in chemically reactive environments. *Electronics Letters*, 41(7):450–452, March 2005.

[66] I.D. Avramov, K. Lange, S. Rupp, B. Rapp, and M. Rapp. Polymer coating behavior of rayleigh-saw resonators with gold electrode structure for gas sensor applications. *Ultrasonics, Ferroelectrics, and Frequency Control, IEEE Transactions on*, 54(1):157–166, January 2007.

[67] W. Soluch. Saw synchronous multimode resonator with gold electrodes on quartz. *Ultrasonics, Ferroelectrics, and Frequency Control, IEEE Transactions on*, 55(6):1391–1393, June 2008.

[68] J.D.N. Cheeke, N. Tashtoush, and N. Eddy. Surface acoustic wave humidity sensor based on the changes in the viscoelastic properties of a polymer film. In *Ultrasonics Symposium, 1996. Proceedings., 1996 IEEE*, volume 1, pages 449–452 vol.1, Nov 1996.

[69] Antonio J. Ricco and Stephen J. Martin. Thin metal film characterization and chemical sensors: monitoring electronic conductivity, mass loading and mechanical properties with surface acoustic wave devices. *Thin Solid Films*, 206(1-2):94 – 101, 1991.

[70] H. Wang, C.-D. Feng, S.-L. Sun, C. U. Segre, and J. R. Stetter. Comparison of conductometric humidity-sensing polymers. *Sensors and Actuators B: Chemical*, 40:211 – 216, 1997.

[71] L. Reindl, G. Scholl, T. Ostertag, H. Scherr, U. Wolff, and F. Schmidt. Theory and application of passive saw radio transponders as sensors. *Ultrasonics, Ferroelectrics, and Frequency Control, IEEE Transactions on*, 45(5):1281–1292, Sept 1998.

List of Publications

[1] D. Lu, A. Penirschke, and R. Jakoby. Dielectric Characterization of Tobacco at Microwaves. *International Conference on Electromagnetic Wave Interaction with Water and Moist Substances*, pp.172-176, Weimar, Germany, September, 2013.

[2] D. Lu, Y. Zheng, M. Schussler, A. Penirschke, and R. Jakoby. Highly sensitive chipless wireless relative humidity sensor based on polyvinyl-alcohol film. *Antennas and Propagation Society International Symposium (APSURSI), 2014 IEEE*, pp.1612-1613, 6-11 July 2014.

[3] D. Lu, Y. Zheng, A. Penirschke, A. Wiens, W. Hu, and R. Jakoby. Humidity dependent permittivity characterization of polyvinyl-alcohol film and its application in relative humidity RF sensor. *European Microwave Conference (EuMC)*, Rome, Italy, October 2014, pp. 163-166.

[4] D. Lu, Y. Zheng, A. Penirschke and, R. Jakoby. Highly sensitive dual-mode relative humidity sensor based on integrated SAW and LC resonators. *Electronics Letters*, vol.51, no.16, pp.1219-1220, 2015.

[5] D. Lu, Y. Zheng, A. Penirschke, and R. Jakoby. Humidity Sensors Based on Photolithographically Patterned PVA Films Deposited on SAW Resonators. *Sensors Journal, IEEE*, vol.16, no.1, pp.13-14, Jan.1, 2016.

[6] D. Lu, M. Maasch, A. Penirschke, Y. Zheng, C. Damm and R. Jakoby. Broadband Permittivity Characterization of Polyvinyl-Alcohol Film for Humidity Sensing Application. *IEEE Transactions on Microwave Theory and Techniques*, vol.64, no.10, pp.3255-3263, Oct. 2016.

Supervised Thesis

Y. Wu: "Study of Microwave Relative Humidity Sensor utilizing PVA Film", *Masterarbeit D2228–M*

Curriculum Vitae

Personal Data

Name:	Donghang Lu
Date of birth:	19.11.1985
Birth Place:	Jilin, China

Education and Career

06.2011–12.2015	Research Assistant in Institute for Microwave Engineering and Photonics at Technischen Universität Darmstadt
09.2008–04.2011	Master of Science in Communications Engineering at Rheinisch-Westfälische Technische Hochschule Aachen
09.2004–07.2008	Bachelor of Science in Electronic Information Engineering at Beihang University
09.2001–07.2004	High school at Jilin No.1 Middle School